Oxygen Ionic-Conducting Ceramics for Gas Separation and Reaction Applications

by

Han-Chun Wu

A Dissertation Presented in Partial Fulfillment
of the Requirements for the Degree
Doctor of Philosophy

Approved January 2020 by the
Graduate Supervisory Committee:

Jerry Y.S. Lin, Chair
Shuguang Deng
Yang Jiao
Heather Emady
Christopher Muhich

ARIZONA STATE UNIVERSITY

May 2020

ABSTRACT

Mixed-ionic electronic conducting (MIEC) oxides have drawn much attention from researchers because of their potential in high temperature separation processes. Among many materials available, perovskite type and fluorite type oxides are the most studied for their excellent oxygen ion transport property. These oxides not only can be oxygen adsorbent or O_2-permeable membranes themselves, but also can be incorporated with molten carbonate to form dual-phase membranes for CO_2 separation.

Oxygen sorption/desorption properties of perovskite oxides with and without oxygen vacancy were investigated first by thermogravimetric analysis (TGA) and fixed-bed experiments. The oxide with unique disorder-order phase transition during desorption exhibited an enhanced oxygen desorption rate during the TGA measurement but not in fixed-bed demonstrations. The difference in oxygen desorption rate is due to much higher oxygen partial pressure surrounding the sorbent during the fixed-bed oxygen desorption process, as revealed by X-ray diffraction (XRD) patterns of rapidly quenched samples.

Research on using perovskite oxides as CO_2-permeable dual-phase membranes was subsequently conducted. Two CO_2-resistant MIEC perovskite ceramics, $Pr_{0.6}Sr_{0.4}Co_{0.2}Fe_{0.8}O_{3-\delta}$ (PSCF) and $SrFe_{0.9}Ta_{0.1}O_{3-\delta}$ (SFT) were chosen as support materials for membrane synthesis. PSCF-molten carbonate (MC) and SFT-MC membranes were prepared for CO_2-O_2 counter-permeation. The geometric factors for the carbonate phase and ceramic phase were used to calculate the effective carbonate and oxygen ionic conductivity in the carbonate and ceramic phase. When tested in CO_2-O_2 counter-permeation set-up, CO_2 flux showed negligible change, but O_2 flux decreased by 10-32% compared with single-

i

component permeation. With CO_2 counter-permeation, the total oxygen permeation flux is higher than that without counter-permeation.

A new concept of CO_2-permselective membrane reactor for hydrogen production via steam reforming of methane (SRM) was demonstrated. The results of SRM in the membrane reactor confirm that in-situ CO_2 removal effectively promotes water-gas shift conversion and thus enhances hydrogen yield. A modeling study was also conducted to assess the performance of the membrane reactor in high-pressure feed/vacuum sweep conditions, which were not carried out due to limitations in current membrane testing set-up. When 5 atm feed pressure and 10^{-3} atm sweep pressure were applied, the membrane reactor can produce over 99% hydrogen stream in simulation.

DEDICATION

To Emily

Thank you for never giving up on me

ACKNOWLEDGMENTS

The pursuit of the PhD degree has been quite a journey. And without my parents, I could never make this far. I want to thank my parents for their unconditional love and support for me. I thank them for always being on my side and giving me hope. I can never hold on to it if they are not around.

To my younger sister Ginny: you are a blessing of my life. You taught me caring and forgiveness. Along with Father and Mother, you are always supportive ever since I can remember. I am in great joy to see now you and your family are well and thriving. You are always on my mind.

To my wife Emily: it is hard to image how fortunate I am to have you in my life. When I am in despair, you are the one who consulted me and never give up. On you I have so much to learn and from you I have received so much. Thank you for always be my guidance and shelter.

I would like to pay my tribute to my advisor, Dr. Jerry Lin. From him not only I see the greatness of knowledge, but also the exceptional work ethic. Always diligent, meticulous and sharp, Dr. Lin is the epitome of scholars. I only wish I could learn more from him.

I would also like to thank all the coworkers I have been working with. Along the way I have received so much help and assistants from my coworkers. I have also learned a lot as a researcher and as a person from our daily interactions. Without you, my PhD career will lose much colors. I wish all of you a wonderful future.

TABLE OF CONTENTS

LIST OF TABLES

LIST OF FIGURES

xi

CHAPTER 1

INTRODUCTION&BACKGROUND

1.1.   General Background

1.1.1. Introduction of Mixed-Ionic Electronic Conducting (MIEC) Materials

Most known mixed-ionic electronic conducting (MIEC) materials are the metal oxides with a lattice structure in perovskite or fluorite structure. For the perovskite materials, the general formula is $ABO_{3-\delta}$. A and B stands for metal ions in the lattice structure. Typically, A-site cations consist of an alkaline earth metal and have a larger ionic radius than B-site cations, which is normally a transition metal. One of the most common natural perovskite compounds is $CaTiO_{3-\delta}$. As **Figure 1.1** shows, the cubic structure of perovskite has a large cation (A-site) on the center, and smaller cations (B-site) on the corners. The B-site cations are coordinated with six oxygen ions (suppose all the oxygen sites are occupied) and form octahedrons. The notation of δ, as indicated in the formula, represents the oxygen nonstoichiometry of the material. In other words, it is an indication of the amount of oxygen defect. One of the most intriguing properties of perovskite materials is that this lattice structure could endure a relative high amount of oxygen defect. The value of δ typically falls between 0 to 0.5 in room conditions. A measure of the mismatch of the average (A–O) and (B–O) equilibrium bond lengths in the cubic phase is given by the deviation from unity (the ideal case) of the geometric tolerance factor (t) (Goldschmidt, 1930):

$$t = \frac{(A\text{-}O)}{\sqrt{2}(B\text{-}O)} \qquad (1)$$

1

The perovskite structure could simultaneously accommodate more than one cations in both A and B lattice sites with the constraints that multiple valences of ions be provided in varying combinations if their sizes are in the range of 0.45–0.75 or 1–1.4 a.u. (atomic units), excluding the formation of compounds with hexavalent and heptavalent ions. However, the formation of a single-phase compound with five or more cations in equivalent amounts is rare, while those with three and four ions are quite common (Roy, 1954; Sunarso *et al.*, 2008).
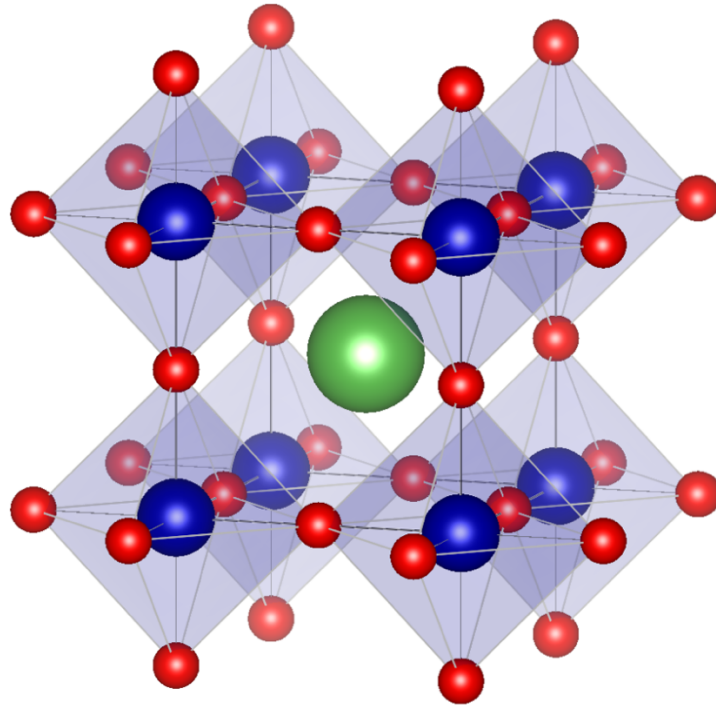
Figure 1.1 *Ideal lattice structure of a typical perovskite material. With a large cation occupying the A-site (green) and smaller cations occupying the B-sites (blue). Oxygen ions (red) forms octahedrons around the B-site cations.*

The ideal fluorite structure consists of anions in simple cubic packing with half of the interstices occupied by cations. This structure has a face-centered cubic (FCC) packing. As shown in **Figure 1.2**, the metal ions are presented as yellow spheres, and non-metal ions are presented in green spheres. The non-metal ions are coordinated with four metal

ions and form tetrahedrons. While most perovskite materials are metal oxides, fluorite structures are commonly seen in halide or other types of minerals. For example, the name of fluorite was initially given to the mineral of CaF_2. However, the discussion about the fluorite in this dissertation will only be on the metal oxides with fluorite lattice structure, which generally have very different properties with the original fluorite. Some fluorite oxides, such as $(ZrO_2)_x(CaO)_{1-x}$, exhibit high electrical conductivity, mainly due to oxygen ion mobility (Kingery *et al.*, 1959). While others, such as $Ce_{2-x}Gd_xO_{1.8}$, have high oxygen ion conductivity but very low electrical conductivity (Zienius *et al.*, 2017). This type of structure tends to have cations occupying all cation sites while leaving many of the oxygen anion sites empty, leading to high oxygen deficiency (Kiukkola and Wagner, 1957).
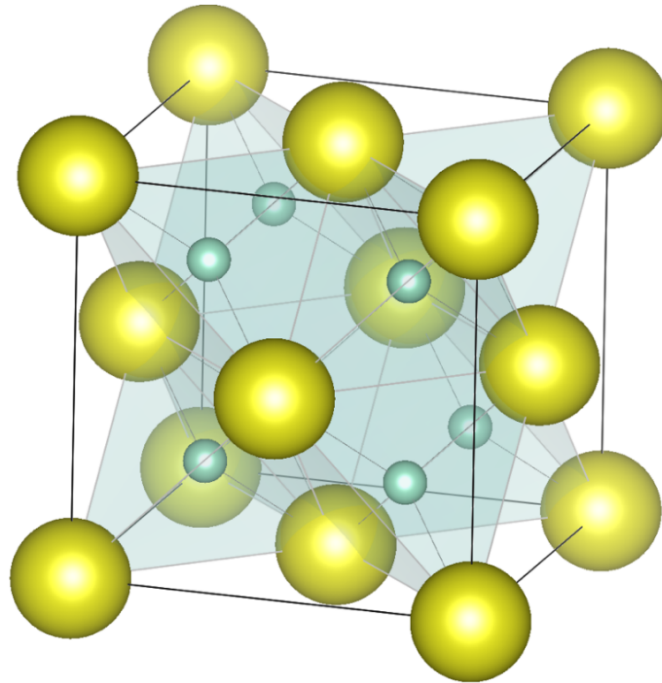
Figure 1.2*. Ideal lattice structure of a typical fluorite material. Metal ions are presented as yellow spheres and non-metal ions are presented in green spheres. The metal ions surround the non-metal ions and form tetrahedrons.*

The inception of the research about ionic transport in solids can be traced back to 1899 when W. Nernst (Nernst, 1899) reported the ionic conduction in solid zirconia. However, this discovery attracts little research attention for either fundamental science or applications until 1976. In that year, Takahashi et al. (Takahashi, Esaka, and Iwahara, 1976) started the initial development materials having both ionic and electronic conductivities, such as Bi_2O_3-BaO. Later on, Cales and Baumard (Cales and Baumard, 1982) introduced the mixed ionic-electronic conduction concept and demonstrated an oxygen semi-permeable membrane. Application of these concepts begins with oxide-ion conduction by vacancies in the materials, both oxide-ion electrolytes and mixed oxide-ion/electronic conductors that may be used as oxygen-permeation membranes, as partial-oxidation catalysts or as components of a solid-oxide fuel cell (Goodenough, 2004).

1.1.2. Overview of Oxygen Production and Its Significance

Oxygen is essential for many industrial processes, such as coal-fired or gas-fired power generation, fuel cell power generation, and many oxidation catalytic processes. The natural source of oxygen is air. However, air only consists of 21% of oxygen, while the rest being 78% of nitrogen, about 1% of argon and carbon dioxide. Nitrogen generally is not involved in the oxidation chemical process. In fact, the abundance of nitrogen poses a negative effect on many occasions. For instance, in a combustion process, nitrogen will be inevitably heated and exhausted to the atmosphere. The energy absorbed by nitrogen will then be wasted.

In light of global warming and climate change, reducing CO_2 emission has become one of the first and foremost tasks in the research society. According to U.S. Environmental Protection Agency (EPA), electricity generation is the second largest sector of CO_2 emission in the U.S. (**Figure 1.3**), and the majority of the CO_2 emission in this sector is from fossil fuel power station (United States Environmental Protection Agency, 2019).

Total U.S. Greenhouse Gas Emissions by Economic Sector in 2017

Agriculture 9%
Commercial & Residential 12%
Transportation 29%
Industry 22%
Electricity 28%
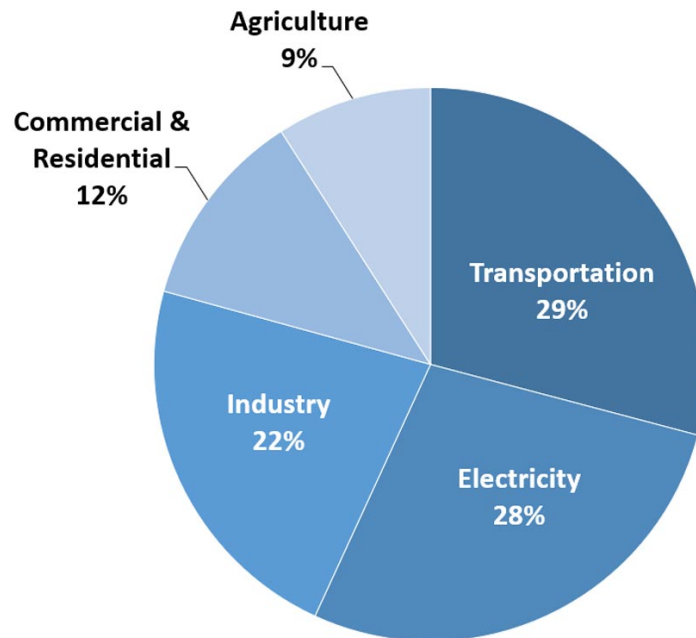
U.S. Environmental Protection Agency (2019). Inventory of U.S. Greenhouse Gas Emissions and Sinks: 1990-2017

Figure 1.3. *Total U.S. greenhouse gas emissions by economic sector in 2017 (United States Environmental Protection Agency, 2019).*

To reduce CO_2 emission from power generation, new combustion technologies coupled with carbon capture and storage (CCS), such as post-combustion capture, pre-combustion capture, and oxy-fuel combustion, have drawn much research interests from

researchers. **Figure 1.4** presents a simplified configuration of these CCS processes. In a post-combustion capture process, CO_2 is separated from the flue gas produced by a fossil fuel power plant. The most effective technique currently is amine absorption (Descamps, Bouallou and Kanniche, 2008; Gibbins and Chalmers, 2008; Kanniche *et al.*, 2010). However, the demonstrated scale of operation is much smaller than the typical requirement for a commercial power plant, and this operation also poses a net 10-14% efficiency drop for the power generation process (Singh *et al.*, 2003; Hammond and Spargo, 2014). On the other hand, a pre-combustion capture process is normally suggested to be connected to an integrated gasification combined cycle (IGCC) power plant. In this process, coal is gasified by pure oxygen and forms a syngas containing CO, CO_2, and H_2. The CO can be transformed into CO_2 via a water-gas shift (WGS) reaction and can then be separated from the H_2-containing stream. An alternative operation is to separate H_2 from the syngas stream, and CO can be combusted in an O_2/CO_2 atmosphere (Williams, Shaddix and Schefer, 2008). While in oxy-fuel combustion, flue gas is recirculated and mixed with oxygen. Due to the elimination of nitrogen, the flue gas will consist mainly CO_2, and the combustion is carried out under an O_2/CO_2 atmosphere, making CCS much practical and economical compared with conventional combustion processes. Several techno-economic assessment studies have suggested that pre-combustion and oxy-fuel technologies have great potential in increasing process efficiency while being much more environment-friendly (Damen *et al.*, 2006; Beér, 2007; Descamps, Bouallou and Kanniche, 2008; Pehnt and Henkel, 2009). For both technologies, an air separation unit is essential to achieve effective CCS. However, current air separation technologies are either adding too much capital cost and making the process not economically viable or still underdeveloped. Therefore, there is a demand for

developing new air separation technology. An overview of these air separation technologies is presented in Chapter 1.2.1.
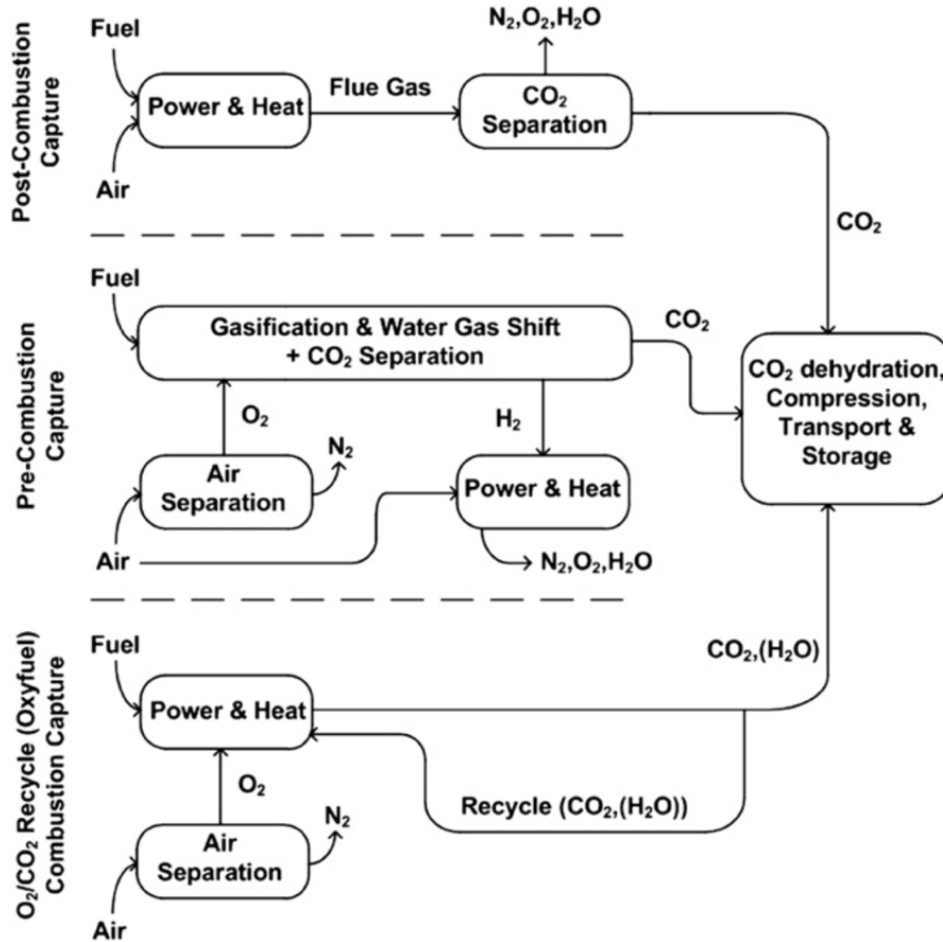
Figure 1.4. *Overall plant configurations for the three main categories of carbon capture technologies (Toftegaard et al., 2010).*

1.1.3. Overview of Hydrogen Production and Its Significance

For carbon reduction, the role of hydrogen is even more critical than oxygen. Hydrogen has been seen as one of the major energy sources for the next generation. Direct utilization of hydrogen does not produce any pollutant, and hydrogen has the highest energy/weight ratio among all types of fuels (Service, 2004). It is very obvious that the

most readily available hydrogen source on earth is water. Hydrogen and oxygen can both be generated form the water-splitting reaction:

$$H_2O \leftrightarrow 1/2O_2 + H_2 \qquad \Delta H^0_{298K} = 285 \text{ kJ/mol} \qquad (1.A)$$
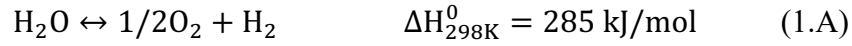
The water-splitting reaction is mostly carried out by electrolysis. In an ideal world, the energy used from performing the reaction comes from renewable energy sources. The produced hydrogen and oxygen can then be utilized in household or utilities. In such a scenario, carbon dioxide emission will be diminished to a minimal level or even zero. Early research conducted by Fujishima and Honda (Fujishima and Honda, 1972) induced a rise of the attention to this field. Recent demonstrations showed the production rate of hydrogen reaches 68 mmol/g/h with a semiconductor-coupled CdS/TiO_2 electrode (El-Maghrabi *et al.*, 2018). However, due to the energy required for water splitting is so high, as indicated in reaction 1.A, producing hydrogen from water splitting is hardly economically viable for current technologies.

Other than water, the most accessible source of hydrogen on earth is fossil fuel, and it is the most commonly used source for hydrogen production today. It is estimated that around 50% of the global hydrogen demand is met by natural gas steam reforming, 30% comes from oil reforming, 18% from coal gasification, 3.9% from water electrolysis, and 0.1% from other sources (Dincer and Acar, 2014). Currently, steam reforming of natural gas or steam reforming of methane (SRM) is still the most efficient method and produces hydrogen with the lowest cost (Dincer and Acar, 2014). The apparent downside of using fossil fuel is the inevitable CO_2 emission. However, none of the new technologies with significantly less carbon footprint is matured enough to produce hydrogen at a reasonable price (Service, 2004). According to the latest edition of BP Statistical Review

of World Energy (British Petroleum Co., 2019), fossil fuels (including oil, coal, and natural gas) still consists about 85% of the world's energy consumption. In contrast, renewables only account for 4%, as shown in **Figure 1.5**. It is expected that fossil fuel will still be the major energy source for the next few decades (Kennedy, 2004; Service, 2004). However, it is also noticeable that the share for natural gas has been steadily growing over the last 35 years. Producing hydrogen from natural gas produces the least amount of CO_2 and other pollutants compared with using oil or coal (Service, 2004). Therefore, producing hydrogen from natural gas can be a good temporary solution for carbon reduction before zero-emission technologies can take over.

Oil remains the most used fuel in the energy mix. Coal is the second largest fuel but lost share in 2018 to account for 27%, its lowest level in 15 years. The share of natural gas increased to 24% such that the gap between coal and gas has narrowed to three percentage points. The contribution of hydro and nuclear remained relatively flat in 2018 at 7% and 4%, respectively. Strong growth pushed up renewables share to 4%, just behind nuclear.

Figure 1.5*. Shares of global primary energy consumption by fuel (British Petroleum Co., 2019).*

Despite being the most energy-efficient hydrogen production method, due to the highly endothermic nature of SRM, it is still a very energy-intensive process. For commercial steam reformers, high temperature (700-1000 °C) and pressure (3-25 bar) are

usually required to achieve desirable methane conversion and production rate. The energy cost prevents hydrogen from being utilized as a major source of fuel. Therefore, studies of improving the energy efficiency of methane conversion to hydrogen, or specifically SRM, has drawn extensive research interests from academia.

In a commercial SRM unit, multiple reactions take place as follows:

$$CH_4 + H_2O \leftrightarrow CO + 3H_2 \qquad \Delta H^0_{298K} = 206 \text{ kJ/mol} \qquad (1.B)$$

$$CO + H_2O \leftrightarrow CO_2 + H_2 \qquad \Delta H^0_{298K} = \text{-41 kJ/mol} \qquad (1.C)$$

$$CH_4 + 2H_2O \leftrightarrow CO_2 + 4H_2 \quad \Delta H^0_{298K} = 165 \text{ kJ/mol} \qquad (1.D)$$
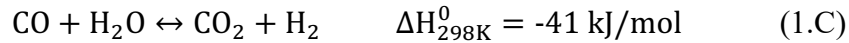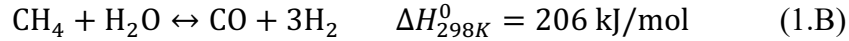
Reaction 1.C is also known as a water-gas shift (WGS) reaction. As indicated above, the reaction is mildly exothermic, and therefore it is not favored at high temperatures required by methane steam reforming (reaction 1.B and 1.D). This would render the product stream of an industrial methane reformer with a relatively high concentration of CO (~15% wet based). Typically, another WGS reaction unit has to be incorporated into the process to convert the remaining CO to H_2.

1.2. Applications of MIEC on Oxygen and Hydrogen Production

1.2.1. Adsorption-Based and Membrane-Based Oxygen Production

Ever since being commercialized by Linde in the early 1900s, cryogenic distillation has been the most prevalent air separation technology to this date. Although it is efficient in producing high purity oxygen and other noble gas, the process is very energy intensive as it requires compression and refrigeration of gases. Such energy cost makes this process only economically viable in large-scale operations (Yang, 1997; Smith and Klosek, 2001).

Due to the high capital cost and large facility footprint, cryogenic distillation is not very flexible to accommodate the need for many industries. Therefore, the search for alternatives has been carried out by both academia and industry.

Air separation can be very beneficial when applied to combustion-based power generation. Normally, for this application, high purity oxygen (>99%) is not required. Instead, adsorption-based air separation is a more suitable technique to supply a moderately high concentration (~95%) oxygen feed to the process (Yang, 1997; Smith and Klosek, 2001; Anheden, Yan and De Smedt, 2005), as shown in **Figure 1.6**. Pressure-swing adsorption (PSA) air separation has been developed for this kind of demand. The most common conventional sorbents are artificial zeolites 5A and 13X.
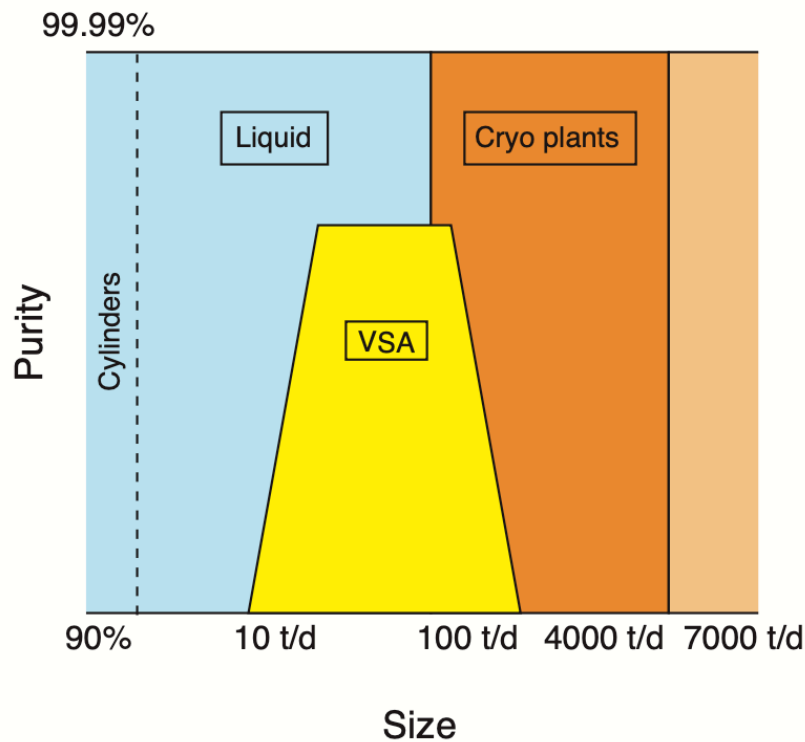
Figure 1.6. Oxygen production technology selection as a function of quantity (Anheden, Yan and De Smedt, 2005).

In general, zeolites consist of Na, Si, Al, and O atoms and have a microporous structure. Because nitrogen has higher quadrupoles than oxygen (0.31 Å to 0.1 Å), it has stronger interactions with the cations in the zeolite. As a result, these zeolites have stronger preferential adsorption towards nitrogen than oxygen, and air separation can be achieved by this selective adsorption property. Because the adsorption capacity of nitrogen is highly dependent on the cation species presented in the zeolite structure, early research efforts were focused on improving nitrogen adsorption capacity by substitution of cations in the zeolite structure. Research on Li-X zeolites conducted by Chao (Chao, 1989) and Baksh et al. (Baksh, Kikkinides and Yang, 1992) showed promising N_2 adsorption capacities and selectivities. Rege and Yang (Rege and Yang, 1997) also reported binary Li- and Ag-exchanged zeolite X sorbents, which shows excellent nitrogen to oxygen selectivities and adsorption capacities.

In addition to zeolites, carbon molecular sieve (CMS) is also a commonly used adsorbent for air separation. The feature of CMS is that it generally has a narrow pore size distribution (pore size normally around 4-9Å) (Deng, 2006). This property makes CMS adsorbents very useful when the gases need to be separated have very close molecular sizes. The development of CMS adsorbent is mature, and numerous patents have been filed since the 1970s (Munzner *et al.*, 1974, 1976; Grant, 1975; Sutt, 1986; Cabrera and Armor, 1991; Auvil, Schork and Srinivasan, 1993; Sircar, Rao and Golden, 1999). This type of adsorbent is mostly used for the generation of high-purity nitrogen in an industrial PSA process (Deng, 2006).

Despite the improvement, the most advanced zeolite can still only have a N_2/O_2 adsorption selectivity around 10 (Rege and Yang, 1997), as data shown in **Figure 1.7**. Also,

zeolites are not selective between argon and oxygen due to their similar polarizabilities (Sircar, Rao and Golden, 1999). This renders the highest purity of oxygen about 95-96% out of a zeolite-based adsorption device without other techniques combined. In fact, it will not be economical for a zeolite-based PSA process to even challenge to produce such high concentration oxygen. This limits the applicability and flexibility of the process. To further increase the efficiency of the PSA air separation process, a more selective adsorbent is desired.
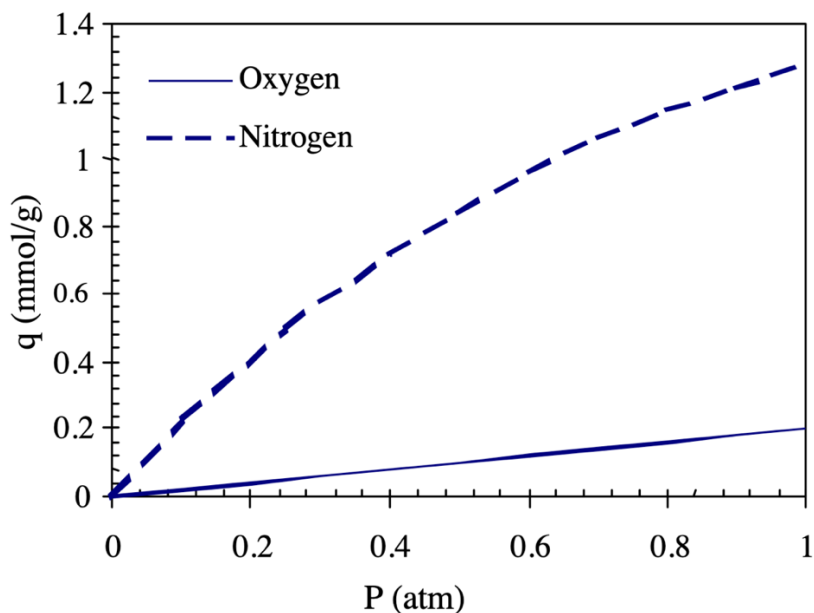
Figure 1.7. Comparison of adsorption capacities of nitrogen and oxygen on zeolite LiX (Rege and Yang, 1997).

Unlike the zeolites, which rely on interactions of gas molecules and surface cations to achieve separation, the oxygen sorption (adsorption and absorption considered as a single process) on perovskite materials is based on the structural oxygen defect and surface reactions. In high temperature (normally > 500 °C) conditions, oxygen ions in the

13

perovskite structure will have enough mobility to transport through the lattice oxygen defects. When the ambient oxygen partial pressure is high, i.e., the gas-phase oxygen chemical potential is higher than the oxygen chemical potential in the perovskite solid, the oxygen inflow will take place via defect surface reaction, resulting increase of the oxygen ion concentration in the solid. The reaction expressed in Kroger-Vink notation are as follows:

$$\frac{1}{2}O_2 + V_O^{\cdot\cdot} \rightarrow O_O^{\times} + 2h^{\cdot} \qquad (1.E)$$
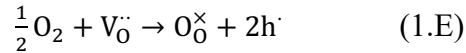
where $V_O^{\cdot\cdot}$ is oxygen vacancy, $O_O^{\times}$ is lattice oxygen and $h^{\cdot}$ is electron hole.

When the ambient oxygen pressure is low, the reverse reaction would take place, and the molecular oxygen will be released from the sorbent into the environment:

$$O_O^{\times} + 2h^{\cdot} \rightarrow \frac{1}{2}O_2 + V_O^{\cdot\cdot} \qquad (1.F)$$
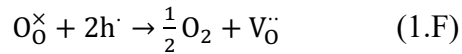
During the sorption and desorption process, the oxygen defect content, expressed as oxygen nonstoichiometry (δ), would change along the process and eventually reach equilibrium. The nonstoichiometry is the material's intrinsic property and the value of δ is determined by the thermodynamic state (temperature and pressure). By utilizing the difference of the nonstoichiometry ($\Delta\delta$), the sorbent can be useful in the PSA process for producing either nitrogen or oxygen. Since the emphasis of this research is the solution in the energy sector and carbon reduction, this research will only focus on the capability of oxygen separation of the sorbents.

Although it is logically sound to utilize the difference in oxygen content to achieve air separation, not every perovskite material has good sorption capacity. A common approach to increase the oxygen defect concentration (create more "room" for oxygen storage in the material) is metal ion doping. Generally, doping a cation with different ionic

14

sizes at either the A-site or B-site of the perovskite lattice would result in lattice distortion and create more defects. Since early 1980s, Mizusaki and coworkers (Mizusaki *et al.*, 1984, 1985, 1989, 1991, 1992; Ishigaki *et al.*, 1988; Mizusaki, 1992) conducted a series of research on the oxygen nonstoichiometric, ionic diffusion and electrical properties of a group of perovskite materials with a general formula of $La_xSr_{1-x}BO_{3-\delta}$ (B=Al, Zr, Bi, Cr, Mn, Fe, CO). These works provided valuable information about the effect of A-site doping on perovskite structure and proposed a defect model (Mizusaki *et al.*, 1985). In addition, Yamazoe and coworkers (Teraoka *et al.*, 1984, 1985; Zhang *et al.*, 1990) also carried out a systematic investigation for B-site cation doping effect on structure and oxygen sorption property of $La_{1-x}Sr_xCo_{1-y}Fe_yO_{3-\delta}$ (LSCF) oxides around the same time. The results gained much attention and later on inspired numerous studies on strontium cobaltite ($SrCoO_{3-\delta}$)-based perovskite ceramics (Qiu *et al.*, 1995; ten Elshof, Bouwmeester and Verweij, 1995; Kharton *et al.*, 1999; Wang, Cong and Yang, 2002; Liu *et al.*, 2006; He, Zhu and Yang, 2011).

While most research groups were focusing on membrane related research, Lin and coworkers (Yang and Lin, 2002; Yang, Lin and Zeng, 2002; Z. Yang and Lin, 2003) were the first to propose and demonstrate the concept of utilizing perovskite materials as sorbents in a PSA process. Their research started with an initial screening of several LSCF materials with different compositions. Two specific compositions, $La_{0.1}Sr_{0.9}Co_{0.5}Fe_{0.5}O_{3-\delta}$ (LSCF1955) $La_{0.1}Sr_{0.9}Co_{0.9}Fe_{0.1}O_{3-\delta}$ (LSCF1991) were found to have the largest sorption capacity (Yang, Lin and Zeng, 2002). Subsequent investigations using TGA and fixed-bed revealed detailed information about the sorbent, such as sorption isotherms (**Figure 1.8**) and breakthrough curves. More specifically, it was found that despite having fast sorption

15

rate, the desorption rate of LSCF1991 is rather slow. The phenomenon was observed as the "long tail" of the desorption breakthrough curve, as shown in **Figure 1.9**.

A cluster defect model was also developed in their works (Yang and Lin, 2002; Z. Yang and Lin, 2003) by a semi-empirical approach. The model was able to predict the nonstoichiometry (δ) and in different oxygen partial pressure. The nonstoichiometry is directly related to the oxygen sorption capacity and therefore the results were useful for the development of PSA process or device using perovskite sorbents.

The cluster defect model can be expressed as:

$$2B_B^{\cdot} + O_O^{\times} \leftrightarrow 2B_B^{\times} + V_O^{\cdot\cdot} + \frac{1}{2}O_2 \qquad (1.G)$$
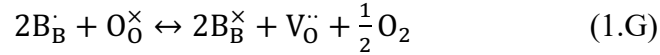
$$K_1 = \frac{\left[B_B^{\times}\right]^2 [V_O^{\cdot\cdot}]^2 Po_2^{1/2}}{\left[B_B^{\cdot}\right]^2 [O_O^{\times}]} \qquad (1.H)$$

$$2B_B^{\times} + O_O^{\times} \leftrightarrow \left[B_B^{'}\text{-}V_O^{\cdot\cdot}\text{-}B_B^{'}\right] + \frac{1}{2}O_2 \qquad (1.I)$$
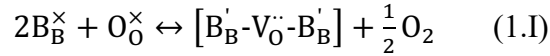
$$K_2 = \frac{[B_B^{'}-V_O^{\cdot\cdot}-B_B^{'}]Po_2^{1/2}}{\left[B_B^{\cdot}\right]^2 [O_O^{\times}]} \qquad (1.J)$$

where $B_B^{\cdot}$ and $B_B^{\times}$ are the B cation occupying the B-site in the lattice with single positive charge and neutral charge, respectively. $O_O^{\times}$ is lattice oxygen and $V_O^{\cdot\cdot}$ is oxygen vacancy. K_1 and K_2 are equilibrium constants for formula 1.G and 1.I.

Based on the results of Lin and coworkers, Guntuka et al. (Guntuka *et al.*, 2008) carried out an extensive investigation of sorption kinetics and modeling on fixed-bed for many LSCF compositions. Yin et al. (Yin and Lin, 2007; Yin, Kniep and Lin, 2008) conducted a series of investigations of the order-disorder phase transition phenomena of certain LSCF materials. The results showed that the materials with order-disorder phase transition have larger sorption capacity faster desorption rates. However, in the above

research, most of the results are from TGA and the bench-scale demonstration was not enough to estimate the potential utilizing the phase transition property. More recently, Miura and coworkers (Miura, Ikeda and Tsuchida, 2016) reported a $Sr_{1-x}Ca_xFeO_{3-\delta}$ perovskite sorbent exhibiting a sorption capacity about two times larger than the benchmark LSCF1991 sorbents. Despite having high sorption capacity, the desorption rate demonstrated in their work is still rather slow even with vacuum sweep.
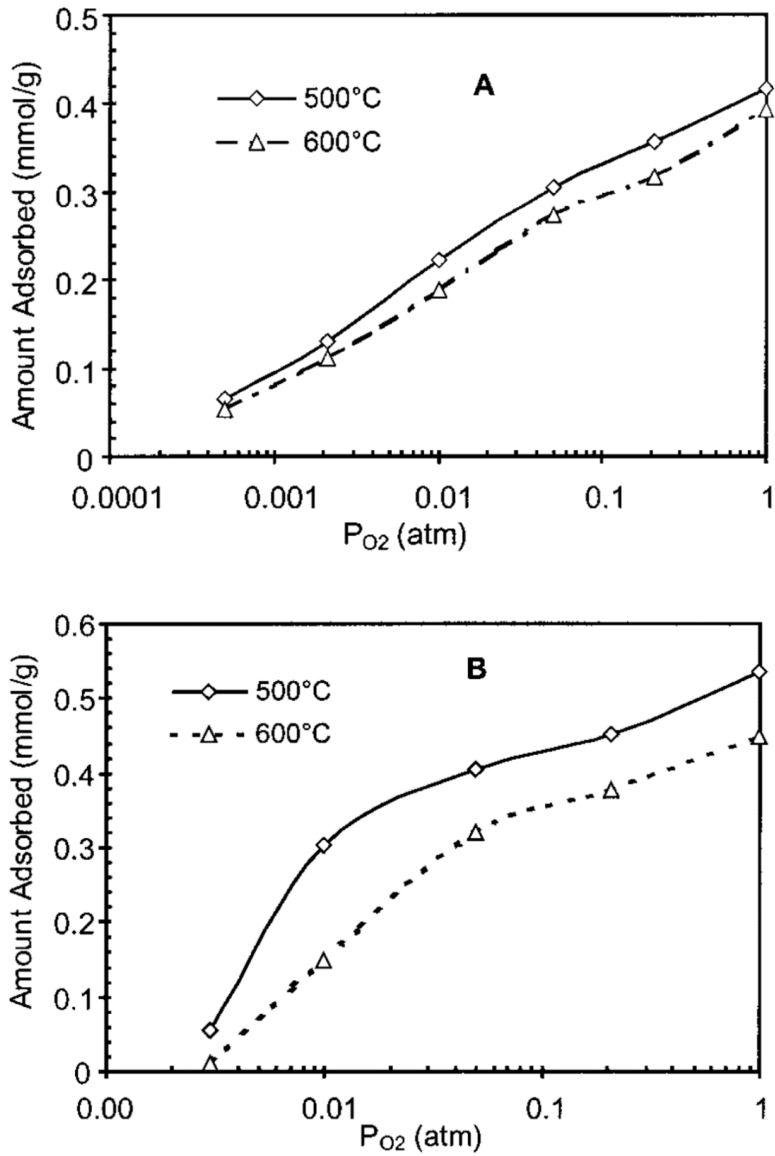
Figure 1.8*. Sorption isotherms of (A) LSCF1955 and (B) LSCF1991 at 500 and 600 °C (Yang, Lin and Zeng, 2002).*
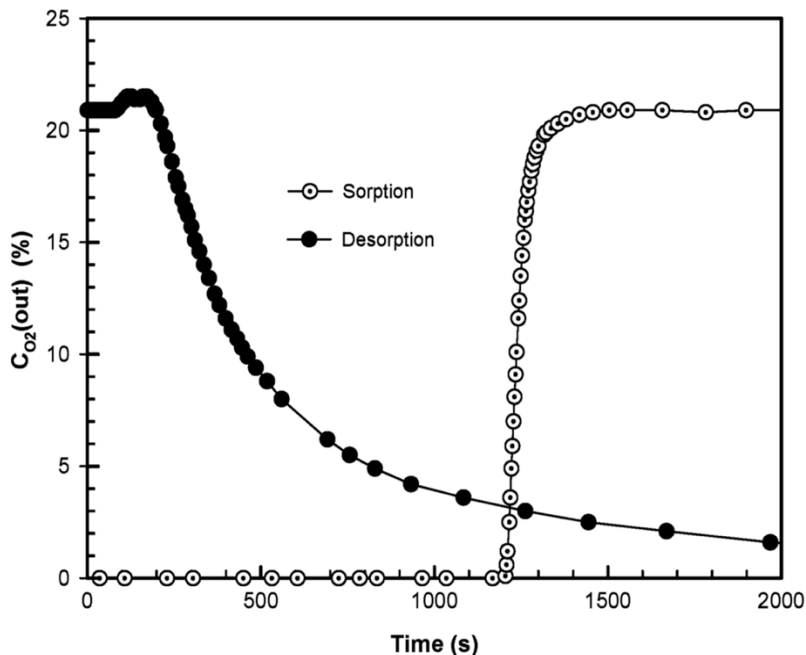
Figure 1.9*. Sorption and desorption curves of LSCF1991 at 800 °C. The long-tailing of the desorption curve indicates slower desorption rate* (Z. H. Yang and Lin, 2003)*.*

1.2.2. MIEC Membrane for O_2 and CO_2 permeation

The research community was particularly interested in using perovskite materials as oxygen-permeable membranes due to their potential application in fuel cells (Ishihara, Matsuda and Takita, 1994; Ishihara *et al.*, 2000; Petric, Huang and Tietz, 2000; Hilpert *et al.*, 2003; Sholklapper *et al.*, 2006). Over the past two decades, some perovskite materials with promising oxygen permeability have been reported, as given in **Table 1.1**. Most notably, Yang and coworkers (Shao *et al.*, 2000; Wang, Cong and Yang, 2002) first synthesized the $Ba_{0.5}Sr_{0.5}Co_{0.8}Fe_{0.2}O_{3-\delta}$ (BSCF) perovskite, which exhibiting exceptionally high oxygen flux and caught much attention from researchers in related fields. The materials development started with $SrCo_{0.8}Fe_{0.2}O_{3-\delta}$. The substitution of Sr by Ba, which has a larger ionic radius, significantly improved the oxygen permeability. The results were

19

followed by numbers of other groups and more promising results of Ba-doped perovskite were reported. Sunarso et al. also (Sunarso *et al.*, 2011) reported remarkably high oxygen permeation numbers (given in **Table 1.1**) of a $BaBi_{0.05}Sc_{0.1}Co_{0.85}O_{3-\delta}$ perovskite hollow fiber membrane. Shao and Haile (Shao and Haile, 2004) utilized BSCF as an electrode in a solid oxide fuel cell (SOFC) demonstration and showed an encouraging power density of $1010\ mW\ cm^{-2}$.

In addition to perovskite materials, fluorite materials were also studied for O_2-permselective membranes. Lin and coworkers (Han *et al.*, 1997; Han, Xomeritakis and Lin, 1997) successfully synthesized ultra-thin zirconia/yttria membranes by an electrochemical vapor deposition (EVD) technique. However, the oxygen flux was rather low ($\sim 10^{-9}\ mol\ s^{-1}\ cm^{-2}$). Later on, the same group (Akin, Lin and Zeng, 2001; Akin and Lin, 2002) developed a $Bi_{1.5}Y_{0.3}Sm_{0.2}O_{3-\delta}$ (BYS) membrane for oxidative coupling of ethane on a membrane reactor and rather high oxygen flux was reported (given in **Table 1.1**). In general, fluorite materials have lower oxygen permeability than perovskite materials partly due to their low electrical conductivity (Sunarso *et al.*, 2008). The electrical conductivity would affect the rate of the surface reaction of $O_2 + 2e^- \rightarrow O^{2-}$. However, some materials have been proven to have high oxygen ionic conductivity ($\sim 1.5\ S/m$), such as BYS, $Sm_{0.2}Ce_{0.8}O_{2-\delta}$ (SDC) and $Gd_{0.2}Ce_{0.8}O_{2-\delta}$ (GDC) (Kharton, Marques and Atkinson, 2004; Zienius *et al.*, 2017).

Table 1.1. *Representative MIEC membranes with high oxygen permeability.*

Material	Temperature (°C)	J_{O_2} (mol s^{-1}cm^{-2})	Type	Thickness (mm)	P'_{O_2} (atm)	P''_{O_2} (atm)	Reference
Ba$_{0.5}$Sr$_{0.5}$Co$_{0.8}$Fe$_{0.2}$O$_{3-\delta}$	800-900	7.07×10^{-7} to 2.31×10^{-6}	Perovskite	1.5	0.21	9.3×10^{-3} to 0.1147	(Wang, Cong and Yang, 2002)
BaTi$_{0.2}$Co$_{0.4}$Fe$_{0.4}$O$_{3-\delta}$	600-950	0 to 6.67×10^{-6}	Perovskite	1-2	0.21	–	(Tong *et al.*, 2003)
BaBi$_{0.05}$Sc$_{0.1}$Co$_{0.85}$O$_{3-\delta}$	600-950	1.02×10^{-7} to 7.76×10^{-6}	Perovskite	0.17	0.21	–	(Sunarso *et al.*, 2011)
Bi$_{1.5}$Y$_{0.3}$Sm$_{0.2}$O$_{3-\delta}$	825-875	4.40×10^{-7} to 6.36×10^{-7}	Fluorite	1.2	0.21	0.05 to 0.15	(Akin and Lin, 2002)
Ce$_{0.9}$Pr$_{0.1}$O$_{2-\delta}$– Pr$_{0.6}$Sr$_{0.4}$Fe$_{0.5}$Co$_{0.5}$O$_{3-\delta}$	800-1000	1.65×10^{-7} to 7.48×10^{-7}	Dual-phase perovskite	0.5-0.6	0.21	–	(Liang *et al.*, 2014)
Ce$_{0.85}$Gd$_{0.1}$Cu$_{0.05}$O– La$_{0.6}$Ca$_{0.4}$FeO$_{3-\delta}$	800-950	1.70×10^{-7} to 6.12×10^{-7}	Dual-phase perovskite	0.5	0.21	–	(Fang *et al.*, 2015)

More recently, several scale-up projects of air separation modules have been carried out with some encouraging results. Air Products and Chemicals, with the support from the U.S. Department of Energy (DoE), has successfully demonstrated an intermediate oxygen production of 100 tonne-per-day (TPD) by their proprietary ITM (Ion Transport Membrane) technology, according to their 2015 report (Armstrong, 2015). A similar project, the demonstration of OTM (Oxygen Transport Membrane) technology by Praxair, collaborated with U.S. DoE and National Energy Technology Laboratory (NETL), is also in progress (Li, 2018). Despite the recent progress, the membrane technology for air separation is still premature. On the contrary, PSA technology has been commercialized for decades, and currently, the production rate can reach 218 TPD with 95% oxygen purity in a commercial PSA unit (Chong *et al.*, 2016). Furthermore, the production cost of perovskite sorbent is expected to be much lower than perovskite membranes, as the membrane and the sealing of the module will require a very low tolerance of defects.

Therefore, in the near term, a perovskite sorbent-based PSA technology poses the greater potential for commercialization than membrane technology.

In addition to O_2-permselective membranes, ion-conducting ceramics have also been utilized for CO_2 separation. Lin and coworkers (Anderson and Lin, 2006, 2010; Ortiz-Landeros, Norton and Lin, 2013; Norton, Lu and Lin, 2014; Norton, Ortiz-Landeros and Lin, 2014) pioneered the research of carbonate-ceramic dual-phase membrane. The concept is to combine the oxygen ionic transport property of the ceramic phase and the carbonate ionic conductivity of the carbonate phase. The mechanism of CO_2 transport of this type of membrane is displayed in **Figure 1.10**. A ceramic-based dual-phase membrane consists of a porous ceramic support (the ceramic phase, purple in **Figure 1.10**) and a molten carbonate (mixture of Li_2CO_3/Na_2CO_3/K_2CO_3, yellow in **Figure 1.10**) phase filling the pores. When the membrane surface is exposed to CO_2, the CO_2 gas molecules will react with surface oxygen ions (O^{2-}) provided by the ceramic phase to become carbonate ions (CO_3^{2-}). The carbonate ion will then be driven by the pressure gradient across the membrane through diffusion in the molten carbonate phase. On the other side of the membrane, the reversed reaction will take place and CO_2 will be released to the environment and achieve permeation. Notable research of ceramic-MC membranes in recent years are summarized in **Table 1.2**.
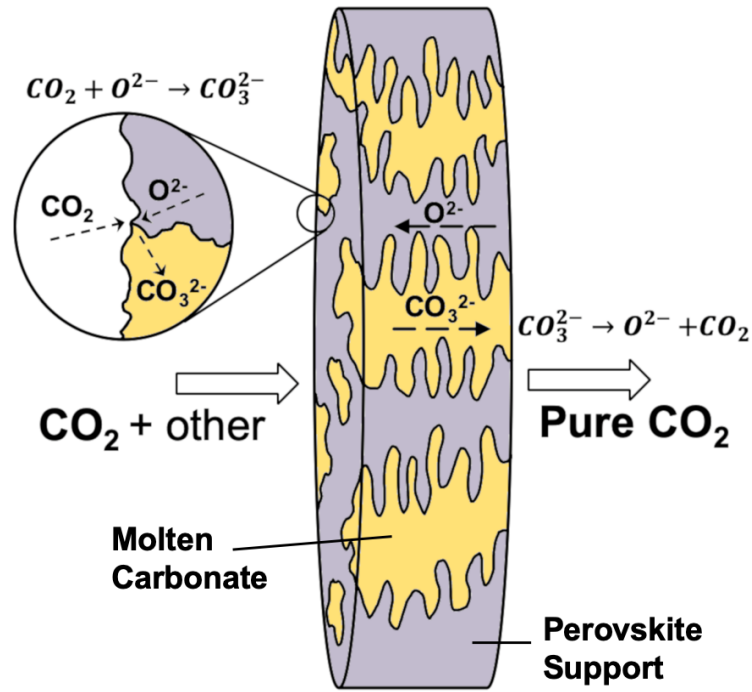
Figure 1.10. *Illustration of the CO₂ permeation mechanism of a ceramic-carbonate dual-phase membrane.*

Table 1.2. *Notable works of CO₂-permselective dual-phase membranes*

Material	Temperature (°C)	J_{CO2} (mol s^{-1} cm^{-2} Pa^{-1})	Thickness (mm)	P'_{CO2} (atm)	P''_{CO2} (atm)	Reference
$La_{0.6}Sr_{0.4}Co_{0.8}Fe_{0.2}O_{3-\delta}-$ carbonate	700-900	3.0×10^{-9} to 3.8×10^{-8} **(Permeance, mol s^{-1} cm^{-2} Pa^{-1})**	0.375-3.0	0.5	–	(Anderson and Lin, 2010)
$Ce_{0.8}Sm_{0.2}O_{2-\delta}-$ carbonate	700-900	1.36×10^{-7} to 5.85×10^{-7}	1.5	0.5	0.0036– 0.016	(Norton, Lu and Lin, 2014)
$Ce_{0.8}Sm_{0.2}O_{2-\delta}-$ carbonate	700-900	2.72×10^{-7} to 1.09×10^{-6}	0.15	0.5	–	(Dong, Ortiz-Landeros and Lin, 2013)
$Ce_{0.8}Sm_{0.2}O_{2-\delta}-$ carbonate	550-700	1.77×10^{-7} to 1.25×10^{-6}	1.2	0.48	–	(Zhang *et al.*, 2012)
$SrFe_{0.8}Nb_{0.2}O_{3-\delta}-$ carbonate	500-900	6.28×10^{-8} to 4.08×10^{-7}	0.22	0.5	6×10^{-3}	(Jiang *et al.*, 2016)

Despite showing promising permeation flux, the stability of the dual-phase membrane was not superior. Due to the usage of strongly basic alkaline earth metals, such as Sr and Ba, the membrane is prone to react with acidic gas, such as H_2S and CO_2. Several studies on CO_2/O_2 separation for oxy-fuel combustion have reported the instability of Ba-containing membranes (Arnold, Wang and Feldhoff, 2007; Li, Kerstiens and Markus, 2013; Yi, Weirich and Schroeder, 2013). Similarly, stability issues of LSCF-MC membranes have been reported despite having good CO_2 permeance (Norton, Ortiz-Landeros and Lin, 2014; Ravkina, Klande and Feldhoff, 2015). To address the issue, researcher started to focus on the development of CO_2-resistant materials. Partovi et al. (Partovi *et al.*, 2015) demonstrated that doping praseodymium into Sr-Co-Fe perovskite gives good stability to the membrane, and steady O_2 flux was reported when using pure CO_2 as a sweep gas. Yi et al. (Yi, Schroeder and Martin, 2013) took a B-site-doping approach and showed that $SrFe_{0.8}Nb_{0.2}O_{3-\delta}$ has excellent stability in CO_2. More recently, Zhu et al. (Zhu *et al.*, 2015) summarized previous research efforts and proposed a metal ion doping strategy for synthesizing CO_2-tolerant MIEC materials. Two perovskite oxides, $SrFe_{0.9}Ta_{0.1}O_{3-\delta}$ and $SrFe_{0.8}Sb_{0.2}O_{3-\delta}$, were developed based on the doping strategy and exhibit excellent stability when used as an O_2-permselective membrane with pure CO_2 sweep. These recent developments of CO_2-tolerant materials ensure the stability of dual-phase membranes in a CO_2-rich environment.

Multi-gas permeation is another new application of ceramic-MC membranes. The CO_2-O_2 co-permeation experiment conducted by Norton et al. (Norton, Ortiz-Landeros and Lin, 2014) proved that multi-species permeation can also be achieved with a non-porous dual-phase membrane. When the membrane surface is exposed to O_2 and CO_2 at the same

time, a significant increase in CO_2 permeation flux was observed (Norton, Ortiz-Landeros and Lin, 2014; Zhuang *et al.*, 2019). The reason is that the electronic conductivity facilitates the gas-phase reaction of $CO_2 + 0.5O_2 + 2e^- \rightarrow CO_3^{2-}$ and it becomes the predominant CO_2 permeation route as opposed to defect ionic reaction for oxygen. This work opened up the potential of various applications of MIEC-MC dual-phase membranes. For example, Fabián-Anguiano et al. (Fabián-Anguiano *et al.*, 2019) have used this co-permeation property to design a membrane reactor for dry methane reforming and partial methane oxidation in a single stage.

1.2.3. MIEC Membrane Reactors for Hydrogen Production

Because MIEC membranes offer excellent oxidative property, many researchers have found that MIEC membranes have the potential of being used as a hydrocarbon oxidative reactor for hydrogen production and numerous works have been carried out. Tsai et al. (Tsai *et al.*, 1997) were among the first to conduct the study of direct conversion of methane to syngas via partial oxidation of methane (POM) in a disc-type membrane reactor based on $La_{0.2}Ba_{0.8}Co_{0.2}Fe_{0.8}O_{3-\delta}$. In the demonstration, significantly higher methane conversion was observed when the catalyst (5% Ni/Al_2O_3) was packed directly on the membrane surface. The authors concluded that intimate contact of the catalyst and the membrane surface is critical to deplete surface oxygen ions and establish a high oxygen potential gradient for oxygen transport.

Yang and coworkers (Dong *et al.*, 2001; Shao *et al.*, 2001) later on carried out a series of research on POM in a $Ba_{0.5}Sr_{0.5}Co_{0.8}Fe_{0.2}O_{3-\delta}$ (BSCF) membrane reactor packed

with LiLaNiO/γ-Al$_2$O$_3$ catalyst. The membrane reactor was able to achieve 98.5% CH$_4$ conversion, 93.0% CO selectivity and 10.45 ml·cm^{-2}·min^{-1} oxygen permeation flux at 850 °C. The research also exhibited excellent stability of the membrane as it was able to hold up to 500 h of operation. However, other research groups reported membrane failure when working in POM conditions and concluded BSCF lacks stability (Balachandran *et al.*, 1995, 1997). Jin's and Caro's research group also conducted a systematic investigation of perovskite materials' application in a POM membrane reactor (Jiang *et al.*, 2008; Zhang *et al.*, 2008; Dong *et al.*, 2009; Wang *et al.*, 2009). More recently, Othman et al. (Othman, Wu and Li, 2015) reported a new type of composite hollow fiber consisting La$_{0.6}$Sr$_{0.4}$Co$_{0.2}$Fe$_{0.8}$O$_{3-\delta}$ and deposited with Bi$_{1.5}$Y$_{0.3}$Sm$_{0.2}$O$_{3-\delta}$ (BYS) for oxidative coupling of methane (OCM). The BYS deposited on the membrane surface served as the catalyst for the reaction, and conventional catalysts were not used in this work. The result showed that the membrane reactor was able to achieve 60% CH$_4$ conversion and 79% C$_{2+}$ compound selectivity.

As introduced in Chapter 1.1.3, SRM is the most commonly used technology for hydrogen production. To employ membranes in an SRM process, the membrane has to be capable of handling high temperature working conditions. By in situ removal of products (H$_2$ or CO$_2$), the reaction equilibrium can be shifted toward the product side and achieve process intensification. In the past decades, research activities were mainly concentrated on H$_2$-permselective membranes. Since the stoichiometry of hydrogen is the highest among all the gas components in the SRM reaction, it is intuitive that separation of hydrogen would have the most prominent effect to the reaction equilibrium. Due to the unique H$_2$-soluble property, palladium or palladium alloy membranes have been extensively studied

for hydrogen separation. A Pd-based membrane SRM reactor is shown in **Figure 1.11**. The hydrogen produced via the reforming reaction will permeate through the membrane, causing shortage of hydrogen in reaction chamber. The methane conversion is expected to increase without a temperature increase due to reaction shift.
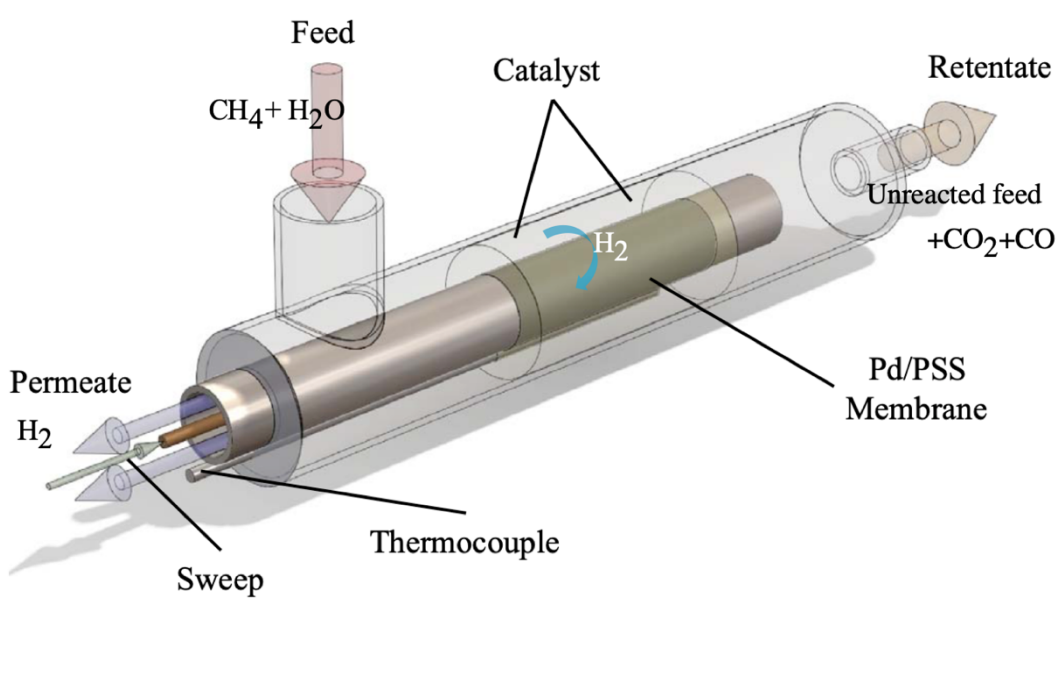
***Figure 1.11**. Illustration of Pd-based SRM membrane reactor. (Remade based on (Anzelmo, Wilcox and Liguori, 2017))*

Several types of Pd-based membrane designs were proposed to reduce the usage of the pricy palladium. For example, Gallucci et al. (Gallucci *et al.*, 2004) demonstrated a Pd-Ag dense alloy membrane and achieved 22-62% CH_4 conversion at 350-450 °C with 122 kPa feed pressure. Besides dense metal membranes, composite membranes with porous support were also developed. Kikuchi et al. (Kikuchi, Uemiya and Matsuda, 1991) proposed a Pd-alumina composite membrane that can achieve 64% CH_4 conversion at 400 °C with 100 kPa feed pressure and vacuum at the permeate side. Tong et al. (Tong *et al.*, 2005) fabricated a thin Pd-based membrane with porous stainless-steel support (Pd/PSS).

The demonstration showed a high methane conversion of 84-98% at 450-550°C with 300 kPa feed pressure. However, the high material cost and instability of Pd prevent these membranes from being utilized in real industrial processes. Dolan et al. (Dolan *et al.*, 2006) reported susceptibility of Pd-based membranes to CO and other sulfur-containing trace compounds. More recently, in the stability test conducted by Anzelmo et al. (Anzelmo, Wilcox and Liguori, 2017), H_2/Ar selectivity of the Pd/PSS membrane dropped significantly after 250 h of performing steam reforming. The membrane failure was suspiciously due to grain growth after extended testing (Kumpmann, Günther and Kunze, 1993; Bryden and Ying, 1995).

Apart from Pd-based membranes, microporous silica-based membranes were also applied to SRM or WGS membrane reactors (Giessler *et al.*, 2003; Tsuru *et al.*, 2004; Brunetti *et al.*, 2007; Akamatsu *et al.*, 2011; Meng and Tsuru, 2016). Although the price of fabricating these membranes is lower, the H_2/CO_2 selectivity of these is not desirable compared with Pd-based membranes. Another downside of H_2 separation, in general, is that the produced H_2 is collected at the permeate side with low pressure, which would require extra energy for compression prior to subsequent transport and utilization.

Modeling and simulation studies are very valuable for membrane reactor development. The modeling and simulation results would offer great convenience in assessment of reactor performance in real industrial conditions and for scale-up. Based on the work of Tsai et al. (Tsai *et al.*, 1997), Jin et al. (Jin *et al.*, 2000) extended the study on $La_{0.2}Ba_{0.8}Co_{0.2}Fe_{0.8}O_{3-\delta}$ membrane reactor for POM and developed a model which can well predict CH_4 and conversion and H_2/CO ratio in the product. Tsuru et al. (Tsuru *et al.*, 2004) demonstrated SRM in a microporous silica catalytic membrane reactor and a dimensionless

model was used to assess the performance of the membrane reactor. As Pd-based membranes were well-studied experimentally and much information were already available, numerous simulation works, including economic evaluation, on Pd-based membrane have been carried out (Lin *et al.*, 2003; Patel and Sunol, 2007; Ma *et al.*, 2015, 2017).

1.3.   Problem Statement, Research Objectives and Structure of Dissertation

1.3.1.   Problem Statement and Research Objectives

The previous research works on material science or applications of MIEC materials have laid down a solid foundation for future research. Although it is encouraging that some proprietary membrane technologies are on the way of commercialization, such as ITM of Air Products, OTM of Praxair, the potential of MIEC oxides are still to be explored.

The perovskite and fluorite structure are highly tailorable. Therefore, numerous new compositions have been created over the past few decades. While some of the new compositions showed great properties in preliminary demonstrations, in-depth investigation and bench-scale process demonstrations are often lacking. In order to better assess the potential of the MIEC materials in a real industrial process, more detailed process demonstrations have to be carried out.

For new air separation process development, some promising results of perovskite membranes have been reported. However, high level of technical difficulties has been found in the fabrication high-quality membrane and the high-temperature sealing in terms of meeting industrial standards. The concept of perovskite sorbents was proposed to

circumvent the above problems while utilizing the oxygen transport properties of perovskite materials. Since the concept is relatively new, there are not many related works at this point. A complete assessment of comparing perovskite sorbent and perovskite membrane processes for air separation, or more specifically, oxygen production, can only be carried out when sufficient research results have been reported. Therefore, the investigations on both fundamental oxygen transport properties and the performance of a bench-scale sorption column were carried out in order to gain insights.

Ceramic-carbonate dual-phase membranes have attracted much attention from the research community since the concept was proposed. Over the past decades, some of the perovskite materials used in early research works have been found to be unstable when subjected to a CO_2-rich environment. Therefore, the search for CO_2-resistant materials for the next generation dual-phase membrane is essential. While numbers of works on CO_2-resistant perovskite have been reported in the literature, few dual-phase membrane demonstrations were performed. Moreover, the concept of multi-gas permeability of dual-phase membranes has only been reported by Lin and coworkers (Norton, Ortiz-Landeros and Lin, 2014). This technology has the potential to expand the applicability of dual-phase membranes further to the future industrial process. The investigation of the interactions between CO_2 and O_2 permeation and how the geometric factors of the membrane will affect the permeation is worth exploring.

As fossil fuel is projected to be the main hydrogen source for the next few decades, it is crucial to come up with innovations to improve current industrial processes. As mentioned above, despite being the most efficient hydrogen production process, SRM is still very energy-intensive due to the nature of the chemical reactions. While past research

on Pd-based membranes effectively maintained high methane conversion with reduced temperature, the drawbacks, such as material cost and membrane stability, have prevented them from commercialization. The approach of CO_2-removal poses several advantages over Pd-based membrane reactor. Not only the CO_2-permselective reactor can maintain high hydrogen pressure in the product, but also achieve pure CO_2 separation simultaneously in single stage. However, due to it is only reported by Lin and coworkers (Dong and Lin, 2016; Wu, Rui and Lin, 2020), the effectiveness of the membrane reactor still needs be proven with more research results. Therefore, the dissertation is to present the latest findings in a demonstration of a ceramic-carbonate membrane reactor performing SRM. A mathematical model was also developed based on the experiment results. The modeling results not only provided the information needed for reactor performance assessment, but also will be beneficial for future membrane reactor development.

1.3.2. Structure of Dissertation

This dissertation covers two main parts. The first part is focused on perovskite and fluorite materials as oxygen sorbents and membrane for oxygen and CO_2 separation. The second part is centered at experimental and modeling studies about the membrane reactor for hydrogen production. For both oxygen and hydrogen production processes, the core mechanism is directly related to the oxygen transport property of the MIEC materials. More specifically, Chapter 2 is a detailed study of the oxygen transport phenomenon of perovskite-type sorbents in both TGA and fixed-bed conditions. Chapter 3 presents research on a new type of ceramic-carbonate dual-phase membrane, which is capable of

performing CO_2-O_2 counter-permeation. Detailed oxygen and CO_2 transport and the effect of membrane geometric factors are investigated. Chapter 4 extended the research towards a more application-oriented aspect with a demonstration of a CO_2-removal SRM membrane reactor. Based on the results of Chapter 4, a mathematical model was proposed in Chapter 5. The mathematical model provides useful information about membrane reactor performing under some conditions difficult to carry out in a laboratory, such as high pressure SRM reaction.

CHAPTER 2

AIR SEPARATION BY PEROVSKITE SORBENTS WITH OXYGEN VACANCY
ORDER-DISORDER PHASE TRANSITION

2.1.   Introduction

As mentioned in Chapter 1.2.1, cryogenic distillation is highly energy-intensive and requires large scale plant to make it economically viable. For some industrial processes, such as oxy-fuel combustion, cryogenic distillation may not be cost-effective to produce the required oxygen. Therefore, the high temperature air separation processes based on pressure-swing adsorption (PSA) or oxygen-permeable membrane are considered as good alternatives over cryogenic distillation.

Among the large variety of perovskite oxides, $La_{1-x}Sr_xCo_{1-y}Fe_yO_{3-\delta}$ (LSCF) are of specific interest to researchers for applications such as membranes or sorbents for air separation and electrodes of solid oxide fuel cells (Lin *et al.*, 2005; Sunarso *et al.*, 2008; Zhang *et al.*, 2008). Teraoka et al. were the first to demonstrate the oxygen permeation through various compositions of LSCF materials and showed the possibility of practical use (Teraoka *et al.*, 1985). On the other hand, Yang et al. (Yang, Lin and Zeng, 2002; Z. H. Yang and Lin, 2003) were the first to show potential applications of LSCF sorbents in industrial PSA processes by conducting thermogravimetric analysis (TGA) and bench-top scale fixed-bed oxygen sorption/desorption experiments with $La_{0.1}Sr_{0.9}Co_{0.9}Fe_{0.1}O_{3-\delta}$ (LSCF1991) and $La_{0.1}Sr_{0.9}Co_{0.5}Fe_{0.5}O_{3-\delta}$ (LSCF1955). LSCF sorbent-based fixed-bed oxygen sorption were then followed by Guntuka et al. (Guntuka *et al.*, 2008; Guntuka, Farooq and Rajendran, 2008). While focusing on column kinetics and modeling, the reported sorption capacity, sorption and desorption breakthrough curves profiles of

LSCF1991 agrees well with Yang's early results and further showcased the potential of these materials as sorbents for air separation.

Different from activated carbon or zeolite, which physically adsorb nitrogen from the air, the LSCF sorbents only adsorb oxygen and thus theoretically have infinite selectivity for oxygen over nitrogen. Under such a scenario, the desorption efficiency of oxygen becomes the key factor for industrial application, as oxygen is more desirable than nitrogen in energy production processes. Research conducted by Yang et al. (Yang and Lin, 2003) and Guntuka et al. (Guntuka, Farooq and Rajendran, 2008) showed strongly-favorable type oxygen adsorption isotherm and "long-tailing" desorption breakthrough curve of LSCF1991, which indicates slow desorption rate. To make the LSCF sorbent-based PSA practical, the oxygen desorption efficiency has to be improved.

Yin et al. (Yin and Lin, 2007; Yin, Kniep and Lin, 2008) observed that in the gravimetric study some of the LSCF sorbents, for example, LSCF1991, exhibit enhanced oxygen desorption rate, and attributed this phenomenon to the presence of oxygen vacancy disorder-order transition during the desorption process. With the presence of disorder-order transition, the desorption of LSCF1991 in TGA reached equilibrium at 1500 to 2000 seconds at the temperature range of 600-800°C, as compared with more than 4000 seconds of desorption time for $La_{0.5}Sr_{0.5}CoO_{3-\delta}$ (LSC55), which is without disorder-order transition (Yin and Lin, 2007).

The disorder-order transition refers to a phenomenon that oxygen vacancies of the metal oxide transform from a disordered (perovskite) to an ordered (brownmillerite) structure, while order-disorder transition refers to the reverse transition process. Early research conducted by Qiu et al. and Liu et al. (Qiu *et al.*, 1995; Liu *et al.*, 1996) discovered

the phase transition of $SrCo_{0.8}Fe_{0.2}O_{3-\delta}$ (SCF82) and proposed a phase diagram based on

TGA results. A descriptive LSCF1991 phase diagram was proposed by Yang et al. (Yang

and Lin, 2005) following the same rationale, as shown in **Figure 2.1**. It is noteworthy that

the brownmillerite region is theoretically limited at $(3-\delta) = 2.5$ since the oxygen vacancies

are immobilized by electrostatic force in the ordered state (Goodenough, 2004). Therefore,

the oxygen nonstoichiometry (δ) does not change with temperature when the material is

equilibrated in the ordered state. In addition, in low oxygen partial pressure environment

LSCF1991 may transform from brownmillerite to perovskite as the temperature increases

above the phase transition temperature.
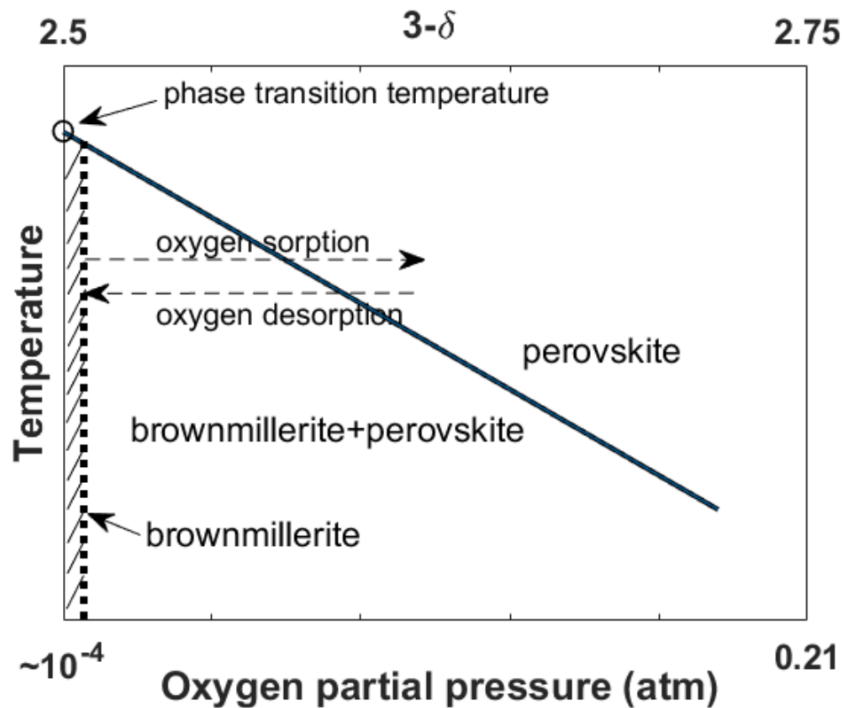
Figure 2.1*. Descriptive phase diagram of LSCF1991.*

The concept of manipulating the oxygen vacancy order-disorder transition in a PSA air separation process is explained by the dashed arrows in **Figure 2.1**. At a certain temperature, switching gas surrounding LSCF1991 between air (P_{O2}=0.21atm) and a purge gas (or vacuum) (P_{O2}=1.3×10^{-4} atm), the perovskite oxide adsorbs or desorbs oxygen and the δ value changes accordingly. As discussed above, Yin et al. (Yin and Lin, 2007; Yin, Kniep and Lin, 2008) reported significantly enhanced oxygen desorption rate when the surrounding gas is switched from air to a purge gas for LSCF1991 with disorder-order transition. However, it was not clear if such disorder-order transition assisted oxygen desorption rate could help achieving fast oxygen desorption breakthrough curve in the fixed-bed processes. The objective of this work is to conduct a comparative study on oxygen desorption in the gravimetric and fixed-bed processes to better understand the oxygen vacancy disorder-order transition phenomenon and to assess if it can be advantageously used to improve fixed-bed air separation process.

2.2. Experimental

The perovskite oxides were prepared by liquid citrate method. Stoichiometric amount of La(NO$_3$)$_3$·6H$_2$O, Sr(NO$_3$)$_2$, Co(NO$_3$)$_2$·6H$_2$O, and Fe(NO$_3$)$_3$·9H$_2$O (Alfa Aesar, at least 98% of purity) were dissolved in deionized water with 20% excess of citric acid. The solution was under heating and stirring at 130°C during polymerization and condensation reaction for at least 8 hours. After condensation the solution was heated to 200°C to evaporate excessive water. A viscous, dark orange gel-like product was obtained at the end of evaporation. The gel-like product was then heated to 400°C to induce self-ignition for removing organic content in the mixture. The resulting black waffle-like solids

were hand-ground in a mortar, and then sintered at 1250°C in air for 20 hours, with a ramping and cooling rate of 2°C/min.

Three representative compositions of the perovskite-type ceramics were studied in this work: $La_{0.1}Sr_{0.9}Co_{0.9}Fe_{0.1}O_{3-\delta}$ (LSCF1991), $La_{0.1}Sr_{0.9}Co_{0.6}Fe_{0.4}O_{3-\delta}$ (LSCF1964), and $La_{0.2}Sr_{0.8}Co_{0.6}Fe_{0.4}O_{3-\delta}$ (LSCF2864). LSCF1964 was manufactured by Treibacher Industrie AG, and the other materials were synthesized by the method described above. Additional hand grinding might be needed if the sintered compound were aggregated into clusters. The sintered powders were ball-milled with hexane at 14 Hz for about 15-20 h to reduce the size of the particles to less than 5 μm. The particle morphologies and sizes were examined by scanning electron microscope (SEM). High resolution powder X-ray diffractometry (XRD) (PANalytical X'Pert Pro, CuKα1 radiation) was used to examine the structure of the materials. The diffraction spectra were collected in the range of $2\theta = 20°$-80°. Besides the regular powder X-ray diffraction, in-situ high temperature XRD were also conducted to study the high temperature phase structure of LSCF1991. The in-situ high temperature set-up consisted of a heating platform and a polymer vacuum dome with vacuum less than 2.7×10^{-7} bar during the measurements.

The phase transition temperature and oxygen sorption/desorption property were recorded by thermal gravimetric analysis/differential scanning calorimetry (TGA/DSC, TA Instrument, SQT600). In each experiment run 20 ± 0.5 mg of sample powder was loaded. To measure the phase transition temperature, TGA/SDC measurement was performed with temperature ramping up from room temperature to 950°C in a ramping rate of 5°C/min in the flow of nitrogen (industrial grade, $P_{O2}\sim10^{-4}$) at 100 ml/min. In oxygen sorption/desorption experiments on the TGA/DSC instrument, breathing grade air (Praxair)

and industrial grade nitrogen (Praxair, 99.995%) were used as sorption/desorption gases. Transient sorption/desorption weight increase/decrease curves were determined at a given temperature in the range from 500°-800°C. Generally, the sorption transient increase curves took about 40 min, while the desorption ones could take up to 2 h to reach the equilibrium.

The oxygen nonstoichiometry of fresh samples in air at room temperature (δ_0) were obtained by a reduction experiment in the same TGA instrument aforementioned. The samples were reduced at 850°C in the flow of 10%H_2/90%He at 100ml/min. The value of δ_0 can be calculated based on the stoichiometry of the reduction reaction. For example, the δ_0 value of LSCF1991 can be calculated through the following equation:

$$\delta_0 = \frac{1.95M_O - 3xM_O - x(0.1M_{La} + 0.9M_{Sr} + 0.9M_{Co} + 0.1M_{Fe})}{(1-x)M_O} \qquad (2.1)$$

Which is based on the reduction reaction:

$$La_{0.1}Sr_{0.9}Co_{0.9}Fe_{0.1}O_{3-\delta} \rightarrow 0.05La_2O_3 + 0.9SrO + 0.9Co + 0.1Fe + \left(\frac{1.95-\delta}{2}\right)O_2 \quad (2.A)$$
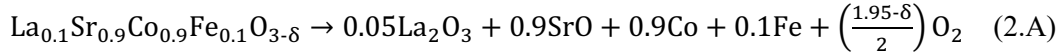
where $x = (W_i - W_f)/W_i$ with W_i and W_f being the sample weight before and after the reduction, respectively. M_i is the atomic weight of the element i. With known δ_0 value, the absolute value of δ at any moment during the sorption or desorption process can be determined from the change of the sample weight with respect to which in air at the room temperature. The oxygen adsorption amount at given oxygen partial is calculated from the oxygen nonstoichiometries at that pressure and the reference atmosphere (e.g. nitrogen) by:

$$q = -\frac{\delta(P_{O_2}) - \delta(P_{O_2(ref)})}{M_s} \qquad (2.2)$$

where M_s is the average molecular weight of the perovskite sorbent.
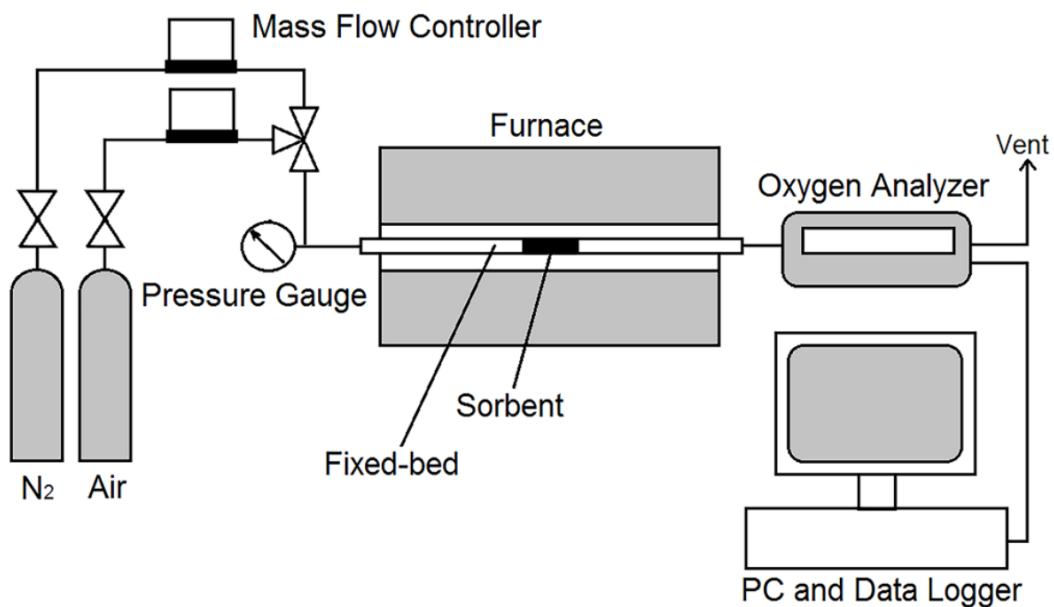
Figure 2.2*. Schematic diagram of the fixed-bed experiment set-up used in this work.*

Figure 2.2 shows the schematic of the fixed-bed system used in this work. The sorption column was made of an alumina tube with 0.6 mm i.d. and 0.9 mm o.d. 2 g of the perovskite powder were packed in the fixed-bed column for each experiment. The packing length was about 5 cm. Industrial grade nitrogen (Praxair, 99.995%) and breathing grade air (Praxair) were used in the experiment. Gas flow rates were controlled by two mass flow controllers for nitrogen and air, respectively, and both streams were calibrated at 5 ml/min. A pressure gauge was installed on the feed side to ensure no significant pressure difference across the bed. Gas switching was implemented by a 3-way valve. Before the experiment the fixed-bed was heated to the target temperature and held at the temperature for at least 10 h to ensure the sample reaching the steady state. The oxygen concentration of the effluent during sorption/desorption was measured by an oxygen analyzer (Systech Illinois, ZR800) as a function of time. The dead volume of the system was determined as 10 ml. In

order to study the phase transition property of the sorbents in fixed-bed, the samples were quenched after 2 h of desorption at 600°C and examined by HT-XRD. Quenching was done by pulling out the aluminum tube containing the perovskite out of the furnace rapidly followed by cooling in air with a fan.

2.3. Results and Discussion

The morphologies of the perovskite oxide particles are shown in **Figure 2.3**. The particles are dense and the particle size is in the range of 1-5 μm. XRD patterns of the three samples oxides are of typical perovskite structure, as shown in **Figure 2.4**. The oxygen nonstoichiometry of the samples in air at the room temperature (δ_0) was determined to be 0.168, 0.134 and 0.212 for LSCF1991, LSCF1964 and LSCF2864, respectively. DSC spectra for the three samples are shown in **Figure 2.5**. The endothermic peak of LSCF1991 heat flow at 846°C indicates the occurrence of oxygen vacancy order-disorder phase transition, whereas there is no phase transition observed from the heat flow data of LSCF1964 and LSCF2864. This is consistent with the previous results (Yang, Lin and Zeng, 2002; Z. H. Yang and Lin, 2003; Yin and Lin, 2007) that the LSCF perovskites with lower iron content in the B site tend to have oxygen vacancy order-disorder phase transition characteristics.
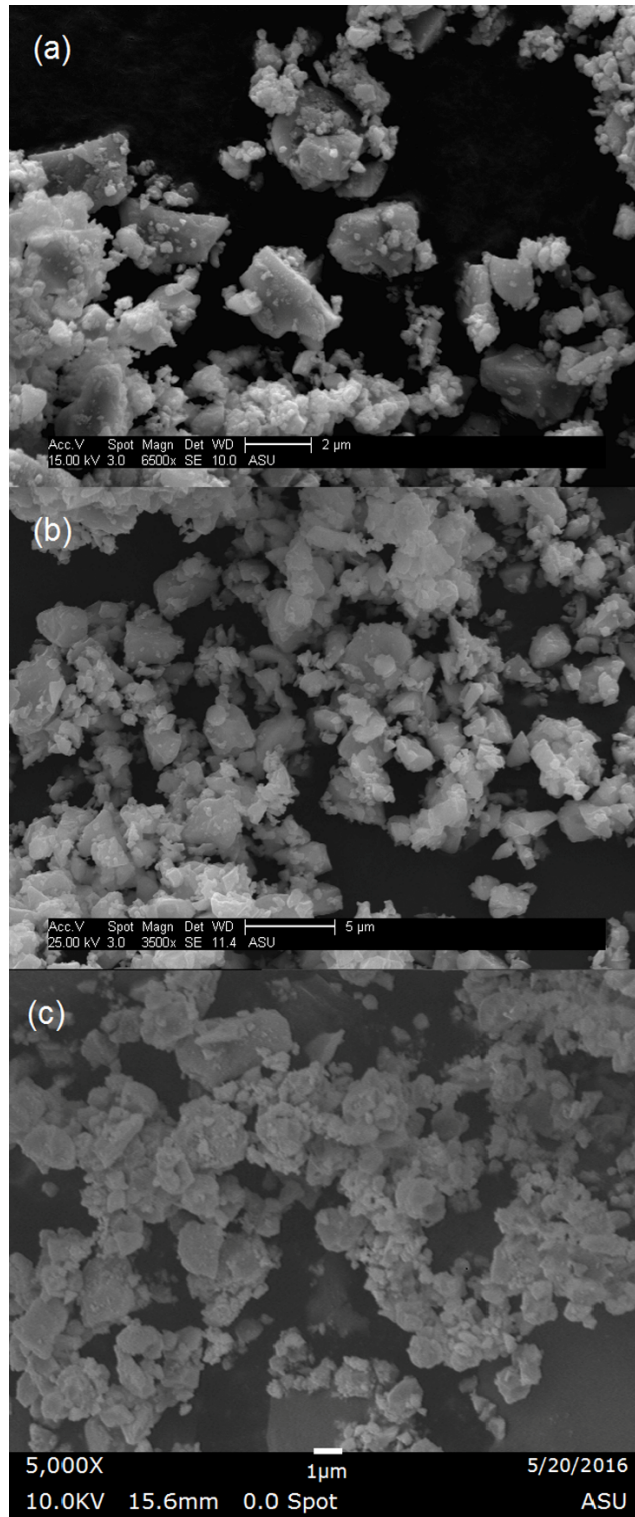
Figure 2.3. SEM images of (a) LSCF1991 (b) LSCF1964 and (c) LSCF2864 particles prepared by ball-milling.
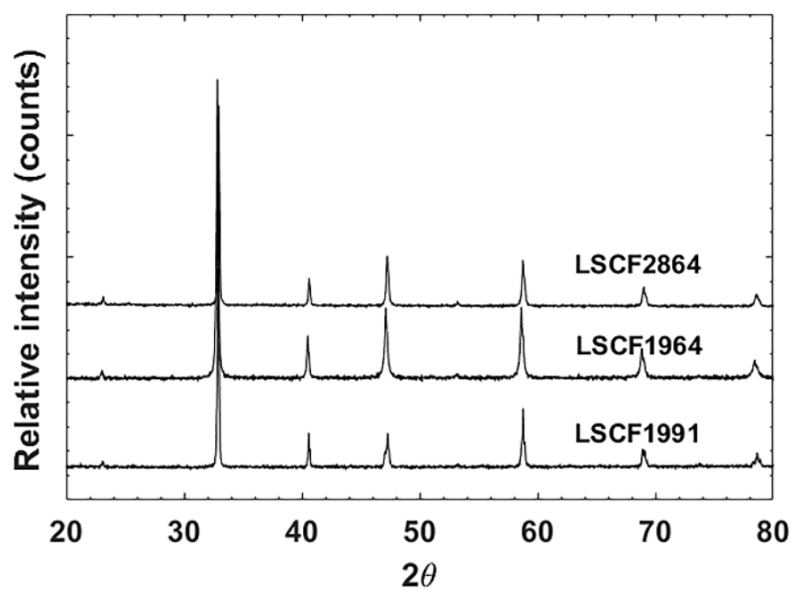
Figure 2.4*. XRD spectrums of the LSCF oxides studied in this work.*
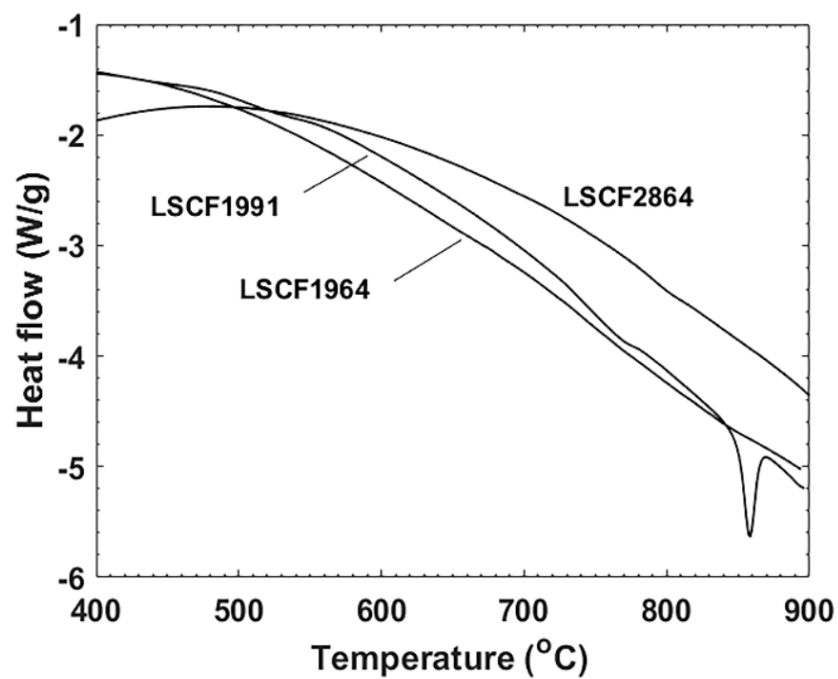
Figure 2.5*. DSC heat flow pattern of the LSCF perovskite oxides in temperature ramping.*

42
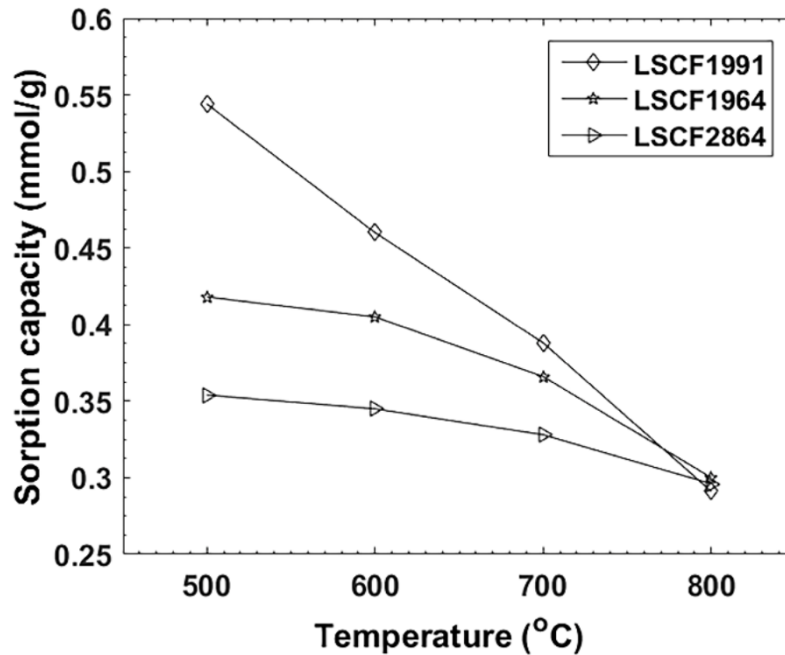
Figure 2.6*. Oxygen sorption capacities in air of the LSCF perovskite oxides studied in this work.*

The oxygen sorption/desorption capacity data measured in TGA are shown in **Figure 2.6**. At 800°C, the sorption capacities of the three materials are almost the same. However, LSCF1991, which has lower iron content, shows highest sorption capacities at temperatures from 400-700°C. In addition, the sorption capacity of this material decreases with increasing temperature. The other two materials with lower iron content show lower sorption capacities. The sorption capacities of all these three materials decrease with increasing temperature in this temperature range.

Figure 2.7 (a)-(d) show transient data of oxygen desorption in 500-800°C in air/nitrogen switching condition. Among the three materials, LSCF1991 has better desorption performance than the other two materials in the TGA tests. As shown in **Figure 2.7**, the transient weight curves of LSCF1991 have a sharp turn at all the four temperatures with shortest time to reach equilibrium as compared with other two samples. For example,

in **Figure 2.7 (a)** the desorption rate increases at around 22 min and it reaches equilibrium at 45 min, while the other two materials without phase transition characteristics show slower desorption and do not reach equilibrium even after 2 h.
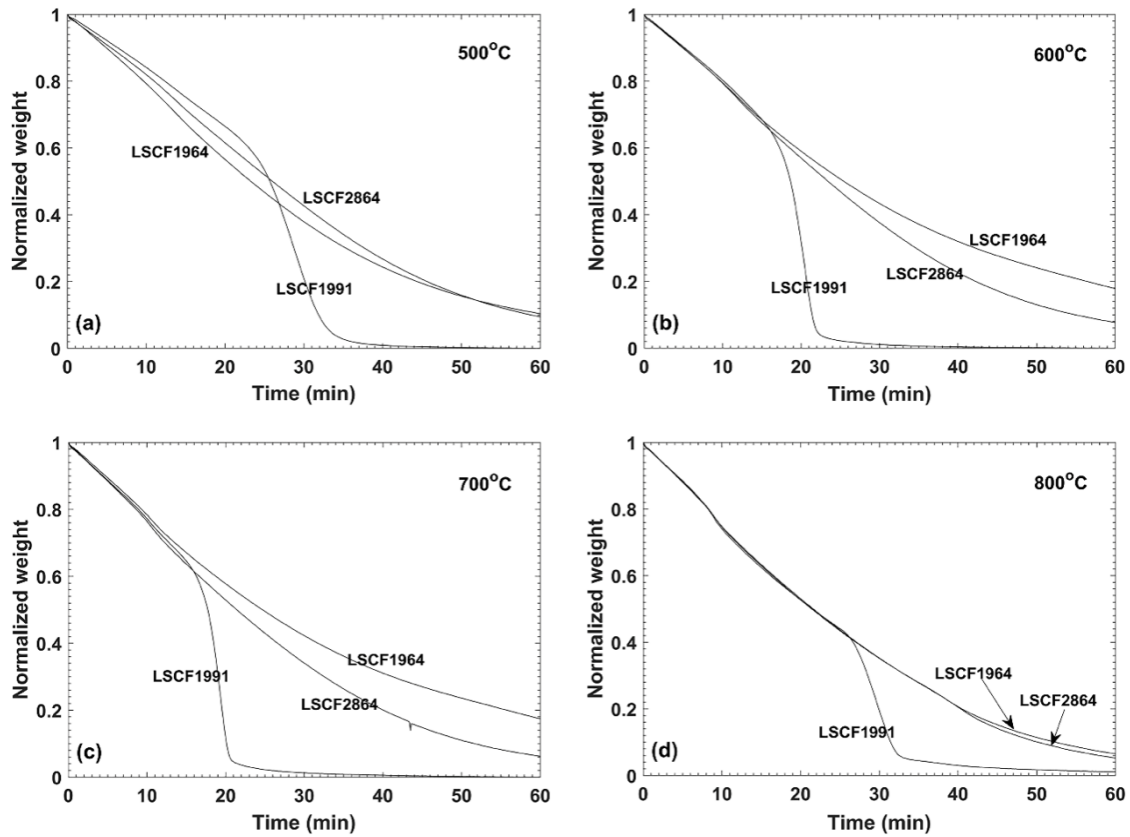
Figure 2.7. *Oxygen desorption of LSCF perovskite oxides in TGA at (a) 500°C, (b) 600°C, (c) 700°C, (d) 800°C.*

Table 2.1. *TGA and Fixed-bed sorption capacity data for perovskite oxides investigated in this work*

Temperature (°C)	LSCF1991		LSCF1964		LSCF2864	
	Sorption capacity tested in TGA	Sorption capacity tested in fixed-bed	Sorption capacity tested in TGA	Sorption capacity tested in fixed-bed	Sorption capacity tested in TGA	Sorption capacity tested in fixed-bed
500	0.544	0.569	0.418	0.429	0.354	0.394
600	0.460	0.467	0.405	0.403	0.345	0.384
700	0.388	0.374	0.366	0.350	0.328	0.323
800	0.291	0.285	0.300	0.293	0.296	0.295

(all in mmol/g)

Fixed-bed experiments were conducted to evaluate if the disorder-order transition enhanced desorption rate observed from the TGA described above would impact on oxygen separation in dynamic processes. **Figure 2.8** shows the fixed-bed sorption breakthrough curves in 500-800°C for LSCF1991, LSCF1964 and LSCF2864, respectively. The sorption capacity of a breakthrough curve can be calculated from the following mass balance equation:

$$q = \frac{F_i X_i P_i t_f}{RTm_s} - \frac{1}{RTm_s} \int_0^{t_f} F_o(t) X_o(t) P_o \, dt \qquad (2.3)$$

where

$$F_o(t) = \frac{F_i(1-X_i)}{1-X_o(t)} \qquad (2.4)$$

in which m_s is the amount of sorbent packed in the column, F, X and P represent the volumetric flow rate, oxygen molar fraction and total pressure, respectively. Subscripts i and o indicate the inlet and outlet condition, respectively. The sorption capacities calculated from the breakthrough curves are consistent with TGA results, as shown by the data listed in **Table 2.1**.

It is also noteworthy that the onset time of the phase transition decreases when the temperature was increased from 500 to 700 °C. However, the onset time increases when the temperature increased to 800 °C. The cause of this phenomenon is the high temperature phase transition from brownmillerite to perovskite. As shown in **Figure 2.5**, the order-disorder phase transition occurred at about 846 °C. Based on the data, we speculate that the phase structure of LSCF1991 is a mixture with more perovskite than brownmillerite. Therefore, the phase transition effect is not as prominent as when the materials is at 600 or 700 °C.

For LSCF1991 desorption, higher oxygen concentration effluent was expected based on the rapid weight drop observed in TGA, which indicates more oxygen released per unit time from the sorbent. **Figure 2.9 (a)-(c)** present the fixed-bed desorption breakthrough curves in 500-800°C of LSCF1991, LSCF1964 and LSCF2864, respectively. The desorption capacities and desorption efficiencies calculated from the breakthrough curves are listed in **Table 2.2**. The desorption efficiency is defined as the ratio of desorption amount to sorption amount (both in fixed-bed) in a certain time interval. As shown by the data in **Table 2.2**, LSCF1991 does have higher desorption capacities than the other two materials. However, no enhanced oxygen desorption rate resulting from phase transition was observed during the process. The desorption breakthrough curves of the three materials all are in similar shape with a long tail.
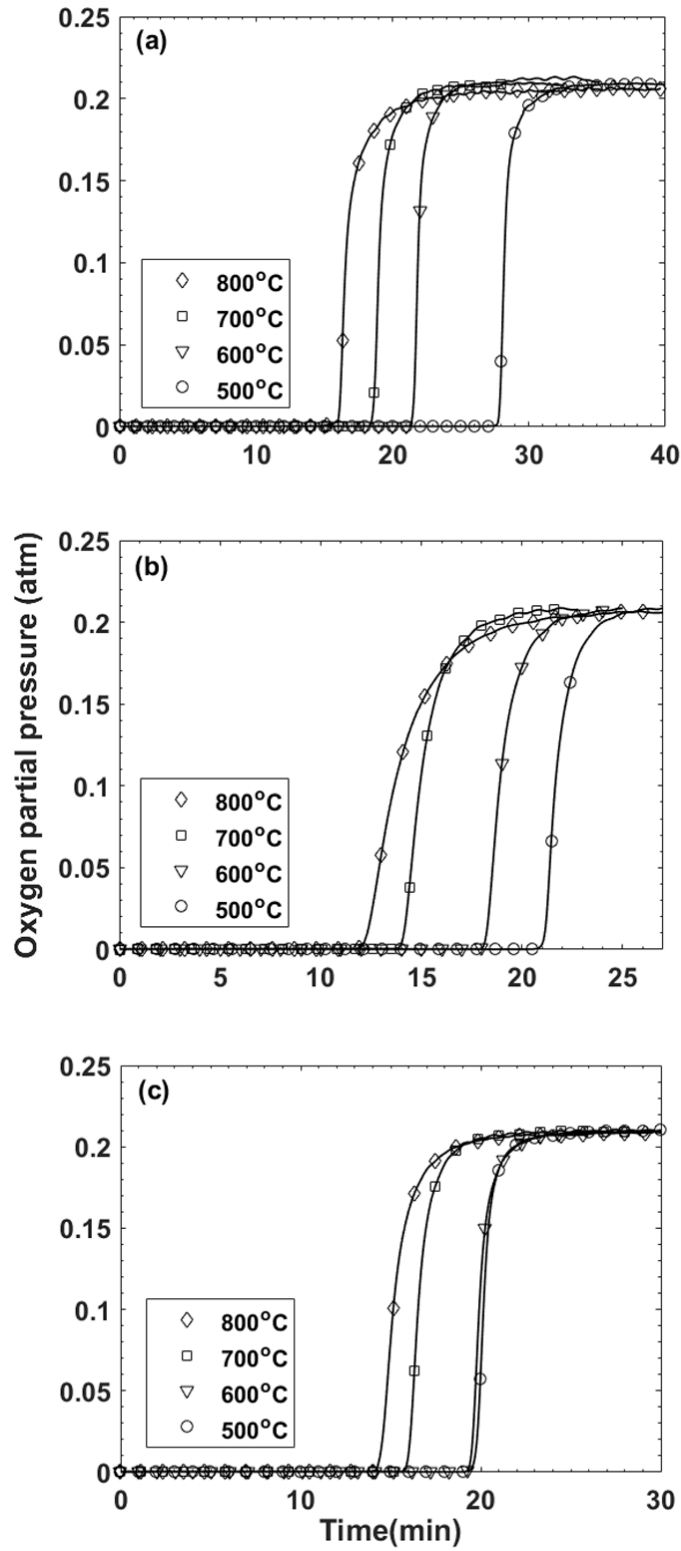
Figure 2.8. *Fixed-bed sorption breakthrough curves at 500-800°C of (a) LSCF1991 (b) LSCF1964 (c) LSCF2864.*
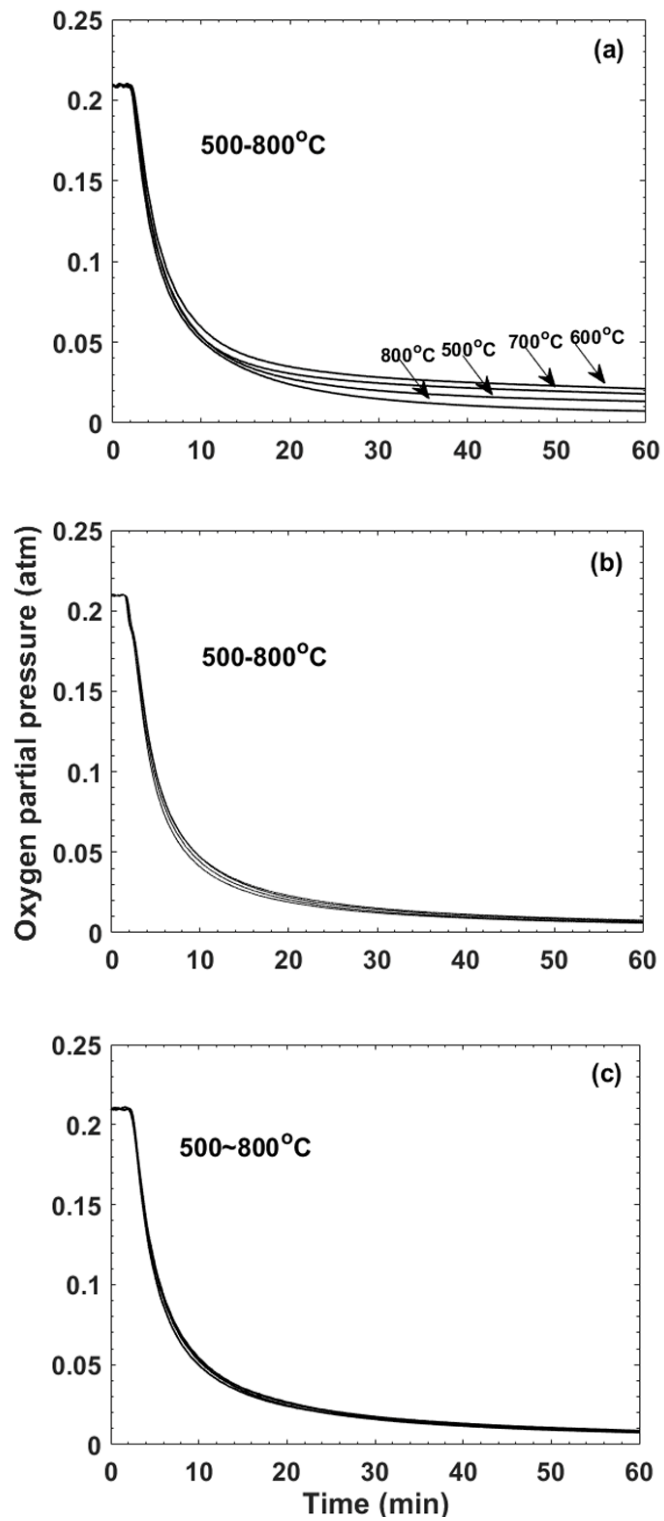
Figure 2.9*. Fixed-bed desorption breakthrough curves at 500 to 800°C of (a) LSCF1991 (b) LSCF1964 (c) LSCF2864.*

Table 2.2. *Fixed-bed desorption capacity data for LSCF perovskite oxides investigated in this work.*

	LSCF1991			LSCF1964			LSCF2864		
Temp. (°C)	Desorption capacity 30 min (mmol/g)	Desorption capacity 1 h (mmol/g)	Efficiency 1 h (%)	Desorption capacity 30 min (mmol/g)	Desorption capacity 1 h (mmol/g)	Efficiency 1 h (%)	Desorption capacity 30 min (mmol/g)	Desorption capacity 1 h (mmol/g)	Efficiency 1 h (%)
500	0.161	0.210	36.8	0.148	0.180	42.0	0.158	0.191	48.5
600	0.186	0.260	55.7	0.147	0.174	43.2	0.168	0.204	53.1
700	0.165	0.229	61.3	0.137	0.163	46.6	0.167	0.202	62.7
800	0.148	0.177	62.2	0.130	0.154	52.6	0.162	0.194	65.5

Table 2.3. *Estimated time to observe enhanced desorption rate in fixed-bed.*

Temp. (°C)	δ when when rate increases	δ when equilibrium	Oxygen desorption percentage when rate increase	Corresponding fixed-bed desorption amount (mmol)	Expected time to observe enhanced rate in fixed-bed desorption (min)
500	0.323	0.475	32%	0.182	41.5
600	0.345	0.478	27%	0.126	12.6
700	0.375	0.481	28%	0.105	10.2
800	0.421	0.483	50%	0.143	27.0

It can be observed that the points at which desorption rate is enhanced are close to the boundary between disordered phase region and two-phase region, as shown in **Figure 2.10** (Yin, Kniep and Lin, 2008). If phase transition occurs at the specific δ values of LSCF1991 in the fixed-bed process, then the phase transition should happen at the expected time listed in the last column of **Table 2.3.** However, as **Figure 2.9 (a)** presents, no obvious change in the desorption rate can be observed.
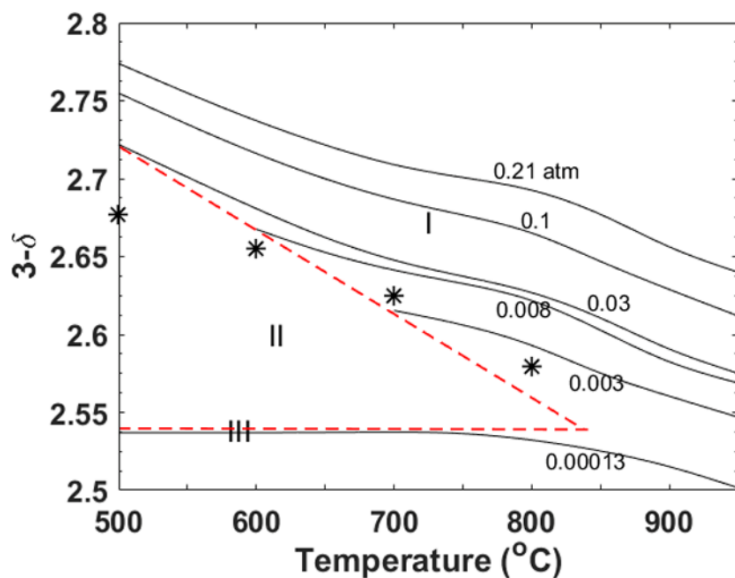
Figure 2.10. *Observed rate-enhanced points on LSCF1991 phase diagram (shown as *).*
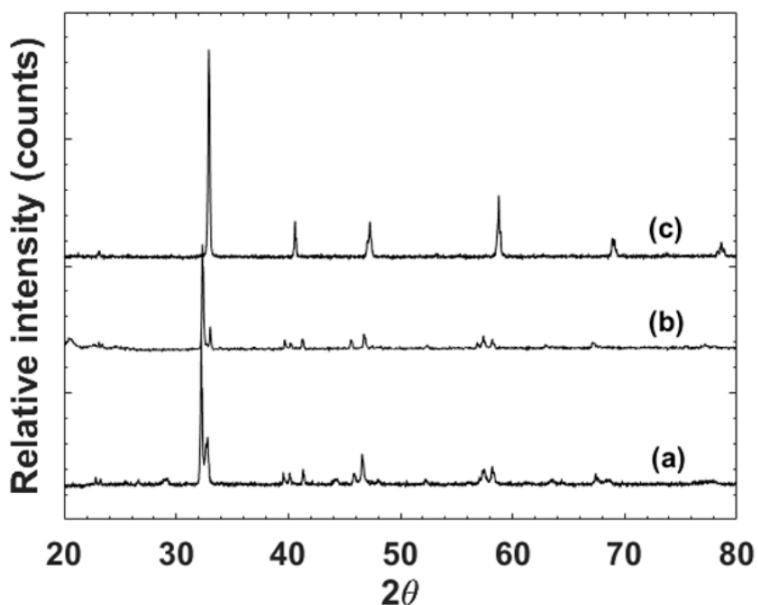
Figure 2.11. *XRD patterns of LSCF1991 of (a) sample quenched from fixed-bed at 600°C, (b) in-situ in vacuum at high temperature at 600°C (brownmillerite) and (c) fresh sample in air at room temperature (perovskite). The peak present in (b) at 2θ=20° was resulted from the polymer vacuum dome of high temperature set-up.*

Figure 2.11 shows the XRD pattern of the quenched LSCF1991 sample. Fresh sample XRD pattern at room temperature and in-situ high temperature XRD pattern in vacuum at 600°C are included as reference of perovskite and brownmillerite phase, respectively. As seen in **Figure 2.11,** although there are some low-intensity peaks which does not match the in-situ high temperature pattern, the quenched sample has evidently transformed into a phase close to brownmillerite. Since the sample was quenched in the fixed-bed after two hours of desorption, the sample may have not yet reached the equilibrium and developed into well-defined brownmillerite phase. Therefore the peaks present at $2\theta=29.1°$ and $44.3°$, which are absent at the high temperature pattern, may result from lower crystallinity of the quenched sample. In addition, it is noteworthy that the oxygen partial pressure in the high-temperature XRD vacuum chamber is much lower than in the fixed-bed at the moment when the sample was quenched. The XRD results suggest that even enhanced desorption rate was not observed during the fixed-bed oxygen desorption, the sample in the fixed-bed still went through the phase transition at the end.

Table 2.4. Comparison in experiment conditions and oxygen concentration in purge.

Experiment set-up	Sorbent amount	Purge flow rate	Initial oxygen desorption rate per unit mass (at 600°C)	Estimated P_{O2} in purge
TGA	20 mg	100 ml/min	5.309×10^{-5} mol O_2/min·g sorbent	3.595×10^{-4} atm
Fixed-bed	2 g	5 ml/min	2.335×10^{-5} mol O_2/min·g sorbent	0.193 atm

The reason for the oxygen vacancy disorder-order transition occurs during oxygen desorption in the TGA but not in the fixed-bed process can be explained by the phase diagram shown in **Figure 2.1**. In TGA experiments during the entire oxygen desorption, the oxygen partial pressure of the purge gas is always at low pressure (down to 10^{-4} atm) due to the large flow rate as compared to the LSCF sample amount. In contrast, the oxygen partial pressure surrounding the LSCF sample in the fixed-bed is much higher due to large amount of LSCF sample as compared to the gas flow rate. A simple semi-quantitative comparison of the two experiments is presented in **Table 2.4**. The initial oxygen desorption rate (defined as the rate from the start to 95% weight reduction) at 600°C calculated from the TGA data is 5.309×10^{-5} mol O_2/min·g sorbent. Under such operation condition the estimated P_{O2} in the purge gas is 3.595×10^{-4} atm. On the other hand, the initial desorption rate of fixed-bed (calculated from desorption breakthrough curve, defined as the rate from the start to 95% weight reduction) is 1.572×10^{-5} mol O_2/min·g sorbent, which is 44.0% of the rate in TGA. The oxygen partial pressure surrounding the sorbents in the fixed-bed is as high as 0.193 atm, as estimated by time average of outlet concentration.

Figure 2.12 illustrate the oxygen partial pressures in the gas stream during oxygen desorption process in TGA and fixed-bed experiments. By referring to **Figure 2.10**, for LSCF1991 desorption at 600°C, the P_{O2} at which the disorder-order phase transition takes place is about 0.008 atm. In the TGA experiment, the oxygen partial pressure in the gas stream is below the equilibrium oxygen partial pressure for ordered phase (indicated as P_{TGA} in **Figure 2.12**). Thus during oxygen desorption oxygen vacancy disorder-order transition occurs in early stage leading to enhanced oxygen desorption rate. The oxygen partial pressure in the gas stream in the fixed-bed experiment in most time is above the

equilibrium oxygen partial of ordered phase, thus disorder-order transition does not occur until the late stage of the desorption step (100-120 min on which the oxygen partial pressure is below 0.008 atm). Therefore, the enhanced oxygen desorption rate was not observed during the oxygen desorption but the sample quenched down after the end of oxygen desorption is in the ordered brownmillerite structure.
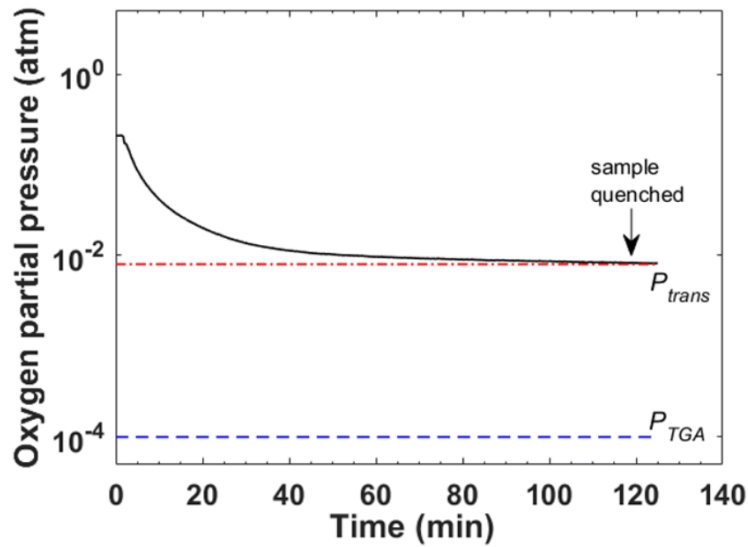
Figure 2.12. Comparison between oxygen partial pressure during LSCF1991 fixed-bed desorption at 600°C, oxygen partial pressure where phase transition takes place (P_{trans}) and oxygen partial pressure in TGA (P_{TGA}).

2.4. Conclusions

TGA measurements show that $La_{1-x}Sr_xCo_{1-y}Fe_yO_{3-\delta}$ (LSCF) with lower iron content (LSCF1991) possessing the unique disorder-order phase transition characteristics has significantly faster oxygen desorption rate than the other two LSCF materials without disorder-order phase transition. However, the disorder-order enhanced desorption rate was not observed in the fixed-bed desorption process. LSCF1991 sample quenched at 600°C after 2 h of desorption has changed to the ordered structure. The oxygen nonstoichiometry data show that the disorder-order phase transition is strongly related to the oxygen partial pressure surrounding the sorbents instead of material structure. During the TGA experiments the oxygen partial pressure in the sweep stream is below the equilibrium oxygen partial pressure for the disordered phase. In contrast, in the fixed-bed desorption process the perovskite sorbent is exposed to gas stream with oxygen partial pressure higher than the transition value until near the end of oxygen desorption breakthrough curve. This explains the differences in effect of the oxygen vacancy disorder-order transition in two oxygen desorption processes.

CHAPTER 3

MIXED-CONDUCTING CERAMIC-CARBONATE DUAL-PHASE
MEMBRANES: GAS PERMEATION AND COUNTER-PERMEATION

3.1.   Introduction

From the discussion in Chapter 1.2.1, we can see that a perovskite sorbent-based

PSA process poses greater potential than dense MIEC membranes for medium-quality

(~95%) oxygen production in a larger volume. However, the non-porous oxygen permeable

membrane still has its advantage in some applications. This technology is especially

attractive when it comes to oxidative reaction of hydrocarbons. Numerous investigations

have been carried out in the literature (Jiang *et al.*, 2008; Zhang *et al.*, 2008; Dong *et al.*,

2009; Wang *et al.*, 2009; Othman, Wu and Li, 2015), as discussed in Chapter 1.2.3. Also,

as introduced in **Figure 1.9**, the oxygen ion-conducting property of MIEC ceramics is not

only limited to oxygen separation. With molten carbonate infiltrated, the composite dual-

phase membrane becomes CO_2-permselective as the surface oxygen ions (O^{2-}) will react

with gaseous CO_2 and produce carbonate ions (CO_3^{2-}) via the following reaction:

$$CO_{2(g)} + O^{2-} \rightarrow CO_3^{2-} \qquad (3.A)$$
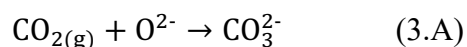
The carbonate ion will be driven by the CO_2 pressure gradient to the other side of the

membrane. On the other side of the membrane, which is exposed to a CO_2-lean atmosphere,

the reversed reaction of 3.A will take place and achieve CO_2 permeation.

From reaction 3.A we can see that oxygen ionic conductivity is essential to CO_2

permeation. Prior to the development of MIEC-carbonate dual-phase membranes, Chung

et al. (Chung *et al.*, 2005) first fabricated a metal-carbonate dense dual-phase membrane

with CO_2 permeance of 2.6×10^{-8} mol·m^{-2}·s^{-1}·Pa^{-1} and a CO_2/N_2 selectivity of 16 at 650 °C. Because the metal support does not have oxygen ion conductivity required for the surface reaction forming CO_3^{2-} ions to take place, this type of membrane demands the presence of oxygen along with CO_2 to achieve CO_2 permeation.

To eliminate the need for O_2, Anderson and Lin (Anderson and Lin, 2010) pioneered the research of ceramic-carbonate dual-phase membranes. The $La_{0.6}Sr_{0.4}Co_{0.8}Fe_{0.2}O_{3-\delta}$-carbonate (LSCF-MC) membrane reported by them exhibited promising CO_2 permeance up to 4.77×10^{-8} mol·m^{-2}·s^{-1}·Pa^{-1} at 900 °C and CO_2/N_2 selectivity of 225. Lin and coworkers (Ortiz-Landeros, Norton and Lin, 2013) also discovered that in most cases, the rate-limiting factor of CO_2 permeation is oxygen ionic conductivity of the ceramic phase. Therefore, increase oxygen ionic conductivity is critical to promoting CO_2 permeation of ceramic-carbonate dual-phase membranes. Their work inspired numerous following research projects later on, as mentioned in Chapter 1.2.2.

An interesting phenomenon was observed in the CO_2-O_2 co-permeation experiment conducted by Norton et al. (Norton, Ortiz-Landeros and Lin, 2014). When both CO_2 and O_2 are presented on the membrane surface, a significant increase in CO_2 permeation flux was measured (Norton, Ortiz-Landeros and Lin, 2014; Zhuang *et al.*, 2019). The results expanded the applicability of ceramic-carbonate dual-phase membranes and inspired the concept of CO_2-O_2 counter-permeation.

Based on the co-permeation phenomena, it is expected that the MIEC-MC membranes could also permeate CO_2 and O_2 in opposite directions. In such an operation, CO_2 and O_2 will be separated into the two sides of the membrane rather than presented on the same side as conducted in the previous research. The counter-permeation concept is

illustrated in **Figure 3.1**. As shown in the figure, CO_2 would react with the oxygen ion on the ceramic-carbonate interface and permeate through the carbonate phase. Meanwhile, O_2 permeation would occur via surface oxygen defect reaction. One of the potential applications of this type of membrane permeation is autothermal methane reforming (AMR) membrane reactors, which is illustrated in **Figure 3.2**. The AMR reactor can be described as reaction 3.B-3.D as follows:

$$CH_4 + H_2O \leftrightarrow CO + 3H_2O \qquad \Delta H^0_{298K} = 206 \text{ kJ/mol} \qquad (3.B)$$

$$CH_4 + 1/2O_2 \leftrightarrow CO + 2H_2 \qquad \Delta H^0_{298K} = \text{-35 kJ/mol} \qquad (3.C)$$

$$CO + H_2O \leftrightarrow CO_2 + H_2O \qquad \Delta H^0_{298K} = \text{-41 kJ/mol} \qquad (3.D)$$

As indicated above, reaction 3.B is highly endothermic, whereas reaction 3.C and 3.D are both exothermic. With appropriate control of reaction selectivity, the reaction can theoretically achieve heat balance and reduce the energy toll for the reaction (hence the autothermal naming). The oxygen required by the reaction can be provided by the membrane and save the cost for an extra air separation unit. Also, the oxygen supplied by the membrane is in ionic form instead of the direct mixing of gaseous oxygen. This can possibly better handle the problem of heat accumulation in the front end of a conventional fixed-bed reactor when performing AMR, which has been reported in the literature (Li et al., 2004; Simeone, Salemme and Allouis, 2008). Moreover, the in situ CO_2-removal can shift the reaction towards the product side and enhance hydrogen production. Besides AMR, several potential applications such as the partial oxidative reaction of hydrocarbons in a membrane reactor can also be explored based on this unique CO_2 and O_2 counter-permeation properties of the MIEC-MC membranes.
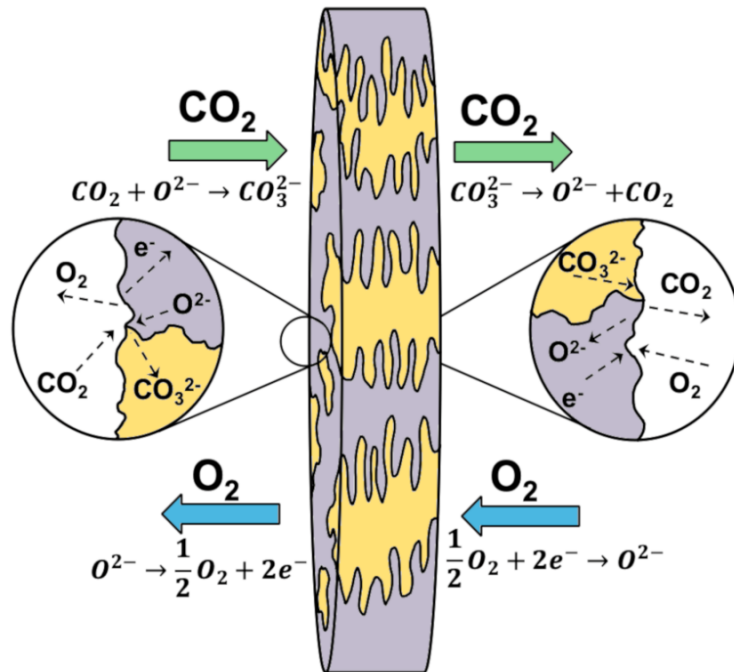
Figure 3.1. *Illustration of CO_2/O_2 counter-permeation concept introduced in this work.*
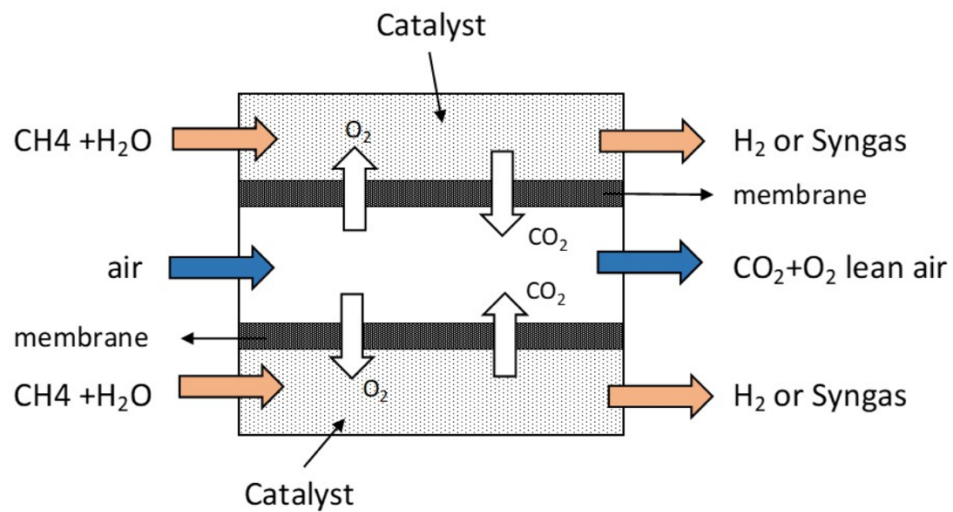
Figure 3.2. *Schematic of an autothermal methane reforming (AMR) reactor equipped with CO_2-O_2 counter-permeable membrane.*

However, as mentioned in Chapter 1.2.1, some of the perovskite materials with high oxygen permeability lack stability in CO_2-rich environment due to containing highly basic metal ions, i.e. Sr and Ba. On the other hand, most fluorite oxides have low electrical conductivity despite having decent oxygen ionic conductivity. These materials are very likely to have failure or poor performance if used for CO_2-O_2 counter-permeation. Therefore, the materials selection of the membrane is essential for this work. Based on the promising results from Partovi et al. (Partovi *et al.*, 2015) and Jiang et al. (Jiang *et al.*, 2016), two perovskite materials, $Pr_{0.6}Sr_{0.4}Co_{0.2}Fe_{0.8}$ (PSCF) and $SrFe_{0.9}Ta_{0.1}O_{3-\delta}$ (SFT), were selected as the membrane support for this study. However, in the literature, these membranes were only tested for O_2 separation in CO_2-rich environment. The performance of CO_2-O_2 counter-permeation remains unknown. The objective of this research is to investigate (a) the applicability of the counter-permeation concept, (b) the interactions between CO_2 and O_2 permeation and (c) the effect of geometric factor of the support on permeation. As the first ever counter-permeation study conducted, it is expected the result of this research will reveal more potential applications of MIEC-carbonate membranes.

3.2. Experimental

3.2.1. Preparation of Ceramic Powders and Membranes

$Pr_{0.6}Sr_{0.4}Co_{0.2}Fe_{0.8}O_{3-\delta}$ (PSCF) ceramic powder was synthesized via the liquid citric method. Stoichiometric amounts of $Pr(NO_3)_3 \cdot 6H2O$ (Alfa Aesar, 99.9%), $Sr(NO_3)_2$ (Alfa Aesar, 99.5%), $Co(NO_3)_3 \cdot 6H_2O$ (Alfa Aesar, 98-102%) and $Fe(NO_3)_3 \cdot 9H_2O$ (Alfa Aesar, 98-101%) were dissolved in deionized water at 100 °C with agitation. The water was gradually evaporated and a gel-like composite was formed. The temperature was increased to 400 °C to induce self-ignition and remove the carbon content in the mixture. The composite was then calcined at 850 °C for 8 h to form a perovskite structure. $SrFe_{0.9}Ta_{0.1}O_{3-\delta}$ (SFT) powder was synthesized via the solid-state reaction method. Stoichiometric amounts of $SrCO_3$ (Alfa Aesar, 99.5%), Fe_2O_3 (Alfa Aesar, 99.495%) and Ta_2O_5 (Alfa Aesar, 99.99%) powder were mixed by ball-milling in ethanol for 24 h. After drying, the powder was calcined at 1250 °C for 20 h.

Disc PSCF and SFT supports were made by hydraulic pressing (Carver 3853-0) at 140 MPa for 5 min. The porous supports were obtained after sintering the green bodies at 1200 °C for 10 h. The sintering process was followed by molten carbonate infiltration. A $Li_2CO_3/Na_2CO_3/K_2CO_3$ (Alfa Aesar 99/99.5/99%) mixture was prepared in 42.5/32.5/25 molar percent and melted at 550 °C in an alumina crucible. Porous supports were brought to contact the molten carbonate liquid surface, and the carbonate was absorbed into the pores due to the capillary effect. The as-synthesized membranes were then ground and polished to about 1.5 mm in thickness with a permeation area of about 1.78 cm^2.

3.2.2. Membrane Characterization

Total conductivity measurements were made on porous and dense PSCF and SFT samples by the four-point method (Wei and Lin, 2008). A silver conducting ink (Alfa Aesar) was used to hold the wires in place and minimize the effects of contact resistance between the wires and membrane. When performing the measurement, current was supplied in the outermost wires, and the voltage was measured across the inner wires. A Keithley 2400 source meter was used to supply a current ranging from 10-100 mA. A Keithley Integra Series 2700 multimeter was used to measure the voltage. The total conductivity (σ_{total}) of the material was calculated using Eq. 3.1 where conductivity is related to the bar's cross-sectional area (A), the current in the outside wires (I), the voltage across the inner wires (V), and the distance between the inner wires (L). On average, the dense sample had an inner wire distance of 4.7 mm and a cross-sectional area of 13.2 mm^2.

$$\sigma_{total} = \frac{IL}{VA} \qquad (3.1)$$

Pore structures of the perovskite supports were characterized by steady-state helium permeation. The as-synthesized disc supports were placed in a metal housing and sealed with rubber O-rings. Steady-state helium flow rates with various pressure differences across the membrane were measured by a bubble flow meter. The measured permeance was then plotted as a function of average pressure of the two sides of the membrane (P_{avg}) and the dusty-gas model (presented as follows) was used for curve fitting (Malinauskas and Mason, 1983). The porosity of the porous supports was measured via Archimedes method with liquid nitrogen, for which the detail description can be found elsewhere (Harry and Johnson, 2004). The porosity to tortuosity ratio (ϕ_p) and average pore radius (r_p) can

61

be calculated from the slope (β) and the intercept (α) of the data fitting.

$$\frac{F}{L} = \alpha + \beta P_{avg} \qquad (3.2)$$

$$\alpha = 1.06 \left(\frac{\varepsilon}{\tau}\right)_p \frac{r_p}{L\sqrt{RTM_w}} \qquad (3.3)$$

$$\beta = 0.125 \left(\frac{\varepsilon}{\tau}\right)_p \frac{r_p^2}{L\mu RT} \qquad (3.4)$$

where ε and τ are the porosity and the tortuosity of the support, respectively, or $\phi_p = \left(\frac{\varepsilon}{\tau}\right)_p$,

referred to as geometry factor for the pores; L is membrane thickness, μ is the viscosity of

test gas (helium in this case), R is gas constant, M_w is the molecular weight of helium.

The phase structures of the membranes were examined by X-ray diffraction (XRD, PANalytical X'Pert Pro, CuKα1 radiation) before and after infiltration. The International Center for Diffraction Data (ICDD) database was used for identifying phase structures. Scanning electron microscopy (SEM, Amray 1910) imaging was used to observe morphology change of the both PSCF-MC and SFT-MC following the membrane synthesis.
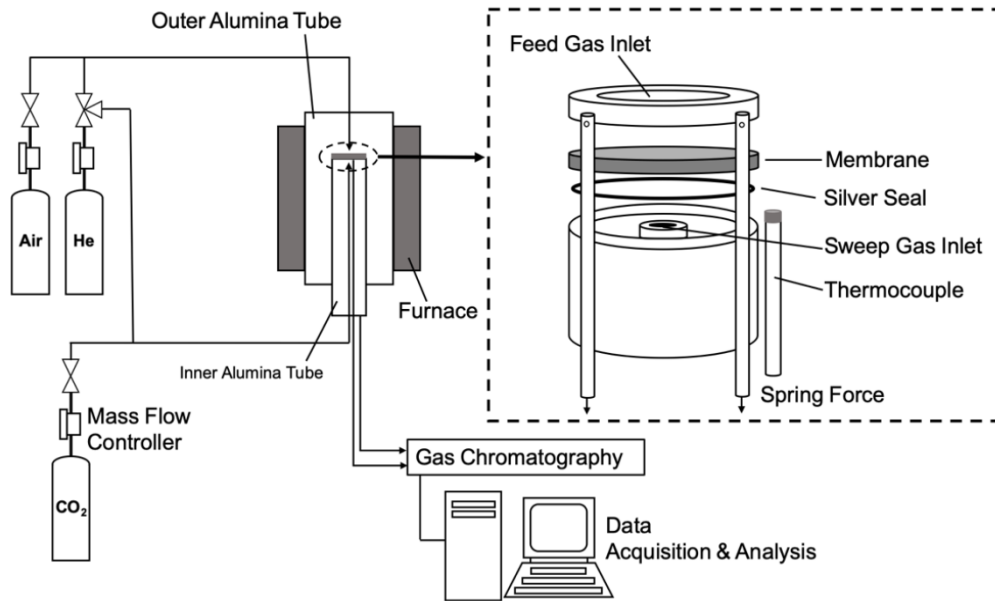
Figure 3.3. Schematic of the high-temperature gas permeation set-up used in this work.

3.2.3. High-Temperature Permeation and Counter-Permeation Measurements

Gas permeation and reaction experiments were performed on a Probostat high-temperature gas permeation system (Probostat, Norwegian Electro Ceramics AS) integrated with a built-in-house gas supply and furnace set-up, as illustrated in **Figure 3.3**. The dual-phase membranes were sealed by a silver ring in the inner tube of the Probostat. Gas-tight sealing was achieved by heating the assembly at 1 °C/min to 950 °C in air to soften the silver ring. As the silver ring softens, the springs and an aluminum spacer in the assembly press down the membrane forming a gas-tight seal. Before performing gas permeation, nitrogen was used to identify potential leaks in the membrane or sealing. All the experiments were performed with a gas-tight set-up. Gas compositions were analyzed by an Agilent 7890A gas chromatography (GC) with a TCD detector, with a HayeSep DB 100/120 column. For O_2 single-gas permeation, a synthetic air (Praxair, breathing grade) was used as feed, while for CO_2 single-gas permeation, 50% CO_2/50% He (Praxair, industrial grade) was used as feed. For both experiments, the feed was controlled at 50 ml/min by mass flow controllers (MKS, model 1179), and 100 ml/min of helium was used as sweep. Both sides were controlled at 1 atm. For CO_2/O_2 counter-permeation, 50% CO_2/50% He was used on one side and synthetic air was used on the other side of the membrane. Both gas streams were set at a total flow rate of 50 ml/min and both sides were kept at 1 atm.

3.3. Results and Discussions

3.3.1. Membrane Microstructure and Conductivity

Porous PSCF and SFT membrane discs were examined by XRD and SEM following the synthesis. As shown in **Figure 3.4**, the XRD patterns indicate that both materials are in the typical perovskite structure, which is consistent with reported data in the literature (Partovi *et al.*, 2015; Zhu *et al.*, 2015). Due to different synthesis methods for the powder, the two membranes exhibit different microstructure. As shown in **Figure 3.5**, the PSCF support has a smaller grain size and better connection between particles, whereas the SFT support appears to have larger and loosely connected grains. The difference between the support microstructure accordingly leads to different pore structures. **Figure 3.6** shows helium permeance for these two membranes versus different average trans-membrane pressure. The data can be well correlated by Eq. 2. The coefficients for the regression, α, and β, and the average pore radius and porosity to tortuosity ratio ($\phi_p = (\varepsilon/\tau)_p$), calculated by Eq. 3 and 4, together with the porosity measured for the PSCF and SFT supports, are given in Table 3.1. As shown, PSCF and SFT supports have similar porosity, tortuosity and porosity/tortuosity ratio (ϕ_p). However, the average pore size of SFT support is about twice that of PSCF. This is consistent with the microstructures observed under SEM **(Figure 3.4)**.
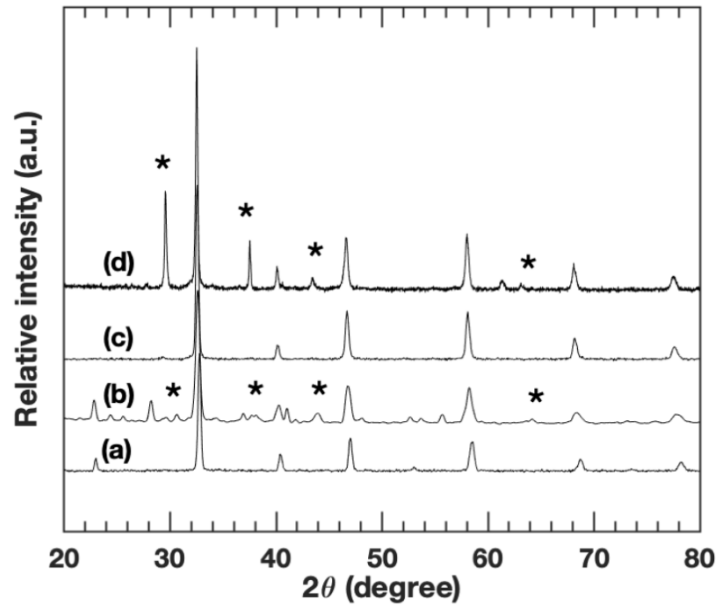
Figure 3.4. *XRD diffraction patterns of fresh (a) PSCF porous support (b) PSCF-MC membrane (c) SFT porous support and (d) SFT-MC membrane. The * marks represent the peak pattern of the molten carbonate mixture.*
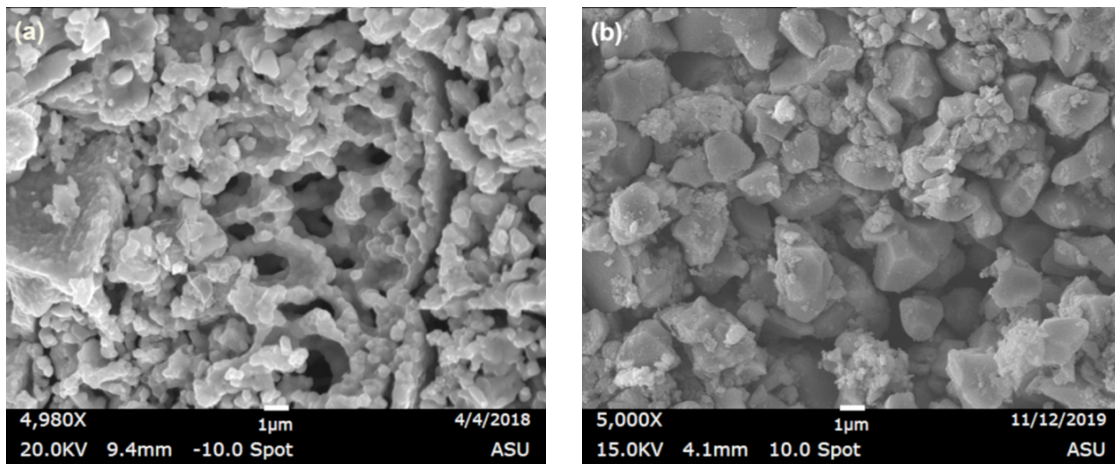
Figure 3.5. *SEM images of (a) PSCF porous support and (b) SFT porous support.*
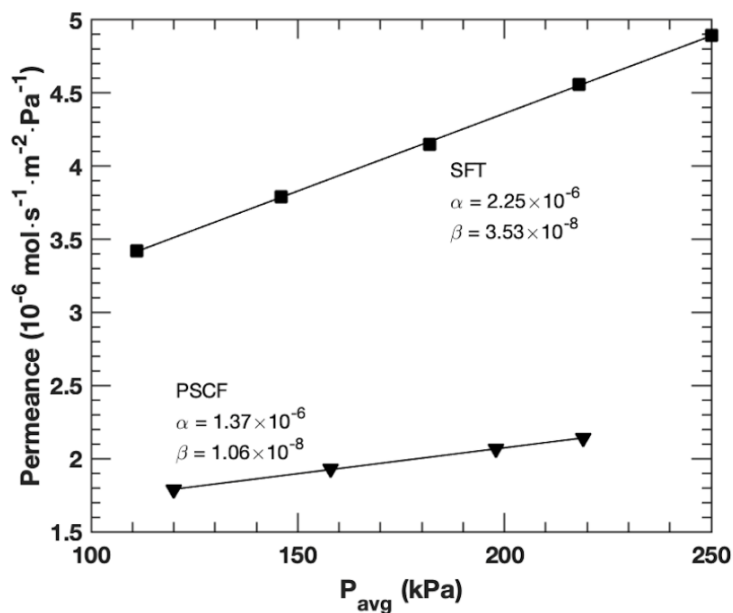
Figure 3.6*. Steady-state helium permeation data of PSCF and SFT porous supports.*

Table 3.1*. Pore and solid structure data for porous PSCF and SFT supports.*

Material	α (mol m^2 s^{-1} Pa^{-1})	β (mol m^2 s^{-1} Pa^{-2})	Porosity (ε)	Avg. pore radius (nm)	Geometric factor for pores ϕ_P (=ε/τ)	Pore tortuosity (τ)	Geometric factor for solid (ϕ_s)
PSCF support	1.37×10^{-6}	1.06×10^{-6}	0.30	330	0.027	11.0	0.68
SFT support	2.25×10^{-6}	3.53×10^{-6}	0.26	654	0.019	13.6	0.39

Figure 3.7 shows total conductivity (or electronic conductivity) at different temperatures for dense and porous PSCF and SFT samples. Compared with literature, PSCF exhibits similar conductivity with Sr-Co-Fe system perovskite ceramics (Zeng *et al.*, 2007; Anderson and Lin, 2010), while SFT has lower conductivity at the whole tested temperature range. In general, the conductivity for a porous solid can be correlated to the dense one by:

$$\sigma_{porous} = \phi_s \, \sigma_{dense} \qquad\qquad (3.5)$$

Thus, the ratio of the conductivity for porous discs to that of the dense ones gives a geometry factor for solid as ϕ_S, which has a physical meaning of the ratio of the relative cross-sectional area for solid phase to the solid tortuosity [$\phi_S = (\varepsilon/\tau)_s$] for electrons (or oxygen ion) transport in the solid phase of the porous support. The values for ϕ_S is about 0.68 for PSCF porous support and 0.38 for SFT porous support. The two ratios are about constant over the temperature range measured.
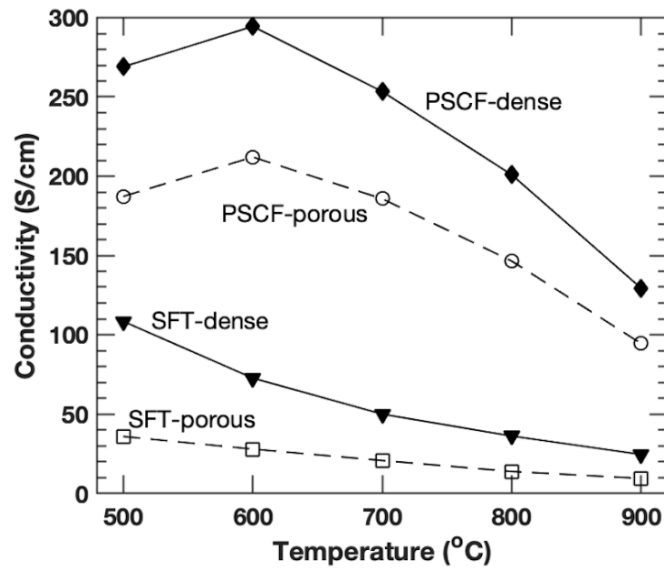
Figure 3.7. *Comparison of total conductivity data of dense perovskite membranes and porous perovskite supports at 500-900 °C.*

The backscattered electron images present the contrast between the infiltrated carbonate (dark parts) and perovskite support (light parts), as shown in **Figure 3.8**. The exposure of both phases provides permeation pathways for CO_2 and O_2, which is crucial to the CO_2-O_2 counter-permeation. Furthermore, the gases will only permeate through the membrane via surface reaction and ionic conduction due to its dense structure after carbonate infiltration.
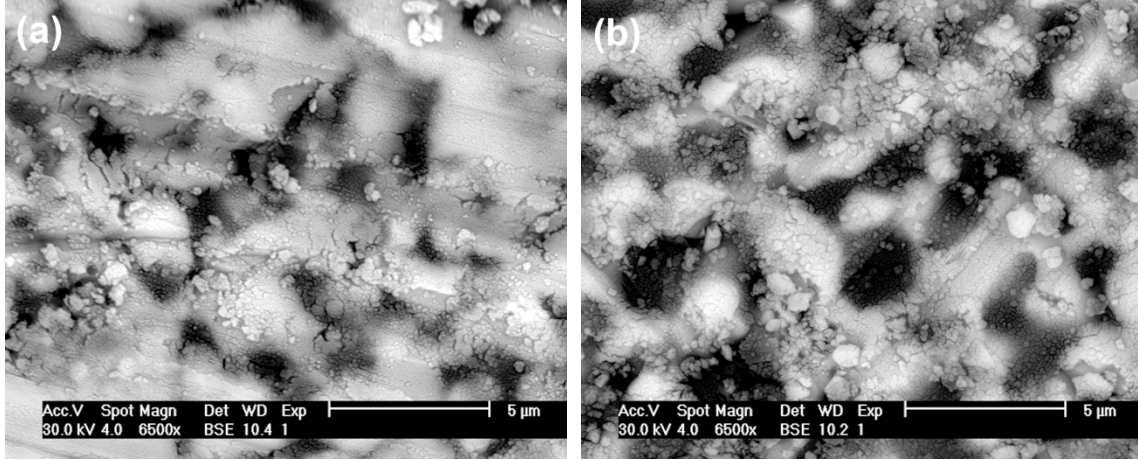
Figure 3.8. *SEM backscattered electron image of (a) surface of PSCF-MC (b) surface of SFT-MC*

3.3.2. Oxygen and Carbon Dioxide Single-Gas Permeation

Oxygen permeation experiments were carried out with synthetic air feed and helium sweep for both PSCF-MC and SFT-MC dual-phase membranes. The oxygen transports through the perovskite phase via oxygen ion, balanced by the electron transport, as illustrated in **Figure 3.9 (a)**. The amount of oxygen transport through the carbonate phase is negligible. In this case, the oxygen permeation flux can be correlated to the electronic and oxygen ionic-conductivity, σ_e and σ_i and the geometric factor ϕ_s of the perovskite phase by Eq. 6 (Bouwmeester *et al.*, 1992; Sunarso *et al.*, 2008):

$$J_{O_2} = \left[\frac{1}{16F^2}\right]\left[\frac{\phi_s\sigma_e\sigma_i}{\sigma_e+\sigma_i}\right]\left(\frac{d\mu_{O_2}}{dz}\right) \qquad (3.6)$$

where F is Faraday's constant and μ_{O2} is oxygen chemical potential. Considering $\sigma_e \gg \sigma_i$ with the geometric factor for the perovskite phase in the dual-phase membrane, and assuming oxygen partial pressure is independent of oxygen ionic conductivity, Eq. 3.6 can be simplified to (Qiu *et al.*, 1995):

$$J_{O_2} = [\phi_s \sigma_i] \left[\frac{RT}{16F^2L}\right] \ln\left(\frac{P'_{O_2}}{P''_{O_2}}\right) \qquad (3.7)$$

where P'_{O_2} and P''_{O_2} are the oxygen partial pressure in the feed and sweep side, respectively, R is gas constant, T is temperature and L is the membrane thickness.

(a) O_2 permeation
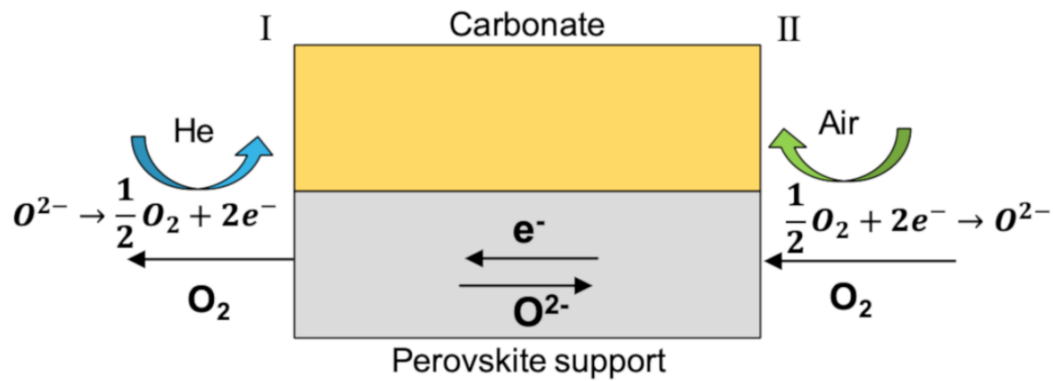
(b) CO_2 permeation
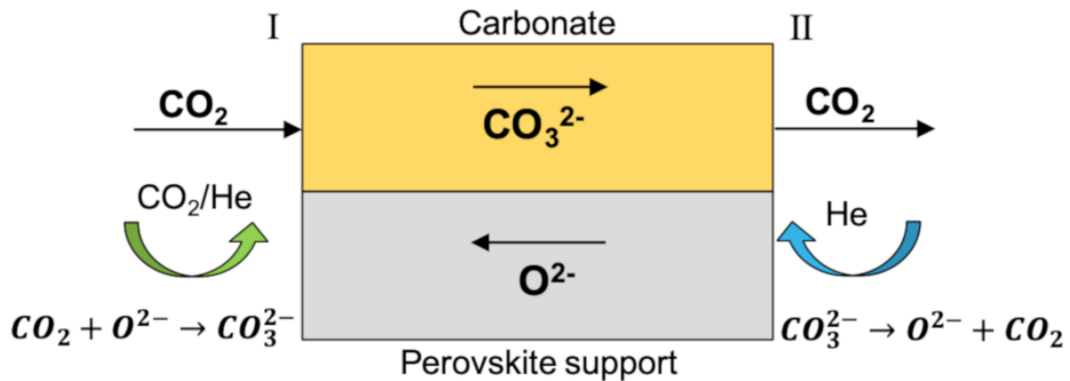
Figure 3.9. *Schematic illustration of (a) oxygen permeation and (b) carbon dioxide permeation through perovskite-carbonate dual-phase membranes.*
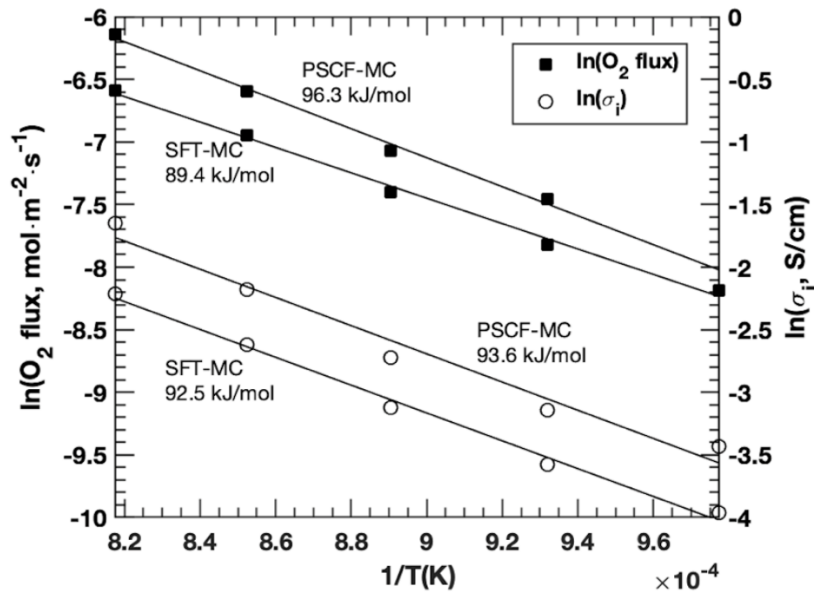
Figure 3.10. *Arrhenius plot of oxygen ionic O_2 permeation flux and σ_i of PSCF-MC and SFT-MC at 750-950 °C. Feed: 50 ml/min synthetic air feed. Sweep: 100 ml/min He sweep.*

The oxygen ionic conductivities for the two perovskite materials can be calculated with oxygen permeation flux data using Eq. 3.7. The temperature dependence of O_2 permeation flux can be correlated by the Arrhenius equation, as shown in **Figure 3.10**. The temperature dependence of permeation flux is quite different from the temperature dependence of the total (electronic conductivity) shown in **Figure 3.7**. The ionic conductivities measured for both materials are about 2-3 orders of magnitude lower than their electronic conductivities. Moreover, the O_2 permeation activation energies for both membranes are very close to their respective activation energies of σ_i. This clearly indicates the rate-limiting factor for O_2 permeation is the O^{2-} ionic conduction in the perovskite phase instead of the electronic conduction. The activation energy for oxygen ionic conductivity calculated in this work generally agreed well with literature (**Table 3.3**), which indicates the σ_i versus temperature relationships are similar in many perovskite ceramics. For SFT,

the activation energy is somewhat larger than the reported values, which could be a result of material crystallinity or measurement error.

Table 3.2. *The apparent activation energy for O_2 or CO_2 permeation under different conditions.*

	PSCF-MC		SFT-MC	
	O_2 permeation E_a	CO_2 permeation E_a	O_2 permeation E_a	CO_2 permeation E_a
Without counter-permeation	96.3	61.9	89.4	54.8
With counter-permeaton	99.6	66.4	90.8	54.7

Unit for activation energy: kJ/mol

Table 3.3. *Comparison of O_2 permeation activation energy of perovskite materials.*

Membrane Material	Thickness (mm)	O_2 permeation E_a (kJ/mol)	Reference
$La_{0.8}Sr_{0.2}Co_{0.6}Fe_{0.4}O_{3-\delta}$	1.4	81.9-127.8	(Qi, Lin and Swartz, 2000)
$Ba_{0.5}Sr_{0.5}Co_{0.8}Fe_{0.2}O_{3-\delta}$	0.07	51.7-86.4	(Baumann *et al.*, 2011)
$Pr_{0.6}Sr_{0.4}Co_{0.2}Fe_{0.8}O_{3-\delta}$	0.6	~98	(Partovi *et al.*, 2015)
$Pr_{0.6}Sr_{0.4}Co_{0.2}Fe_{0.8}O_{3-\delta}$	1.5	96.3	This work
$SrFe_{0.8}Sb_{0.2}O_{3-\delta}$	1	67	(Zhu *et al.*, 2015)
$SrFe_{0.9}Ta_{0.1}O_{3-\delta}$	1	64	(Zhu *et al.*, 2015)
$SrFe_{0.9}Ta_{0.1}O_{3-\delta}$	1.5	89.4	This work

CO$_2$ permeation fluxes at different temperatures for these two membranes were measured with 50:50 CO$_2$/He feed and He sweep. The permeation flux data are given in **Figure 3.11**. As shown, the CO$_2$ permeation flux increases exponentially with temperature, similar to the temperature dependence of oxygen permeation. The Arrhenius plot of CO$_2$ permeates flux shown in **Figure 3.11** gives apparent activation energy for CO$_2$ permeation of 54-66 kJ/mol, which are much smaller than that for oxygen permeation. CO$_2$ permeation through the dual-phase membrane occurs via oxygen ionic conductivity in the perovskite phase and carbonate ion conduction in the molten-carbonate phase, as illustrated in **Figure 3.9 (b).** Ortiz et al. (Ortiz-Landeros, Norton and Lin, 2013) derived the following equation for CO$_2$ permeation flux for perovskite-MC dual-phase membranes:

$$J_{CO_2} = \frac{kRT}{4F^2L} \ln \left(\frac{P'_{CO_2}}{P''_{CO_2}} \right) \qquad (3.8)$$

where k is referred to as total effective conductance as:

$$k = \frac{\phi_p \sigma_c \phi_s \sigma_i}{\phi_p \sigma_c + \phi_s \sigma_i} \qquad (3.9)$$

where P'$_{CO2}$ and P''$_{CO2}$ are the CO$_2$ partial pressures in the feed and sweep side, respectively, and σ_c is the carbonate conductivity of the carbonate phase and σ_i is the oxygen ionic conductivity of the ceramic phase. Arrhenius plot of the total conductance k, calculated from the CO$_2$ permeation data using Eq. 8, is also presented in **Figure 3.11**. The activation energies of k are very close to that of CO$_2$ permeation given in **Table 3.2**, which are also lower than that for oxygen ionic conductivity in the perovskite phase.

With the oxygen ionic conductivity data for PSCF and SFT shown in **Figure 3.10**, and carbonate ionic conductivity data for the molten carbonate from the literature (Li, Xiao and Huang, 2011), the effective carbonate and oxygen ionic conductivity, $\phi_p \sigma_c$ and $\phi_s \sigma_i$

versus different temperatures are given in **Figure 3.12**. Though σ_c is much larger than σ_i, the effective carbonate ionic conductivity in the carbonate phase is not negligible when compared with the effective oxygen ionic conductivity in the perovskite phase. Thus, the activation energy for CO_2 permeation (or total conductance) should fall in the range between the activation energy for carbonate ionic transport (about 30 kJ/mol (Li, Xiao and Huang, 2011)) and oxygen ionic transport in the perovskite phase (about 90 kJ/mol, see **Table 3.3**).
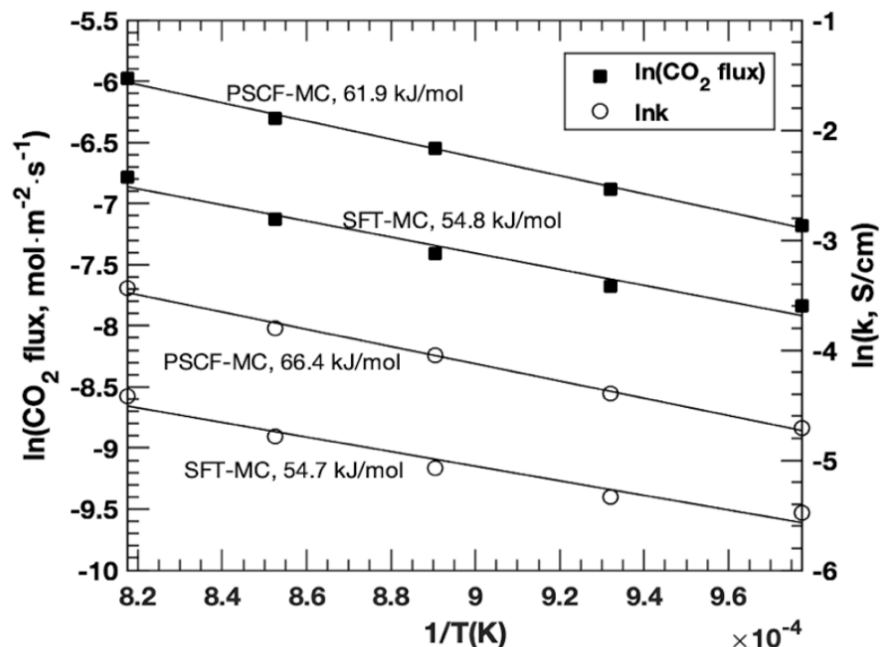
Figure 3.11. *Arrhenius plot of CO_2 permeation flux and total conductance of PSCF-MC and SFT-MC at 750-950 °C. Feed: 50 ml/min 50%/50% CO_2/He. Sweep: 100 ml/min He.*
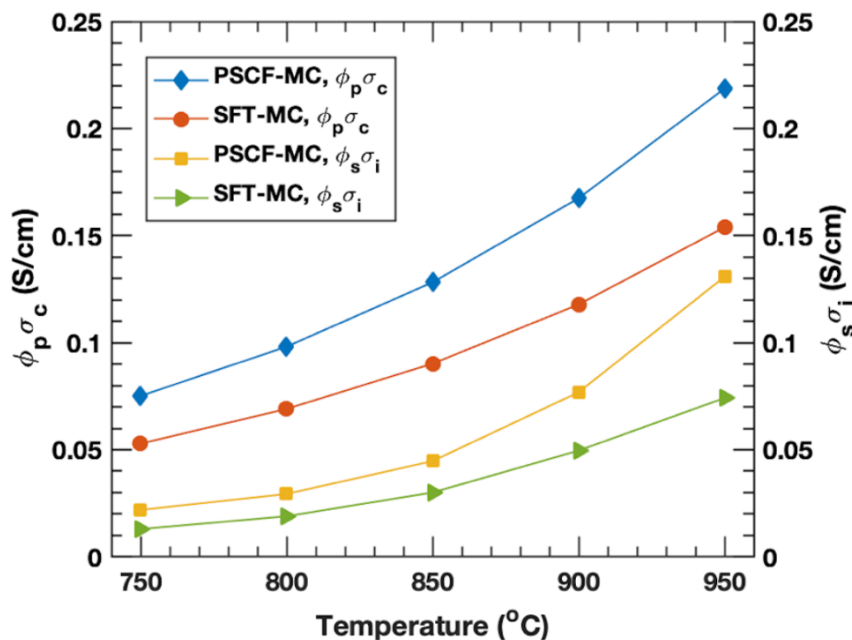
Figure 3.12. *Comparison of effective carbonate and oxygen ionic conductivity $\phi_p\sigma_c$ and $\phi_s\sigma_i$ for membranes.*

3.3.3. Carbon Dioxide/Oxygen Counter-Permeation

CO_2/O_2 counter-permeation experiments were conducted with CO_2/He feed to one side of the membrane (referred to CO_2 side, or membrane surface I) and synthetic air feed to the other side of the membrane (air side, or membrane surface II), as shown in **Figure 3.13.** These surfaces of the membranes are defined in the same way as single CO_2 or O_2 permeation shown in **Figure 3.9**. In all cases, the permeation flux was measured from the permeate stream (i.e., stream from surface II for CO_2 permeation flux, and that from surface I for O_2 permeation). During counter-permeation experiments, both O_2 and CO_2 were detected respectively in the permeate stream from surface I and surface II, confirming counter-permeation of O_2 and CO_2 in the perovskite-MC membranes. This suggests the transport of three charged species (O^{2-}, CO_3^{2-}, e^-) in the membrane during the counter-permeation experiments was achieved, as illustrated in **Figure 3.13**.
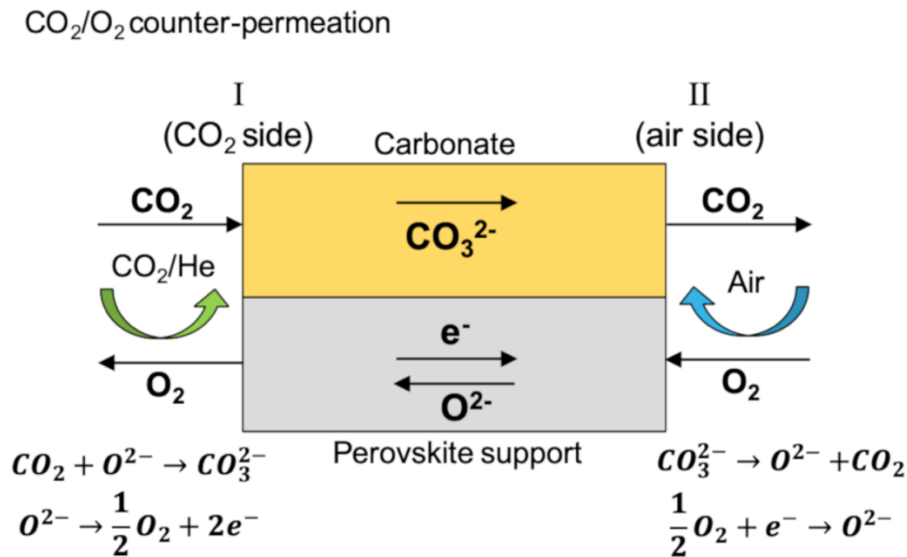
Figure 3.13. *Schematic illustration of transport of various charged species for the perovskite-carbonate dual-phase membrane under CO_2/O_2 counter-permeation experiments.*

Figure 3.14 compares O_2 permeation fluxes (measured from surface I) under CO_2 counter-permeation conditions with those of pure O_2 permeation for PSCF-MC and SFT-MC membranes. The O_2 permeation flux with CO_2 counter-permeation is lower than without CO_2 counter-permeation for both membranes while still follows the same temperature dependence. The apparent activation energy calculated from Arrhenius plots of the O_2 permeation data for both cases are essentially the same, as listed in **Table 3.2**. This suggests that the oxygen permeation in both cases follows the same mechanism, as described by Eq. 3.7.

Specific O_2 permeation flux without and with CO_2 counter-permeation at a given temperature (i.e., 850 °C) are tabulated in **Table 3.4** to facilitate discussion on O_2 permeation through the perovskite-MC dual-phase membranes. Without CO_2 counter-permeation, the O_2 permeation flux for the membrane is the same as the oxygen ion flux (divided by 2) through the bulk of the membrane. With CO_2 counter-permeation, the O_2 permeation through surface I, J_{O2}, is lower than that without CO_2 counter-permeation. However, with CO_2 counter-permeation, some of the oxygen ions transporting through the membrane are consumed on the membrane surface I for the formation of carbonate ion for CO_2 permeation. Thus, the total oxygen ionic flux (expressed in molecular O_2 flux) includes both for O_2 and CO_2 fluxes measured as:

$$J_{O2(total)} = J_{O2} + \tfrac{1}{2} J_{CO2} \qquad (3.10)$$
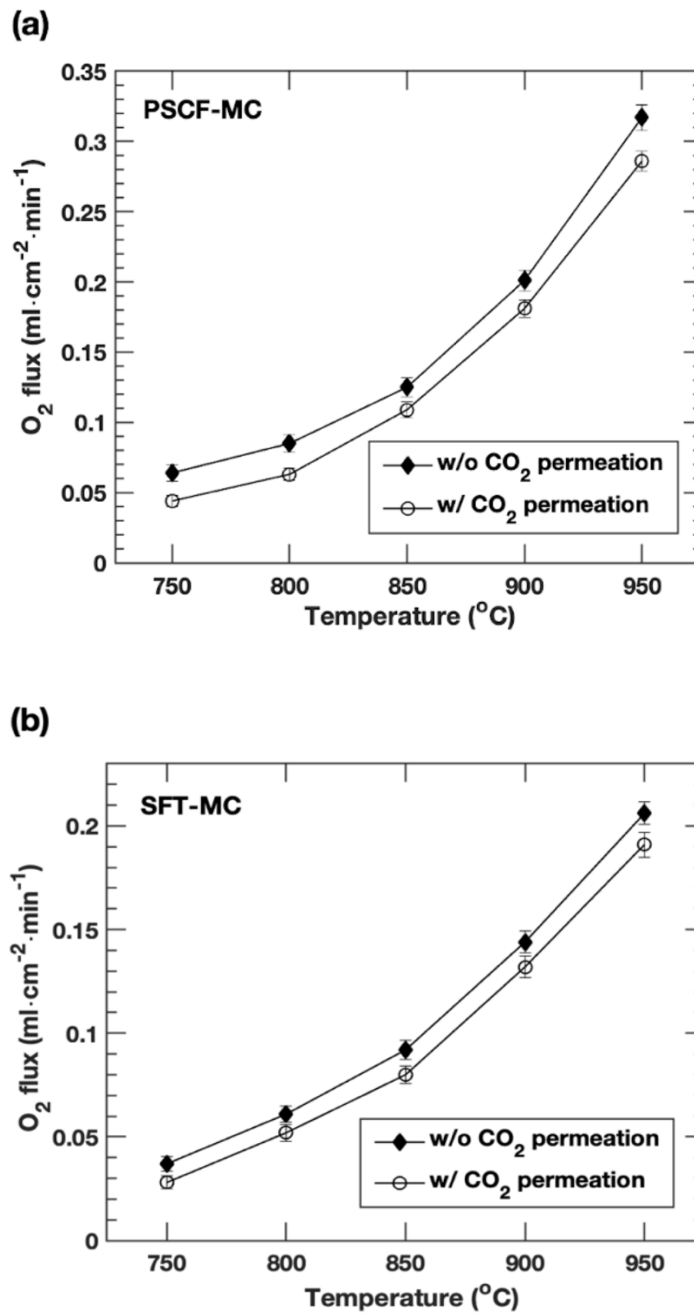
Figure 3.14. *O₂ permeation flux of (a) PSCF-MC (b) SFT-MC membrane in both single component permeation and counter-permeation set-up at 750-950 °C. Air side: synthetic air 100 ml/min. CO₂ side: CO₂ 50 ml/min, He 50 ml/min.*

As given in **Table 3.4**, with known CO_2 counter-permeation flux, the J_{O2} measured is 20-30% lower than J_{O2} flux without CO_2 counter-permeation, but the total J_{O2} calculated by Eq. 10 with CO_2-counter-permeation is about 30-50% larger than that J_{O2} for the same membrane without CO_2 counter-permeation. These results show that CO_2 counter-permeation increases the total O_2 permeation flux (oxygen ion flux) but it gives a lower O_2 apparent permeation flux measured from permeate side as compared to the case without CO_2 counter-permeation.

Table 3.4. *Comparison of typical oxygen permeation flux without and with CO_2 counter-permeation (at 850°C)*

Membrane	Pure O_2 flux (ml·cm^{-2}·min^{-1})	O_2 flux with CO_2 counter-permeation (ml·cm^{-2}· min^{-1})		
	J_{O2}	J_{O2}	J_{CO2}	$J_{O2(total)}$
PSCF-MC	0.125	0.109	0.200	0.209
SFT-MC	0.092	0.080	0.086	0.123

Oxygen permeation (or oxygen ion flux) through a mixed-conducting perovskite membrane depends on operation conditions especially the reaction conditions in the permeate side of the membrane (surface I). When a reactive gas is flowing through the permeate side, O_2 permeation flux increases with increasing reactivity of the gas in the permeate chamber (Rui *et al.*, 2009). Thus, with CO_2 counter-permeation, the reaction on the surface I:

$$CO_2 + O^{2-} \rightarrow CO_3^{2-} \qquad (3.E)$$
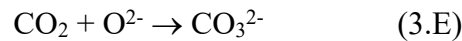
would reduce oxygen chemical potential in the permeate, and accordingly increases O_2 permeation (or oxygen ionic) flux as compared with the case with inert sweep gas, which only the relates to the following reaction:

$$O^{2-} \rightarrow 1/2O_2 + 2e^- \qquad (3.F)$$
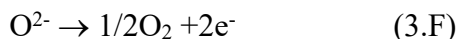
This explains the higher total O_2 permeation measured in counter-permeation. With higher oxygen ionic flux, the split of O^{2-} on surface I depends on the kinetic rate of the reaction 3.E and 3.F on surface I. The data in **Table 3.4** indicate that in counter-permeation, the J_{CO2} fluxes are about twice the O_2 flux for both membranes. This suggests that the rate for reaction 3.E is about four times the rate of reaction 3.F as defined in terms of consumption rate of oxygen ion on the membrane surface.

The above counter-permeation mechanism can also explain the transient (before reaching steady state) O_2 permeation data for the two membranes observed, as shown in **Figure 3.15**. The O_2 permeation flux at the permeate stream (from surface I) starts at a high value with He as the sweep in the permeate side. As soon as the sweep gas is switched to CO_2/He, the measured O_2 permeation flux declines in the first 16 minutes due to consumption of the transported oxygen ions for CO_2 permeation. The membrane now experiences a step increase of oxygen chemical potential gradient due to the introduction of CO_2 which reacts with the oxygen ions on surface I. The step increase in driving force provides a transient increase in oxygen ionic flux at first. When the permeation reached steady state, and measured oxygen permeation flux in the permeate stream stabilized.

Figure 3.16 compares CO_2 permeation flux through the two membranes without or with O_2 counter-permeation. The data in **Figure 3.16** and **Table 3.2** show very close fluxes and temperature dependence (activation energy) in the two cases for both membranes.

These results suggest that carbonate conduction through reaction 3.E consumes oxygen ions transporting through the membranes at the same rate without and with O_2 counter-permeation. As a result, CO_2 permeation fluxes are not affected by the counter-permeation of oxygen.
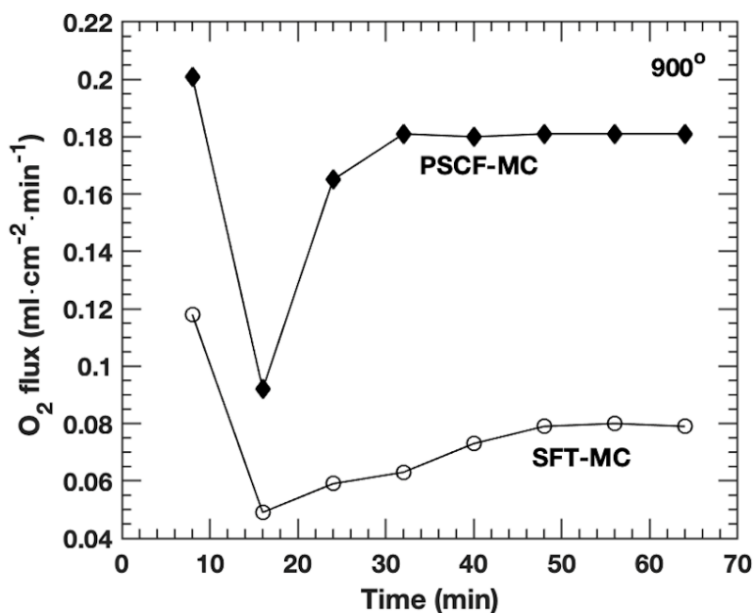
Figure 3.15. *Transient O_2 flux data when CO_2 being introduced to the system. CO_2 was introduced at the 0th minute of the timeline. GC samples were taken every 8 minutes in auto-sampling mode.*
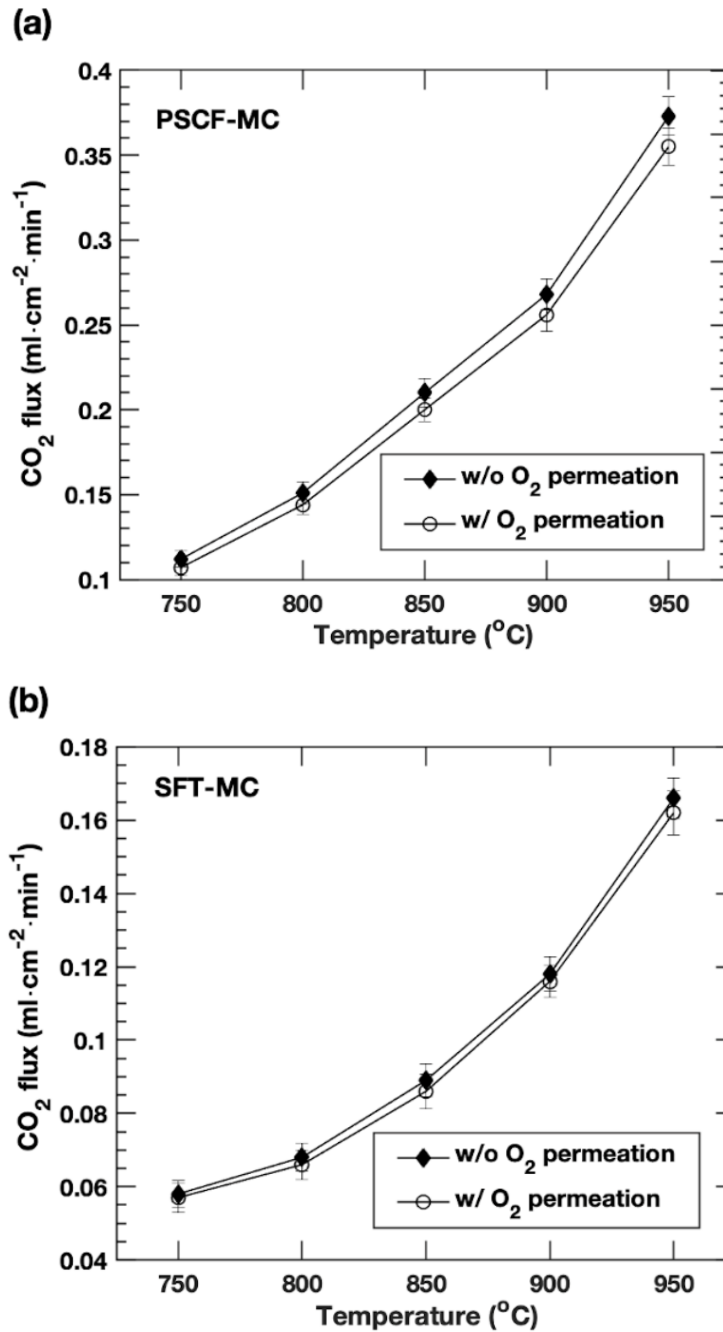
Figure 3.16. *CO_2 permeation flux of (a) PSCF-MC (b) SFT-MC membrane in both single component permeation and counter-permeation set-up at 750-950 °C. O_2 side: synthetic air 100 ml/min. CO_2 side: CO_2 50 ml/min, He 50 ml/min.*

3.4. Conclusions

For ceramic-carbonate dual-phase membranes consisting of mixed electronic-ionic conducting $Pr_{0.6}Sr_{0.4}Co_{0.2}Fe_{0.8}O_{3-\delta}$ and $SrFe_{0.9}Ta_{0.1}O_{3-\delta}$, without counter-permeation of another gas, O_2 permeation rate through the dual-phase membrane is controlled by oxygen ionic conduction in the ceramic phase and CO_2 permeation rate is determined by total conductance including effective carbonate and oxygen ionic conductivities in both phases. With CO_2 counter-permeation, the total oxygen permeation flux is higher than that without counter-permeation due to an increase in the driving force for oxygen transport. The consumption of oxygen ions by CO_2 permeation results in a lower O_2 flux measured in the permeate side. The ratio of CO_2 and O_2 fluxes is determined by the relative rate of the reactions for the formation of carbonate ion and molecular oxygen on the membrane surface exposed to CO_2. However, O_2 counter-permeation has negligible effect on CO_2 permeation flux for the dual-phase membranes.

CHAPTER 4

HYDROGEN PRODUCTION WITH CARBON DIOXIDE CAPTURE BY DUAL-

PHASE CERAMIC-CARBONATE MEMBRANE REACTOR VIA STEAM

REFORMING OF METHANE

4.1.   Introduction

Hydrogen is a clean fuel and an important feedstock in the chemical industry. As

mentioned in Chapter 1.2, the majority of hydrogen produced in the world today still come

from steam reforming of methane (SRM).

The SRM consists of multiple reactions and can be described as follows:

$$CH_4 + H_2O \leftrightarrow CO + 3H_2 \quad \Delta H = 206 \text{ kJ/mol} \quad (4.A)$$

$$CO + H_2O \leftrightarrow CO_2 + H_2 \quad \Delta H = \text{-41 kJ/mol} \quad (4.B)$$

$$CH_4 + 2H_2O \leftrightarrow CO_2 + 4H_2 \quad \Delta H = 165 \text{ kJ/mol} \quad (4.C)$$
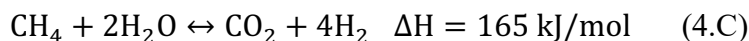
As indicated by reaction 4.A and 4.C, the reactions require much energy to occur. As a

result, one of the biggest problems is that the process is very energy intensive. Furthermore,

since the reactant is still fossil fuel, CO_2 emission is inevitable. To mitigate the

environmental impact of SRM process, the concept of membrane reactor was introduced

as a measure to promote the process efficiency.

For the past decades, research community has been devoted the effort to extract

hydrogen with the membrane. As introduced in Chapter 1.2.3, Pd-based membrane has

been the most well-studied type of membrane for this particular application, while a few

other research groups were focused on microporous silica membrane development (Tsuru

et al., 2004; Tong *et al.*, 2005; Ma *et al.*, 2015; Anzelmo, Wilcox and Liguori, 2017). In

general, Pd-based membrane exhibited promising performance with high permeation flux and theoretically infinite selectivity of hydrogen over other gas components. However, the high materials cost and structural instability have severely hindered Pd-based membranes from being used in the field (Kumpmann, Günther and Kunze, 1993; Bryden and Ying, 1995; Dolan *et al.*, 2006).

While CO_2 being another end product of SRM reaction, its separation from an SRM reactor has never been demonstrated. CO_2-permselective membranes could also be good alternatives to increase methane conversion or enhance H_2 production in SRM. The concept of a CO_2-removal SRM membrane reactor is illustrated in **Figure 4.1**. The membrane offers in situ CO_2 removal while the reaction takes place. Based on the chemical equilibrium principle, reactions 4.B and 4.C will be shifted towards the product side and enhance the hydrogen production. In the past, extensive efforts have been made in developing polymeric (Lin *et al.*, 2006; Merkel *et al.*, 2010) and molecular-sieving (Caro and Noack, 2008; Battersby *et al.*, 2009; Kanezashi and Lin, 2009) membranes with CO_2 permeability. However, these membranes do not work at high temperatures required by SRM. Lin and coworkers and a few others have conducted a series of research on dense ceramic-carbonate dual-phase membranes for CO_2 separation (Anderson and Lin, 2010; Wade *et al.*, 2011; Rui *et al.*, 2012; Sherman *et al.*, 2012; Xu *et al.*, 2012; Zhang *et al.*, 2012; Lu and Lin, 2013; Ortiz-Landeros, Norton and Lin, 2013; Zuo *et al.*, 2014; Jiang *et al.*, 2016). Most notably, Dong and Lin (Dong and Lin, 2016) successfully demonstrated enhanced WGS reaction by a catalyst-free ceramic-carbonate membrane reactor. In their work, the WGS was effectively shifted by the membrane reactor and showed considerably higher CO conversion than a conventional fixed-bed reactor under the same condition.

85
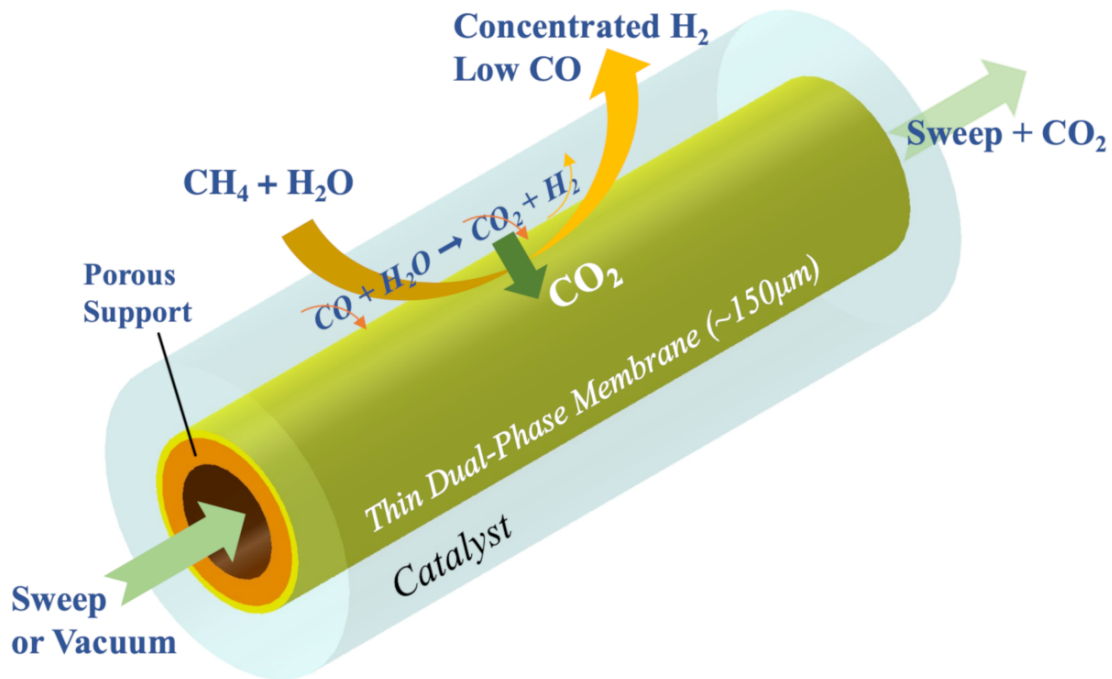
Figure 4.1. *Illustration of a CO_2-permselective SRM membrane reactor.*

One of the major challenges of ceramic-carbonate membranes is the difficulty of fabricating a thin gas-tight dual-phase membrane (<500 μm). This is because the molten carbonate can infiltrate most types of ceramic support, and the support has to be thick enough to provide adequate mechanical strength. Dong et al. (Dong, Ortiz-Landeros and Lin, 2013) and Lu et al. (Lu and Lin, 2014) tackled this problem by introducing bismuth-yttrium-samarium oxide ($Bi_{1.5}Y_{0.3}Sm_{0.2}O_{3-\delta}$, BYS) into the support. The unique carbonate repellant property of BYS makes it an excellent support material. In addition, BYS has similar crystal structure to the well-studied samarium-dope ceria ($Sm_{0.2}Ce_{0.8}O_{2-\delta}$, SDC), which has been researched for gas separation and fuel cell applications (Huang *et al.*, 2006; Xia *et al.*, 2010; Norton, Lu and Lin, 2014). The intrinsic material property makes BYS

chemically compatible with SDC (Dong, Ortiz-Landeros and Lin, 2013). Therefore, an asymmetric-structured membrane with a thick BYS-SDC support layer and a thin SDC-carbonate permselective layer can be fabricated. Due to much lower ionic diffusion resistance, the asymmetric membrane exhibits significantly higher CO_2 flux than the symmetric-structured thick SDC-carbonate membrane (Dong, Ortiz-Landeros and Lin, 2013).

Despite a number of studies have been conducted on the H_2-removal approach to promote the efficiency of SRM, to the best of the author's knowledge, this is the first CO_2-removal membrane reactor demonstration. Inspired by the distinctive performance of BYS-SDC asymmetric thin dual-phase membrane, the author decided to implement this concept of membrane reactor to perform SRM. With its in situ CO_2 removal capability, WGS reaction can be enhanced and H_2 concentration in the retentate is expected to increase significantly. The main objectives of this work are (1) demonstrate the CO_2 removal capability of the BYS-SDC-carbonate membranes to facilitate SRM, and (2) assess H_2 production enhancement by comparing the results from membrane reactor and the conventional fixed-bed reactor.

4.2. Experimental

4.2.1. Membrane Synthesis and Characterization

BYS ($Bi_{1.5}Y_{0.3}Sm_{0.2}O_{3-\delta}$) and SDC ($Sm_{0.2}Ce_{0.8}O_{2-\delta}$) powders were synthesized via liquid citric method as reported previously by Lin and coworkers (Ortiz-Landeros, Norton and Lin, 2013). For the synthesis of BYS, stoichiometric amounts of $Bi(NO_3)_3 \cdot 5H_2O$, $Y(NO_3)_3 \cdot 6H_2O$ and $Sm(NO_3)_3 \cdot 6H_2O$ and solid citric acid (all from Alfa Aesar, at least 98% of purity, ACS reagent grade) were mixed together. For citric acid, the molar ratio of total metal ions to citrate is 1:2. The mixture was dissolved into a nitric acid solution (10 vol% HNO_3) with continuous agitation. The solution was then heated to 250 °C to evaporate the excess water. Once the water was removed, the remaining gel-like mixture was then heated up to 350 °C to bring up self-ignition for removal of carbon content. The waffle-like mixture produced after self-ignition was then collected and calcined at 850 °C for 5 h. The synthesis of SDC powders was achieved by the same method, but the water solution was prepared without addition of nitric acid and the powder was separated into two batches calcined at 950°C and 550 °C for 5 h respectively. The main reason for separating the SDC powder into two batches and calcine them at two different temperatures is to create SDC powders of two different particle sizes. As the outer permselective layer is only about 100 μm thick, it requires SDC powder (sintered at 550°C) with fine and uniform particle size to prevent defect. Moreover, the SDC calcined at 950 °C generally has particle size similar to BYS sintered at 850 °C. The yield for defect-free, high quality SDC-BYS support was higher when using uniform size particles.

88

The tubular membrane was prepared via the centrifugal casting method patented by Lin and coworkers (Dong, Ortiz-Landeros and Lin, 2013; Lin, Ortiz-Landeros and Dong, 2016). BYS-SDC slurry was first to be prepared with the powder composition of 55 wt% SDC (calcined at 950 °C) and 45 wt% BYS mixed with water in 50 wt%:50 wt%. A few drops of 3% polyvinyl alcohol (PVA) solution was added to the mixture to improve mechanical strength of the ceramic body. The mixture was ball-milled at 175 rpm for at least 3 h to form a homogeneous slurry. SDC slurry was prepared via the same method by using SDC powder calcined at 550°C. The SDC slurry was then poured into a stainless-steel mold with inner diameter of 1.3 cm and sealed by rubber stoppers. Centrifugation was performed for 20 min at the rate of 4500 rpm to achieve solid-liquid separation, then the SDC layer was formed as the liquid was drained. The BYS-SDC slurry was added subsequently and the same centrifugation was performed again to make a support layer. The ceramic body was dried before detaching the mold in a humidity chamber at 40 °C with a relative humidity of 60% for at least 12 h. The asymmetric tube with a thin SDC layer and a BYS-SDC support layer was obtained after sintering at 1150 °C for 12 h. The sintered support was immersed directly into molten carbonate at 550 °C. The molten carbonate mixture consists Li_2CO_3, Na_2CO_3 and K_2CO_3 in molar ratio of 42.5:32.5:25. Due to the repellant property of BYS, only the thin SDC thin layer was infiltrated by the molten carbonate. The membrane synthesis was completed after the infiltration process.

The membrane morphology and phase structure were examined by scanning electron microscopy (SEM, Amray 1910) and X-ray diffractometry (PanAlytical X'Pert Pro). Membrane samples before and after performing SRM reaction were both examined.

Additional characterization information about energy dispersive spectroscopy (EDS) images for elemental distribution at the cross section of the membrane, and pore size distribution of the membrane support (before molten carbonate infiltration), are presented in elsewhere (Dong, Wu and Lin, 2018).

4.2.2. CO_2 Permeation and Steam Reforming of Methane (SRM) Reaction

Both non-reactive CO_2 permeation test and SRM reaction were carried out on a built-in-house permeation set-up, as shown in **Figure 4.2**. The high temperature gas-tight sealing was achieved by a ceramic paste. The ceramic paste was prepared by mixing 40 wt% SDC powder, 50 wt% Pyrex powder and 10 wt% $Al_2O_3 \cdot Na_2O$ together and ground with a little amount of deionized water. After the ceramic paste was evenly applied and well dried, the system was heated to 750 °C in the rate of 1 °C/min and held for at least 5 h to melt the paste and achieve gas-tight sealing. Preliminary gas-tightness test was carried out by introducing 100 ml/min nitrogen on the feed side and 100 ml/min helium on the sweep side at 750 °C. If gas leakage occurred, N_2 should be detected by the gas chromatography (GC, Agilent 7890A) from the permeate side. Only after gas-tightness is confirmed, the membrane would be used for subsequent experiments.
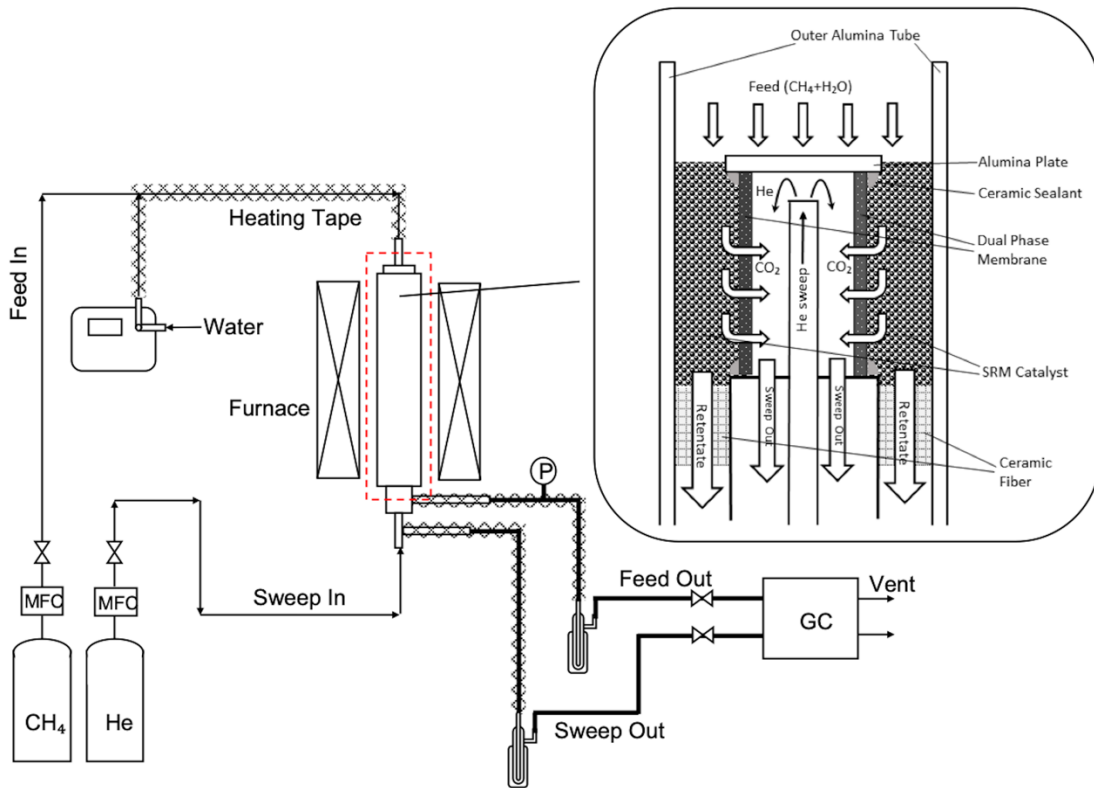
Figure 4.2. Schematic of tubular BYS-SDC ceramic-carbonate membrane reactor for SRM reaction.

In non-reactive CO_2 permeation, a N_2/CO_2 mixture of 50%/50% molar ratio, 50 ml/min was supplied as the feed. In SRM tests, steam/methane (S/C) ratio was controlled at 3 and the CH_4 flow rate was controlled at 5 ml/min. Deionized water was injected by a syringe pump into pre-heated stainless-steel pipe to generate steam. The tubular asymmetric dual-phase membranes were about 0.6 cm in I.D. and around 3.5 cm in length, with the effective permeation area of about 7 cm^2. 0.2 g of Ni-based catalyst (HiFUEL R110) was mixed with 2 g fused silica (3M Ceradyne) uniformly before loaded in each experiment run. Both the catalyst and fused silica were crushed and sieved to 24~60 mesh grains. The catalyst was activated by 100 ml/min, 5 mol% H_2/95 mol% He mixture at 800 °C for 8 h before use. Both sides of the membrane were maintained at atmospheric pressure

in all tests. The gas composition was analyzed by a GC (Agilent 7890A) with a HayeSep DB 100/120 (AllTech) column. The flow rate of both feed-out and sweep-out streams were measured by a soap film flow meter. The CH_4 conversion (X_{CH_4}) was calculated as follows:

$$X_{CH_4} = \frac{F_{CH_4}^{feedin} - F_{CH_4}^{feedout} - F_{CH_4}^{sweepout}}{F_{CH_4}^{feedin}} \times 100\% \qquad (4.1)$$

where $F_{CH_4}^{feedin}$, $F_{CH_4}^{feedout}$ and $F_{CH_4}^{sweepout}$ represent the CH_4 flow rate of feed-in, feed-out and sweep-out gas stream in the membrane reactor, respectively.

The CO_2 recovery (R_{CO_2}) was calculated as follows:

$$R_{CO_2} = \frac{F_{CO_2}^{sweepout}}{F_{CO_2}^{feedout} + F_{CO_2}^{sweepout}} \times 100\% \qquad (4.2)$$

where $F_{CO_2}^{feedout}$ and $F_{CO_2}^{sweepout}$ are the CO_2 flow rate of feed-out and sweep-out stream, respectively.

The hydrogen yield (Y_{H_2}) was calculated as follows:

$$Y_{H_2} = \frac{F_{H_2}^{feedout}}{F_{CH_4}^{feedin} \times 4} \times 100\% \qquad (4.3)$$

where $F_{H_2}^{feedout}$ is the H_2 flow rate of feed-out stream.

For conventional fixed-bed experiments, the permeate side (sweep out in **Figure 4.2**) was closed and the equilibrium of CO_2 concentration was reached. In doing so, the reaction will take place under the same conditions except there will be no CO_2 permeation flux across the membrane.

4.3. Results and Discussions

4.3.1. Membrane morphology

The as-synthesized tubular membrane exhibits a two-layered asymmetric wall structure, as shown in **Figure 4.3(a)**. The EDS elemental mapping presents the difference in compositions between the two layers. As **Figure 4.3(b)** shows, bismuth (red dots) mainly presents in the inner support layer. **Figure 4.3(c) and 4.3(d)** present the high magnification view of the support layer and the permselective layer, respectively. The figures clearly show the dense structure of the SDC-carbonate layer and the porous structure of the support layer. The repellent property of BYS likely results from the acidity of bismuth. Since the molten carbonate is also mildly acidic, the surface energy will be higher when the molten carbonate contacts BYS ceramic surface. The presence of Bi element in the dense layer showing in the EDS elemental mapping could result from (1) small amount of powder from support layer fall onto the dense layer when preparing the sample (2) inaccuracy of the instrument (3) minor diffusion of Bi into the dense layer during the sintering process. Despite the minor presence of Bi, it can be seen that the concentration of Bi in the support layer is clearly much higher than in the dense layer. The minor presence of Bi does not affect the property of the dense layer.

It should be noted that all the membranes used in this work had the thin SDC layer on the outer side of the tube, which is different from similar works in the literature (Dong, Wu and Lin, 2018). The purposes for this change are to (1) increase membrane area per unit length and (2) expose the more stable SDC layer against the reaction.
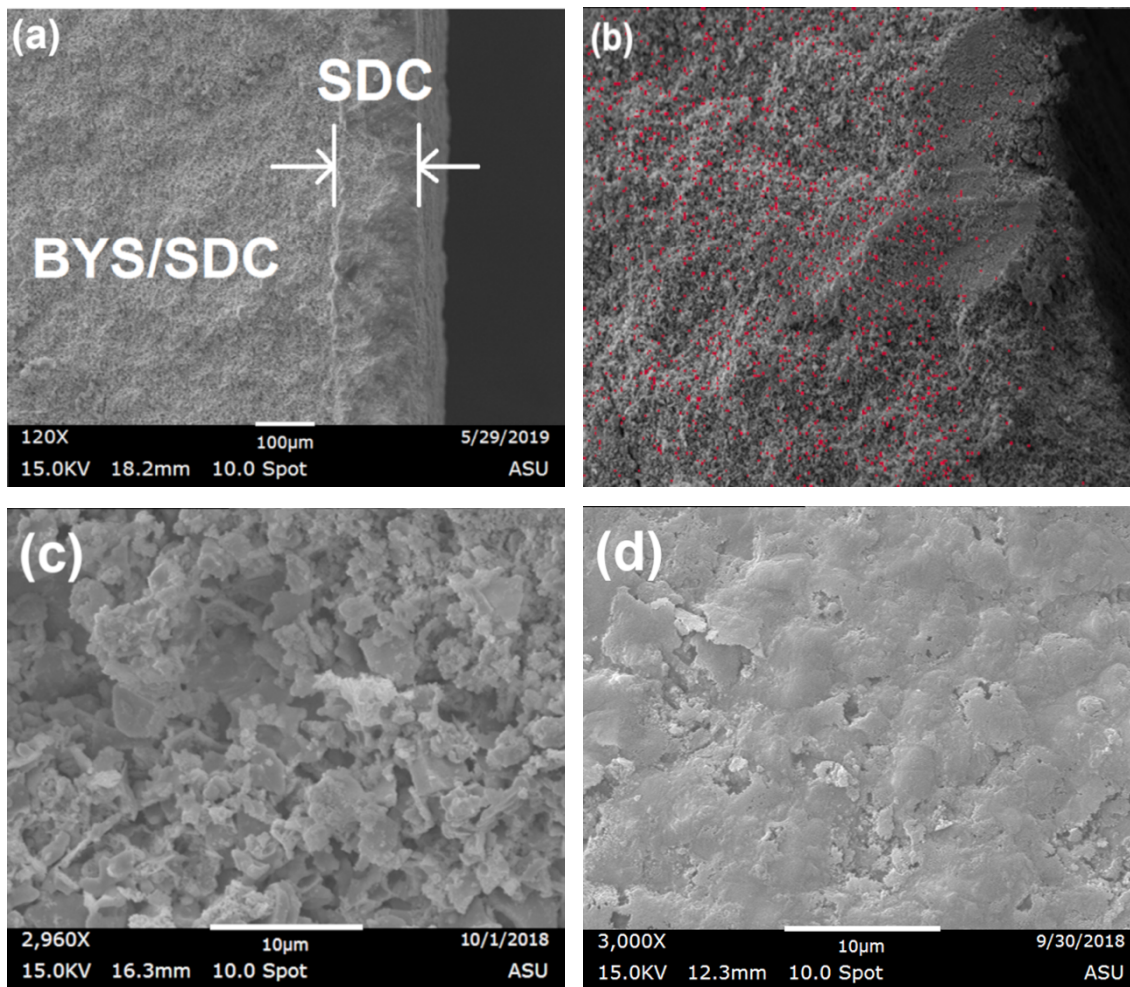
Figure 4.3*. SEM image of (a) the asymmetric structure of the membrane (b) EDS elemental mapping of bismuth (red dots) (c) BYS-SDC support layer and (d) SDC-carbonate (infiltrated) permselective layer.*

4.3.2. CO$_2$ Permeation Properties of BYS-SDC Asymmetric Membrane

Non-reactive CO$_2$ permeation experiments were conducted to evaluate the general CO$_2$ permeation performance of the membrane. As shown in **Figure 4.4**, the CO$_2$ permeance ranges from 7.8×10^{-8} mol·m^{-2}·s^{-1}·Pa^{-1} to 2.24×10^{-7} mol·m^{-2}·s^{-1}·Pa^{-1} and the CO$_2$ permeation flux ranges from 0.37 ml·cm^{-2}·min^{-1} to 1.71 ml·cm^{-2}·min^{-1}. When SRM is

carried out in the membrane reactor, CO_2 flux decreases in membrane reactor when S/C > 3, as presented in **Figure 4.5**. The phenomenon is likely due to excess steam diluting the CO_2 concentration and lowering the driving force for CO_2 permeation. Whereas when S/C is low, the conversion is lower and fewer CO_2 is produced, which results in lower driving force and hence lower permeation flux.
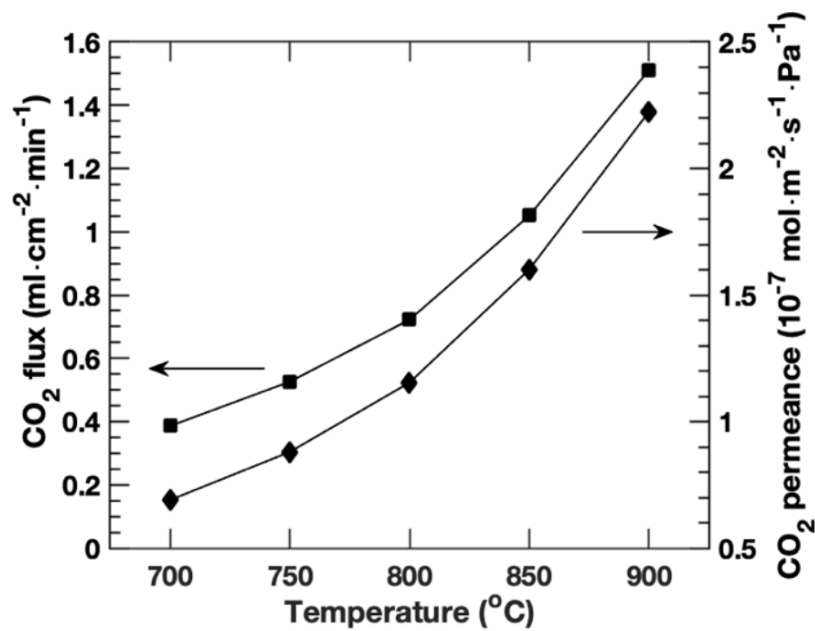
Figure 4.4*. CO_2 flux and permeance in non-reactive conditions at 700-900 °C. Feed: CO_2 = 25 ml/min, N_2 = 25 ml/min. Sweep: He = 50 ml/min. Both feed and sweep sides are at 1 atm.*
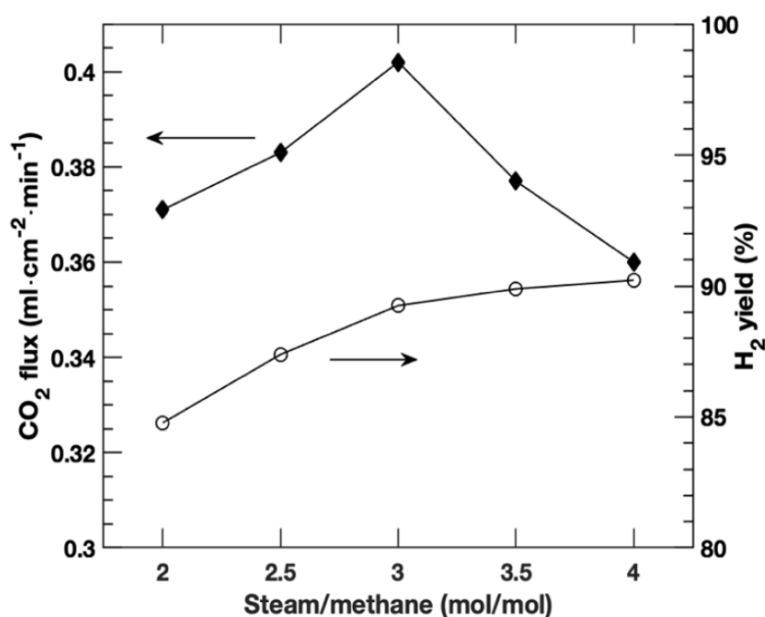
Figure 4.5. CO_2 *permeation flux and H_2 yield when S/C = 2-4 (CH_4 = 5 ml/min) in SRM condition at 800°C. Sweep gas: He = 200 ml/min. Both sides of the membrane were kept at 1 atm.*

Figure 4.6 presents CO_2 permeation flux and CO_2 recovery of the membrane reactor while performing SRM reaction at 700-900 °C, respectively. In the reactive conditions, CO_2 flux reaches from 0.15 ml·cm^{-2}·min^{-1} to 0.4 ml·cm^{-2}·min^{-1}, and the CO_2 recovery ranges from 42-84%. The CO_2 recovery is remarkably high compared with the symmetric WGS membrane reactor reported previously (Dong and Lin, 2016). The significantly improved CO_2 recovery indicates that the reduced membrane thickness effectively enhances the performance of the membrane reactor in terms of CO_2 capture capability.

Figure 4.7 compares CO_2 permeation fluxes under SRM reactive conditions with those under non-reaction conditions obtained in this work, and similar results for thicker membranes with and without WGS reactions. The fact that the CO_2 permeation fluxes

96

under reaction conditions are lower than under non-reaction conditions is because under reaction conditions the CO_2 partial pressure in the reactive gas for SRM or WGS (at total pressure of 1 atm) is lower, and hence a lower driving force for CO_2 permeation, than under non-reaction conditions (CO_2 partial pressure is 0.5 atm in this work). The apparent activation energies for CO_2 permeation in both non-reactive and reactive conditions were calculated via an Arrhenius plot. As **Figure 4.7** shows, the apparent activation energy measured in this work (64.7 kJ/mol) is lower than previously reported thick membrane (83.3 kJ/mol) for non-reactive permeation. The difference might be caused by the effect of surface reaction rate.
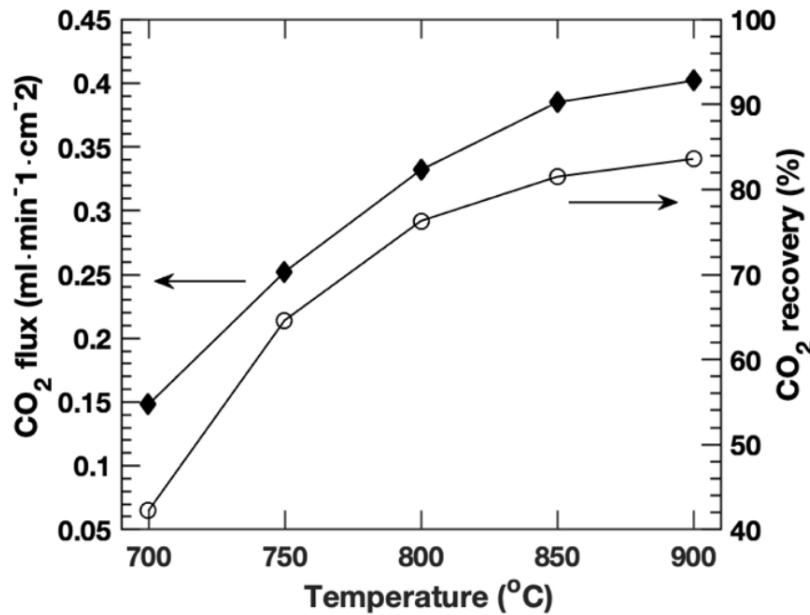
Figure 4.6. *CO_2 permeation flux and CO_2 recovery of membrane reactor performing SRM at 700-900 °C. Sweep: He = 200 ml/min. Feed: CH_4 = 5 ml/min, S/C = 3. Both sides of the membrane were kept at 1 atm.*
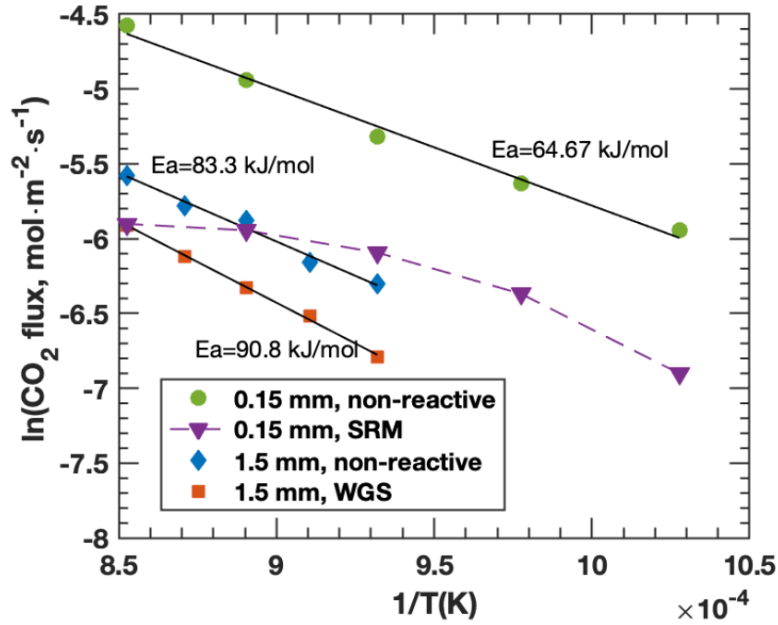
Figure 4.7. *Arrhenius plot of CO₂ flux of asymmetric membrane reactor in non-reactive condition and SMR condition, and of symmetric membrane reactor in non-reactive condition and WGS condition. In SRM reactor: Sweep: He = 200 ml/min. Feed: CH₄ = 5 ml/min, S/C = 3. Both sides of the membrane were kept at 1 atm. Data of symmetric membrane reactor are from reference (Dong and Lin, 2016).*

When the membrane is relatively thick, CO_2 permeation is controlled by transport of oxygen and carbonate in the bulk of the SDC and molten carbonate phase respectively, and the permeation flux is proportional to the membrane total conductance, which can be expressed as follows (Norton, Lu and Lin, 2014):

$$\alpha = \frac{\phi_p \sigma_c \phi_s \sigma_i}{\phi_p \sigma_c + \phi_s \sigma_i} \tag{4.4}$$

where σ_c and σ_i are the carbonate ionic conductivity of the carbonate phase and oxygen ionic conductivity of the ceramic phase, respectively. ϕ_p and ϕ_s represent the geometric factor of the pore and solid phase of the support, respectively. More specifically, ϕ_p equals to porosity (ϵ) to tortuosity (τ) ratio ($\phi_p = \epsilon/\tau$), and ϕ_s the relative cross-sectional area for

solid phase to the solid tortuosity. In the case of SDC-carbonate membrane, σ_c is much larger than σ_i, and α can be approximated as:

$$\alpha \sim \phi_s \sigma_i(T) \qquad (4.5)$$

Table 4.1. *SDC-carbonate series membranes reported in literature and this work.*

Membrane	Dense layer thickness (mm)	Feed	Sweep	E_a (kJ/mol)	Ref.
SDC-carbonate	1.5	50% CO_2, 50% N_2	100% He	83.3	(Dong and Lin, 2016)
		49.5% CO, 36% CO_2, 10% H_2, 4.5% N_2	100% He	90.8	
BYS-SDC-carbonate	0.15	50% CO_2, 50% N_2	100% He	64.7	This work
		25% CH_4, 75% H_2O	100% He	70.2 (700-800°C) 19.3 (800-900°C)	
SDC-carbonate	0.8		100% He	64.7	(Chen et al., 2019)
SDC-BYS three-layered	0.65	10% H_2, 45% CO_2, 45% N_2	100% He	60.2	
SDC-BYS two-layered	0.1		100% He	54.9	

Under such a scenario, the permeation activation energy is determined by the activation energy of σ_i. However, the literature also suggest that when the membrane thickness is reduced to a certain extent, surface reaction rate might become significant to permeation rate (Bouwmeester, Kruidhof and Burggraaf, 1994; Sunarso *et al.*, 2008). Suppose the activation energy for the surface reaction involved in conversion between CO_2/O^{2-} and CO_3^{2-} is lower than the oxygen ionic activation energy in the SDC solid phase, the measured apparent activation energy for CO_2 permeation through the thin SDC-carbonate membrane will become lower compared with the bulk-transport-control case. The activation energies measured by Chen et al. (Chen *et al.*, 2019) on membranes with

various thickness also decrease when reducing membrane thickness, which provides evidence to support this explanation. The comparison of membranes reported in the literature and this work is presented in **Table 4.1**. From the above analysis and activation energy data, we can conclude that the surface reaction for SDC-carbonate membrane likely has lower activation energy than the oxygen ionic conductivity σ_i in the SDC phase.

Another noteworthy phenomenon displayed in **Figure 4.7** is that the activation energy for CO_2 permeation in SRM condition is further decreased, whereas the activation energy in the WGS reactor (90.8 kJ/mol) is slightly larger than non-reactive permeation (83.3 kJ/mol). Also, the Arrhenius plot of SRM data show non-linearity, hence the data were divided into two sections, 700-800 °C and 800-900 °C, and regressed separately. Two activation energies were calculated (70.3 kJ/mol and 19.2 kJ/mol), representing each section. It can be explained by the comparison of the trend of conversion with respect to temperature from the two reactors, as shown in **Figure 4.8**. For the experiments with the thick, symmetric membrane reactor, WGS was conducted under catalyst-free conditions.

As shown in the Figure, the WGS reaction rate is slow and conversion is low. Under such conditions, both WGS reaction kinetic and oxygen ionic conductivity in SDC affect CO_2 permeation. The higher activation energy in the WGS case reflects the contribution of WGS reaction kinetic (higher than 88 kJ/mol with a catalyst (Hla *et al.*, 2009)). On the contrary, SRM was performed with an efficient SRM catalyst in the asymmetric membrane reactor. The lower CO_2 permeation flux with SRM (as compared to non-reactive gas) is due to lower driving force for CO_2 permeation as explained above. This is because under reaction conditions the CO_2 partial pressure in the reactive gas for SRM is lower than in the non-reactive condition, which results lower the CO_2 permeation fluxes**.** The activation

energy for permeation with reactive gas under SRM at lower temperatures (700-800 °C) is similar to that for permeation with non-reactive gas (see **Table 4.1**). The apparent activation energy decreases with increasing temperature due to the surface reaction (with lower activation energy as discussed above) more likely becoming the rate-determining factor.
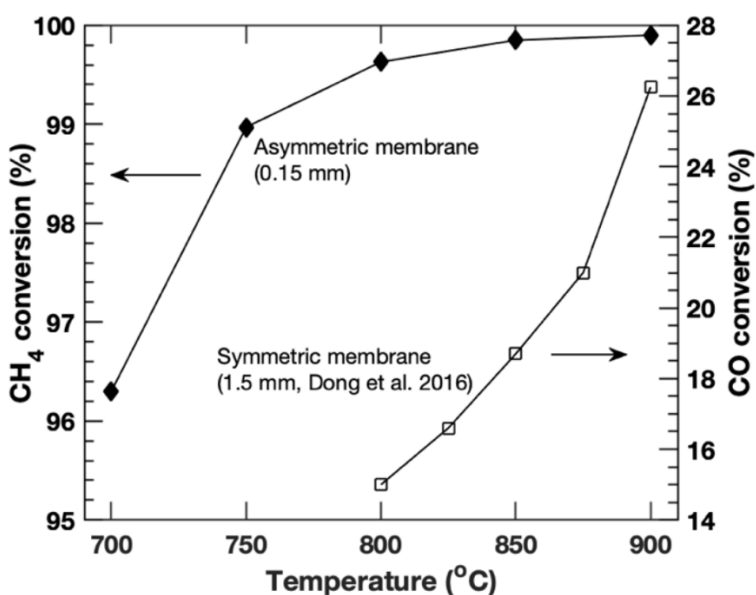
Figure 4.8. Comparison of feed conversion between asymmetric membrane reactor in this work and symmetric membrane reactor reported in literature (Dong and Lin, 2016). For asymmetric membrane: Sweep: He = 200 ml/min. Feed: CH_4 = 5 ml/min, S/C = 3. Both sides of the membrane were kept at 1 atm.

4.3.3. SRM in the Asymmetric Membrane Reactor

Figure 4.9 compares CH_4 conversion and H_2 yield for SRM in the membrane reactor with that in the fixed-bed reactor under the same conditions. As presented in the figure, the membrane reactor only provides slight promotion in CH_4 conversion in comparison with the conventional fixed-bed reactor. Since the membrane can provide sufficiently high CO_2 flux only when the temperature is at least about 700 °C, the reactor was run at high temperatures. In such conditions, CH_4 conversion is already very high and the room for promoting conversion becomes very limited. In spite of that, the conversion data indicate the membrane reactor is capable of achieving almost equilibrium conversion.
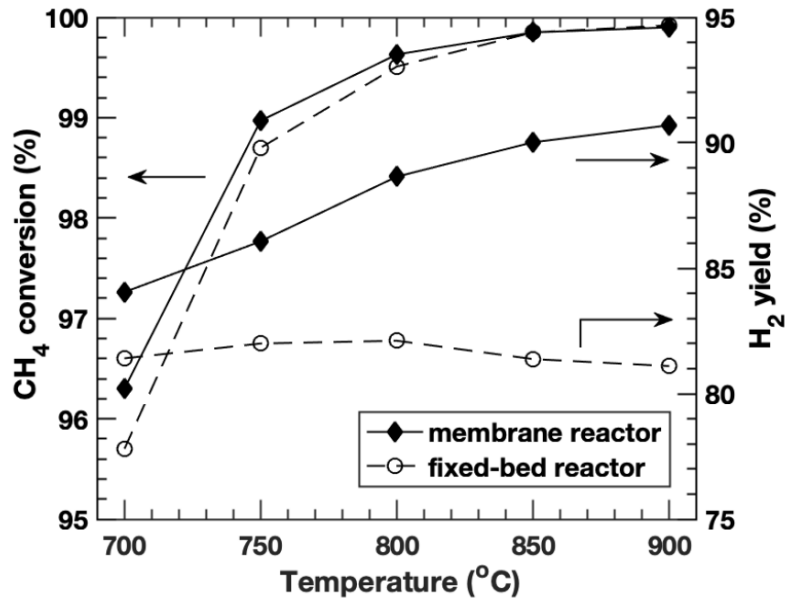
Figure 4.9. *CH_4 conversion and H_2 yield of the membrane reactor and conventional fixed-bed reactor at 700-900 °C. Sweep: He = 200 ml/min. Feed: CH_4 = 5 ml/min, S/C = 3. Both sides of the membrane were kept at 1 atm.*

The major advantage of this type of membrane reactor is to enhance H_2 yield. In addition, such an effect of CO_2 removal becomes more prominent with increasing temperature as the CO_2 flux increases with increasing temperature, also as shown in **Figure 4.9**. At 900 °C, the H_2 yield in membrane reactor reaches about 90%, which presents remarkable improvement from about 81% out of the conventional fixed-bed reactor. Moreover, the use of the asymmetric membrane has apparent effects on product composition. As shown in **Figure 4.10**, the output H_2 concentration is improved from 76% to 88% (dry-based) by the membrane reactor. Meanwhile, the CO concentration (presented in Figure **4.11**) is reduced from 18% to 8% (dry-based) at 900 °C. The concentration changes evidently show that the membrane reactor effectively improves WGS conversion.

Figure 4.12 presents the product composition change from 700-900 °C in the membrane reactor. Despite high CO conversion at high temperature, CO_2 concentration in the retentate still decreases with increasing temperature as the thin asymmetric membrane offers very effective in situ CO_2 removal. Due to limited capability of the experiment set-up, SRM with pressurized feed and vacuum on the permeate side was not demonstrated. Implementing these two techniques will create a greater CO_2 pressure gradient across the membrane and maximize the performance of this membrane reactor. In doing so, the membrane reactor can potentially produce very high concentration of H_2 with pure CO_2 capture in single stage. Nevertheless, without the high pressure data, the results of the experiments conducted at 1 atm still show that this new membrane reactor concept for SRM process poses great potential for process intensification, as no other existing technology have the capability of simultaneous production of high purity, high pressure H_2 and separation of CO_2 from the reactant/product stream.
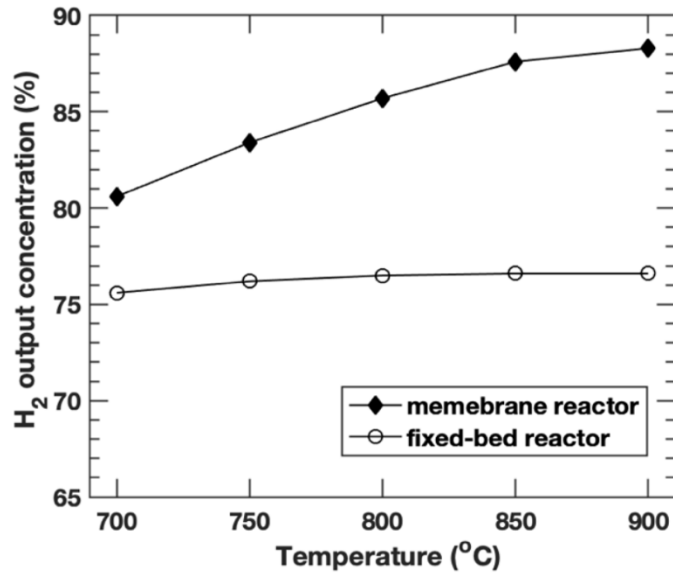
Figure 4.10. *H₂ output concentration (dry-based) comparison of the membrane and fixed-bed reactor. Sweep: He = 200 ml/min. feed: CH₄ = 5 ml/min, S/C = 3. Both sides of the membrane were kept at 1 atm.*
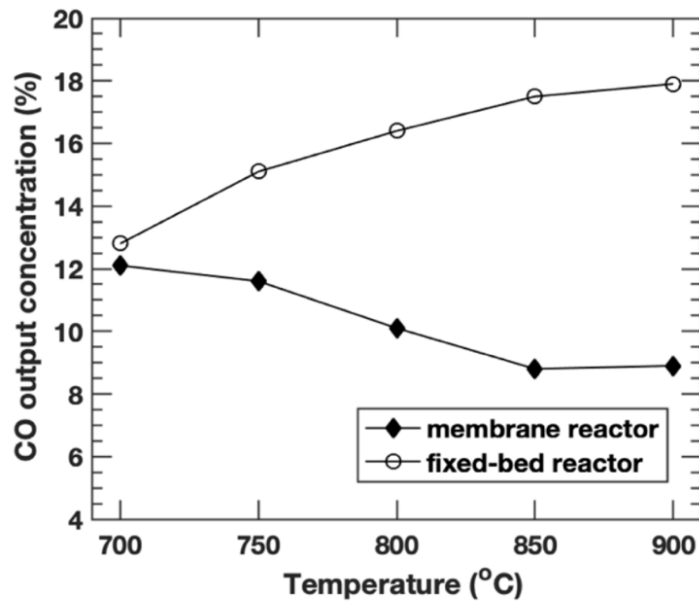
Figure 4.11. *CO concentration (dry-based) comparison of the membrane and fixed-bed reactor. Sweep: He = 200 ml/min. feed: CH₄ = 5 ml/min, S/C = 3. Both sides of the membrane were kept at 1 atm.*
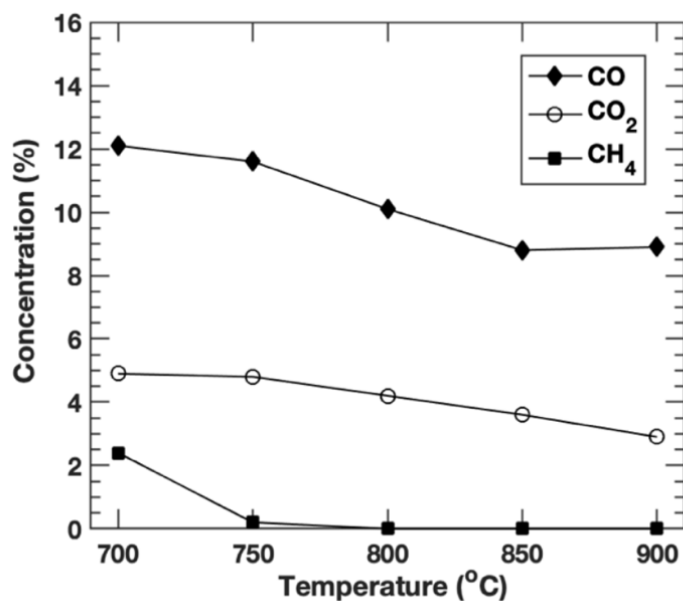
Figure 4.12. *Retentate gas composition (dry-based) of the asymmetric membrane SRM reactor. Sweep: He = 200 ml/min. feed: CH₄ = 5 ml/min, S/C = 3. Both sides of the membrane were kept at 1 atm. Hydrogen data are not included due to large difference in scale (refer to Figure 9 for H₂ data).*

4.3.4. Membrane Stability

For a given membrane, the SRM membrane reactor test at high temperatures typically lasted about 100 h when a sudden increase in hydrogen concentration in the permeate, from zero (undetectable by GC) to about 8%, was observed. With 200 ml/min He sweep, this means a hydrogen permeation flux of about 24 ml/min. Such large flux was due to failure in sealant and the part of the membrane attached to the sealing, as thin cracks near the edge of the membrane were observed after membrane was removed from the reactor. However, the bulk part of the membrane remained in good integrity.

The post-test membranes removed from the reactor were examined by SEM and XRD and the results are compared with the fresh membranes in **Figures 4.13** and **4.14**. In **Figure 4.13 (a)**, the reaction side of a post-test sample shows some recrystallization of carbonates, which is likely formed in the cooling process. Other difference besides from the recrystallization was not observed, for both reaction and sweep side. As for the XRD patterns **(Figure 4.14)**, although the post-testing membrane sample shows slightly weaker X-ray diffraction intensity, there are no other discernable difference in material phase structures. Both the characterization results indicate that the membrane has good chemical stability under SRM conditions.
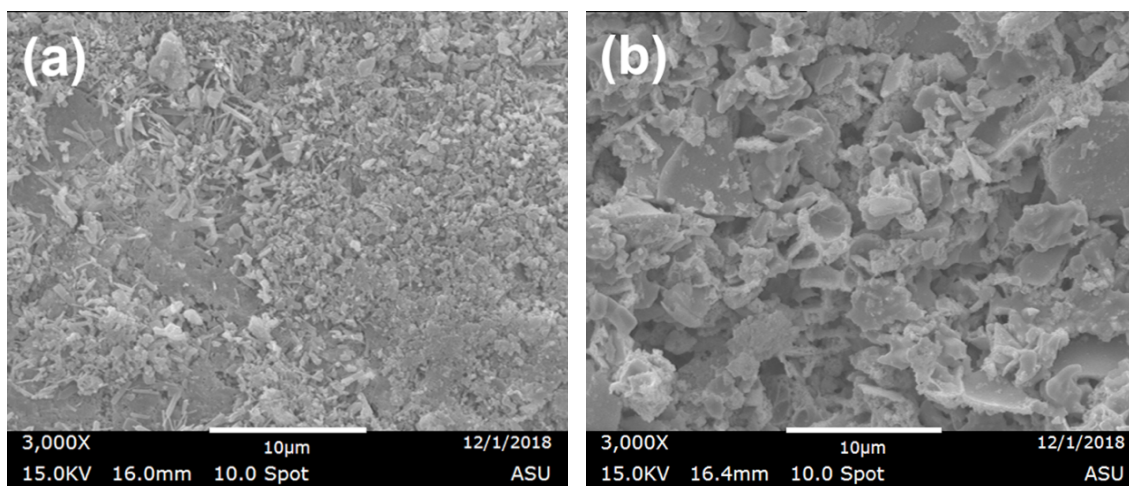
Figure 4.13. *SEM images of BYS-SDC ceramic-carbonate membrane (a) reaction side and (b) sweep side after test.*
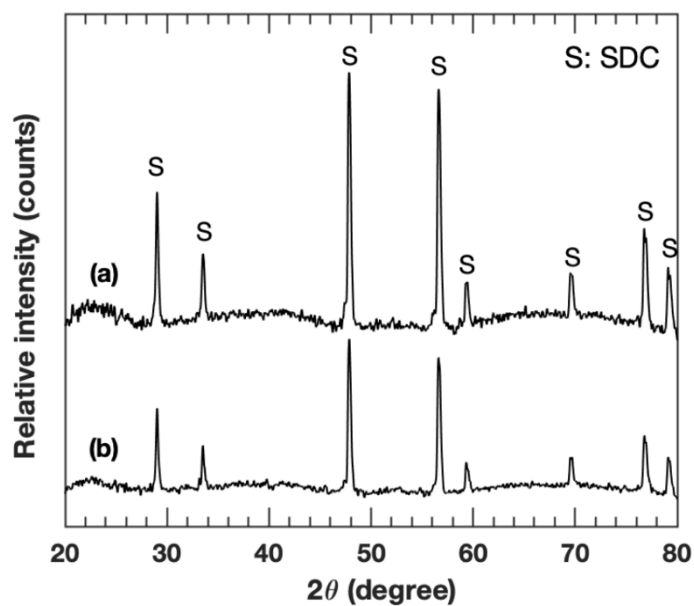
Figure 4.14. *XRD patterns of (a) fresh and (b) post-test membrane (reaction side).*

4.4.   Conclusions

The asymmetric, thin BYS-SDC ceramic-carbonate membrane reactor can effectively convert methane to hydrogen via SRM with CO_2 removal. The results of this study clearly suggest that the CO_2 removal capability of the asymmetric thin ceramic-carbonate membrane reactor can produce high concentration H_2 in a single-stage membrane reactor with CO and CO_2 in the retentate stream reduced to a minimal level. As a result, the reactor footprint can be significantly reduced as no extra WGS unit is needed. CO_2 permeation fluxes for the ceramic-dual phase membranes with reactive gas feed are lower than with non-reactive gas feed under similar conditions, with varying activation energy depending on the relative reaction rate and CO_2 permeation mechanism. The work shows a new membrane process to produce high purity H_2 stream directly from the reactor with simultaneous separation of CO_2. SEM and XRD analysis suggest that the membrane has good chemical stability in SRM environment.

CHAPTER 5

A MODELING STUDY ON CO2-PERMSELECTIVE MEMBRANE REACTOR
PERFORMING STEAM REFORMING OF METHANE

5.1.   Introduction

A simulation study is very practical to assess the membrane reactor performance
in industrial conditions without facing the technical difficulties of making robust
industrial-grade membrane or sealings. Since the majority of the research on SRM, both
experimental and theoretical, were focused on hydrogen separation (Barbieri *et al.*, 2001;
Tsuru *et al.*, 2004; Patel and Sunol, 2007; Ma *et al.*, 2015), no simulation work
investigating CO_2-perselective SRM membrane reactor has ever been reported.
Therefore, the purpose of this research is to develop a membrane reactor model and use
the model to gain insights of how the CO_2-permselective SRM membrane reactor would
perform under industrial conditions.

The concept of using a CO_2-permselective dual-phase membrane to enhance the
WGS reaction was first proposed by Dong and Lin (Dong and Lin, 2016). The
demonstration showed that CO_2 removal from the system successfully increased WGS
conversion even without a catalyst. Inspired from the results, an extensive study of
application a thin (~150 μm) asymmetric-structured dual-phase membrane for SRM was
carried out, which was covered in Chapter 4. The experiment results exhibited that the
membrane was able to recover 84% of CO_2 produced and significantly increased the H_2
concentration of the retentate stream from 76% to 88%. However, due to limitations on the

membrane testing module, high pressure experiments were not able to be carried out. When high CO_2 recovery is achieved, the CO_2 partial pressure on the retentate side will be very low and the driving force for permeation will become very limited. Under such a scenario, pressurizing the feed is necessary to further enhance the performance of the membrane reactor.

In this Chapter, a one-dimensional isothermal plug-flow model with a co-current flow configuration was proposed. The reliability of the proposed model was first examined by comparing the model with the experiment data presented in Chapter 4. The performance of the membrane reactor was assessed in terms of CH_4 conversion, H_2 output concentration and H_2 yield under various conditions, including different steam/methane (S/C) ratio, high feed pressure and vacuum permeate side. Furthermore, a dimensionless analysis was also conducted in order to simulate industrial conditions without the consideration of scales, which provides great convenience.

5.2. Experimental

5.2.1. SRM Kinetic Study

SRM and water-gas shift (WGS) reactions were carried out on a built-in-house packed-bed set-up, as shown in **Figure 5.1**. The experiment was conducted for obtaining kinetic parameters of the rate equation for the simulation. A dense alumina tubular membrane was installed in the set-up; hence the set-up was operated as a conventional fixed-bed reactor and there was no permeation when measuring the conversion data. Gas leakage was tested by introducing 100 ml/min nitrogen as feed and 100 ml/min helium as sweep gas at 750 °C. If gas leakage occurred, N_2 should be detected by the gas chromatography (GC, Agilent 7890A) from the permeate side. Only after gas-tightness is confirmed (with N_2 concentration<0.1%), subsequent experiments will be carried out.
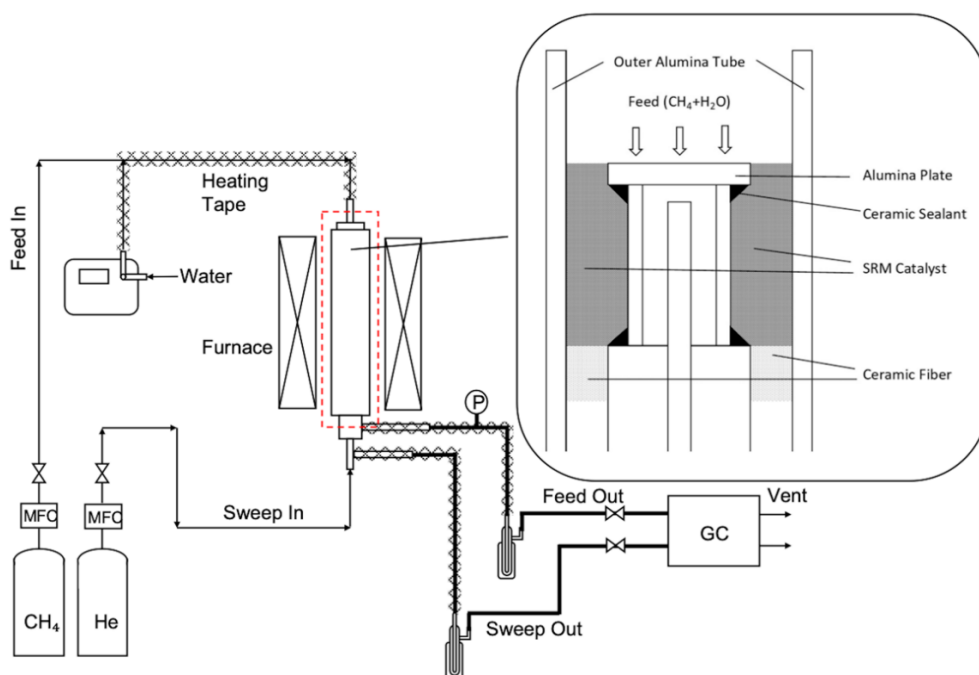
Figure 5.1. *Schematic of tubular membrane reactor for SRM reaction.*

For both SRM and WGS experiments, the steam/carbon (S/C) ratio was controlled at 3. A syringe pump was used to introduce deionized water into a pre-heated stainless-steel pipe to generate steam. 0.2 g of Ni-based catalyst (HiFUEL R110) was mixed with 2 g fused silica (3M Ceradyne) uniformly before loaded in each experiment run. Both the catalyst and fused silica were crushed and sieved to 24-60 mesh grains. The catalyst was activated by 100 ml/min, 5 mol% H_2/95 mol% He mixture at 800 °C for 8 h before performing the reaction. During all the experiment runs, both reaction and permeate sides were kept at atmospheric pressure. Feed and sweep gas were both controlled by mass flow controllers (MKS). The gas composition was analyzed by a GC (Agilent 7890A) with a HayeSep DB 100/120 (AllTech) column. The steam composition was determined by measuring the weight of the condensed water in the cold trap. The flow rate of both feed-out and sweep-out streams were measured by a soap film flow meter. The conversion of species i (X_i, i=CH_4 or CO) was calculated as follows:

$$X_i = \frac{F_i^{feedin} - F_i^{feedout} - F_i^{sweepout}}{F_i^{feedin}} \times 100\% \qquad (5.1)$$

where F_i^{feedin}, $F_i^{feedout}$ and $F_i^{sweepout}$ represent the flow rate of species i in feed-in, feed-out and sweep-out gas stream in the membrane reactor, respectively.

The CO_2 recovery (R_{CO_2}) was calculated as follows:

$$R_{CO_2} = \frac{F_{CO_2}^{sweepout}}{F_{CO_2}^{feedout} + F_{CO_2}^{sweepout}} \times 100\% \qquad (5.2)$$

where $F_{CO_2}^{feedout}$ and $F_{CO_2}^{sweepout}$ are the CO_2 flow rate of feed-out and sweep-out stream, respectively.

The hydrogen yield (Y_{H_2}) was calculated as follows:

$$Y_{H_2} = \frac{F_{H_2}^{feedout}}{F_{CH_4}^{feedin} \times 4} \times 100\% \qquad (5.3)$$

where $F_{H_2}^{feedout}$ is the H$_2$ flow rate of feed-out stream

5.2.2. SRM in Membrane Reactor and CO$_2$ Permeation Experiments

The tubular CO$_2$-permselective membrane was prepared via the centrifugal casting method patented by Lin and coworkers (Dong, Ortiz-Landeros and Lin, 2013; Lin, Ortiz-Landeros and Dong, 2016). The membrane consists of a BYS-SDC (Bi$_{1.5}$Y$_{0.3}$Sm$_{0.2}$O$_{3-\delta}$ and Sm$_{0.2}$Ce$_{0.8}$O$_{2-\delta}$) porous support layer and an SDC-carbonate dense layer with CO$_2$ permeability. The thickness of the CO$_2$-permselective layer is about 100-150 μm. The close-up schematic of the membrane housing module is shown in **Figure 5.2**. The tubular asymmetric dual-phase membranes were about 0.6 cm in I.D. and around 3.5 cm in length, with the effective permeation area of about 7 cm^2. Other components of the membrane testing set-up are as shown in **Figure 5.1**. The SRM experiment was performed with CH$_4$ flow rate = 5 ml/min and S/C = 3 at 700-900 °C. The packing and pretreatment of catalyst are the same as mentioned in section 2.1. Detailed information about the membrane synthesis, characterization and SRM experiment was presented in Chapter 4. In the CO$_2$ permeation experiments, N$_2$/CO$_2$ mixtures of various molar ratio, 50 ml/min were supplied as the feed. The sweep gas was 100 ml/min helium. The measured flux data were used for linear regression to determine the unknown parameters in the flux equation.
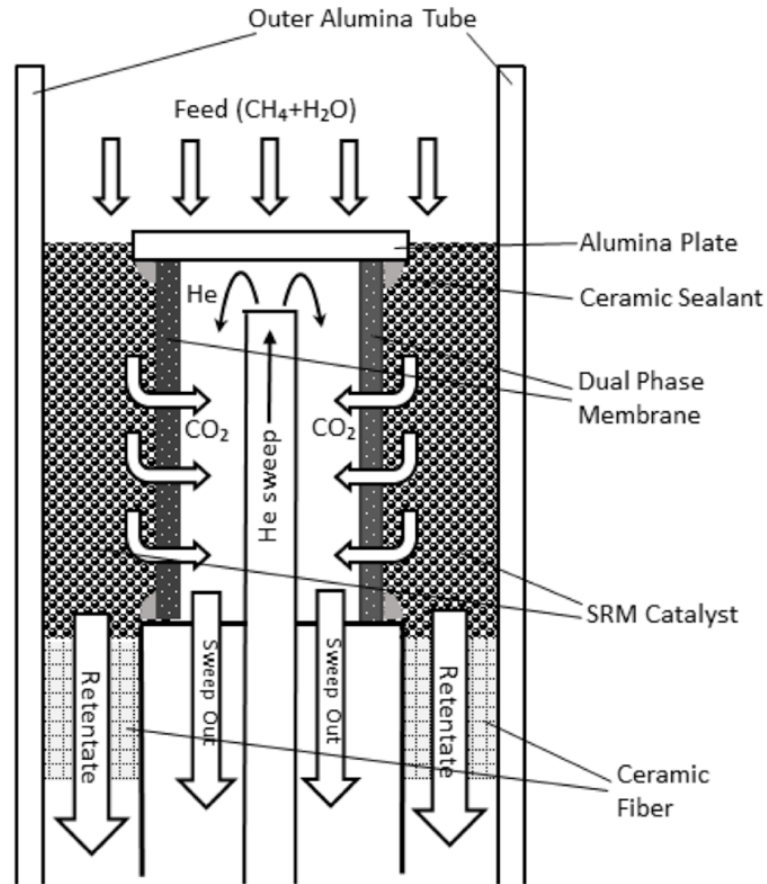
Figure 5.2*. Membrane testing housing used for CO_2 permeation experiments.*

5.3. Model Development

5.3.1. SRM Kinetic Model

The kinetics and reaction mechanisms of SMR performed in the current simulation study are based on the work of Xu and Froment (Xu and Froment, 1989). The three reactions were listed above as reaction 4.A-4.C and the corresponding reaction rate equations are given as:

$$r_1 = \frac{k_1}{P_{H_2}^{2.5}} \left(P_{CH_4}P_{H_2O} - \frac{P_{H_2}^3 P_{CO}}{K_1}\right)/(DEN)^2 \qquad (5.4)$$

$$r_2 = \frac{k_2}{P_{H_2}} \left(P_{CO}P_{H_2O} - \frac{P_{H_2}P_{CO_2}}{K_2}\right)/(DEN)^2 \qquad (5.5)$$

$$r_3 = \frac{k_3}{P_{H_2}^{3.5}} \left(P_{CH_4}P_{H_2O}^2 - \frac{P_{H_2}^4 P_{CO_2}}{K_1 K_2}\right)/(DEN)^2 \qquad (5.6)$$

$$DEN = 1 + K_{CO}P_{CO} + K_{H_2}P_{H_2} + K_{CH_4}P_{CH_4} + K_{H_2O}P_{H_2O}/P_{H_2} \qquad (5.7)$$

where k_j is rate coefficient, K_i is equilibrium constant, K_{CO}, K_{H_2}, K_{CH_4} are the adsorption constants of CO, H_2 and CH_4 respectively, K_{H_2O} is the desorption constant of H_2O and P_i is the partial pressure of gas species. Due to different catalyst was used, and the potential influence of catalyst packing, the rate constants of the reactions might also vary.

In this work, the rate constants and the adsorption constants were obtained by using a nonlinear least square fitting function in Matlab. The empirical method used in this works is referred to work of Abbas et al. (Abbas, Dupont and Mahmud, 2017). The consumption rate of each gas species can be obtained by differentiating the conversion with respect to retention time, i.e., $\frac{dX_i}{d\left(\frac{W}{F_i}\right)}$. The experiment conversion data were fitted with smoothing spline tool in Matlab and $\frac{dX_i}{d\left(\frac{W}{F_i}\right)}$ values were calculated between W/F_i = 0-9 for 100 points (equal for each step). Where W is the total weight of the catalyst and F_i is the methane or CO feed flow rate. For WGS reaction, the following differential equation set was used to solve the kinetic parameters:

$$r_{CO} = \frac{dX_{CO}}{d\left(\frac{W}{F_{CO}}\right)} = r_2 \qquad (5.8)$$

$$r_{H_2O} = -\frac{dX_{H_2O}}{d\left(\frac{W}{F_{CO}}\right)} = -r_2 \qquad (5.9)$$

115

$$r_{H_2} = \frac{dX_{H_2}}{d\left(\frac{W}{F_{CO}}\right)} = r_2 \tag{5.10}$$

$$r_{CO_2} = \frac{dX_{CO_2}}{d\left(\frac{W}{F_{CO}}\right)} = r_2 \tag{5.11}$$

For SRM reaction, the differential equation was set-up as follows:

$$r_{CH_4} = -\frac{dX_{CH_4}}{d\left(\frac{W}{F_{CH_4}}\right)} = -(r_1 + r_3) \tag{5.12}$$

$$r_{H_2O} = -\frac{dX_{H_2O}}{d\left(\frac{W}{F_{CH_4}}\right)} = -(r_1 + r_2 + 2r_3) \tag{5.13}$$

$$r_{H_2} = \frac{dX_{H_2}}{d\left(\frac{W}{F_{CH_4}}\right)} = 3r_1 - r_2 + 4r_3 \tag{5.14}$$

$$r_{CO} = \frac{dX_{CO}}{d\left(\frac{W}{F_{CH_4}}\right)} = r_1 - r_2 \tag{5.15}$$

$$r_{CO_2} = \frac{dX_{CO_2}}{d\left(\frac{W}{F_{CH_4}}\right)} = r_2 + r_3 \tag{5.16}$$

The differential equation sets of Eq. 8-11 and Eq. 12-16 can be solved with known partial pressures from the experiment data and the values of k_j and K_i can be determined.

5.3.2. CO₂ Permeation Flux Equation

A power-function equation for CO_2 permeation flux is based on our previous experiment results on SDC-carbonate membranes research without reaction (Norton, Lu and Lin, 2014; Dong, Wu and Lin, 2018). The equation is used in this model to calculate the in situ CO_2 permeation through the membrane. The flux equation can be expressed as the following form:

$$J_{CO_2} = \frac{RT}{4nF^2L}\alpha[P'^n_{CO_2} - P''^n_{CO_2}] \tag{5.17a}$$

$$\alpha = \phi^m \left(\frac{\varepsilon}{\tau}\right)_s \sigma_i \qquad\qquad (5.17b)$$

where ϕ and m are constants related to oxygen partial pressure to CO_2 partial pressure by either a mass balance on oxygen impurity in the feed or a thermodynamic equilibrium relation for the reaction $CO_2 \leftrightarrow CO + 0.5O_2$. The relationship can be approximated by $P_{O_2} = \phi P_{CO_2}^q$ and mq = n. R is the ideal gas constant; T is temperature; $\left(\frac{\varepsilon}{\tau}\right)_s$ is the ratio of porosity (ε) and tortuosity (τ) of the SDC (thin layer) solid structure; σ_i is the oxygen ion conductivity of the SDC phase (thin layer); L is the thickness of membrane; F is Faraday constant; n is the power of CO_2 partial pressure, P'_{CO_2} and P''_{CO_2} represent the feed side and sweep side CO_2 pressure, respectively. The values of the parameters used in the simulation are given in **Table 5.1**.

Table 5.1. Parameter values used in the simulation

Parameter (unit)	value
R (J/mol/K)	8.314
F (C/mol)	96485
L (μm)	125
Membrane length (cm)	3.5
Membrane area (cm^2)	6.5
Catalyst weight (g)	0.2
Catalyst bed volume (cm^3)	7.96

5.3.3. SRM Membrane Reactor Model

The schematic of the membrane reactor for developing the SRM reaction/separation model is illustrated in **Figure 5.3**. The following assumptions apply to all the simulation in this study: (1) the reactions occur under an isothermal condition in the reactor; (2) flow pattern in the reactor is plug-flow; and (3) the pressure drop long axial direction is negligible. A Matlab program was set up to solve the mass balance differential equations for both sides of the membrane.
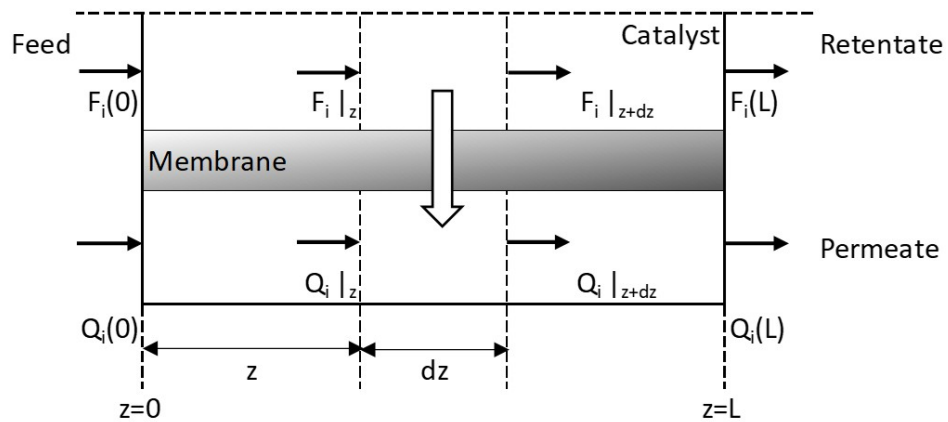
Figure 5.3. *Schematic of the membrane reactor model geometry.*

For mass balance on the reaction side (retentate stream):

$$\frac{dF_i}{dz} = Aw_{cat}\upsilon_i r_i - sJ_i \qquad (5.18)$$

where F_i (i = CH_4, H_2O, CO, CO_2, H_2) is the molar flow rate. υ_i is the stoichiometry of species i in the system. w_{cat} is the weight of catalyst per unit length. A is the cross-sectional area of the catalyst bed. s is the membrane area per unit length. r_i is the formation rate or consumption rate of each species. J_i is the flux of species i permeate through the membrane.

z represents the axial direction of the tubular membrane reactor. Since the membrane will theoretically only allow CO_2 permeation, there will only CO_2 presented in the sweep side (permeate stream), as described as follows:

$$\frac{dQ_{CO_2}}{dz} = sJ_{CO_2} \tag{5.19}$$

where s is the membrane area per unit length and Q_{CO_2} is the CO_2 molar rate on the sweep side.

To facilitate scale-up of obtained results to real conditions, the above equations are also converted into dimensionless form as follows:

$$\frac{df_i}{d\zeta} = \sum_i Da\, v_{i,j} R_j^* - \theta\left(1 - \frac{P_{CO_2}^{\prime n}}{P_{CO_2}^{\prime\prime n}}\right) \tag{5.20}$$

$$\frac{dq_{CO_2}}{d\zeta} = \theta\left(1 - \frac{P_{CO_2}^{\prime n}}{P_{CO_2}^{\prime\prime n}}\right) \tag{5.21}$$

Two dimensionless groups, permeation number (θ) and Damkohler number (Da), were used to achieve the conversion. Other correlations between the dimensional and dimensionless parameters are also given in **Table 5.2**. The permeation number is defined as the ratio of CO_2 permeate flow rate to the methane feed flow rate. It is used to assess the effect of CO_2 removal of the reactor system. The Damkohler number has a physical meaning of the ratio of reaction rate to convective mass transport rate. In our reactor system, it represents the ratio of the theoretical maximum reaction rate to the feed flow rate at the inlet.

Table 5.2. *Correlation between dimensional and dimensionless parameters.*

Permeation number: $\theta = \dfrac{J_{CO_2} S L P_{CO_2}^{\prime n}}{F_{CH_4,0}(P_{CO_2}^{\prime n}-P_{CO_2}^{\prime\prime n})}$

Damkohler number: $Da = \dfrac{R_1^{max} W_{cat} L}{F_{CH_4,0}}$ (W_{cat} = total catalyst weight)

$(R_1^{max} = k_1(\dfrac{P_{CH_4} P_{H_2O}}{P_{H_2}^{2.5}})/(DEN)^2)$ (see Eq. 5.4)

Normalized length: $\zeta = z/L$

Dimensionless reaction rate: $R_j^* = R_j/R_1^{max}$

5.4.   Results and discussions

5.4.1. Reaction Kinetics and CO₂ Permeation Flux

The CH_4 and CO conversions measured with respect to retention time at various temperatures are shown in **Figure 5.4 and 5.5**. The parameter fitting approach is referred to the works of Xu and Froment (Xu and Froment, 1989) and Abbas et al (Abbas, Dupont and Mahmud, 2017). k_2, K_{CO}, K_{H2}, K_{H2O} were calculated via the regression of WGS data. In SRM experiments, the WGS reaction will be very close to equilibrium so that k_2 cannot be meaningfully estimated under such conditions. In addition, K_{CO} and K_{H2} are insignificant due to high temperatures used in SRM experiments. Therefore, only k_1, k_3, K_{CH4}, K_{H2O} are calculated via regression of SRM data. The results are presented in **Table 5.3**. The kinetic parameters calculated at different temperatures can then be correlated by the Arrhenius equation, as shown in **Figure 5.5 and 5.6**. The pre-exponential factors, activation energies for rate constants and enthalpy for adsorption constants are given in **Table 5.4.**

T(°C)	k_1	k_2	k_3	K_{CO}	K_{H2}	K_{CH4}	K_{H2O}
Water-gas shift							
300	–	18.95	–	233.9	0.09190	–	–
325	–	27.49	–	127.7	0.04973	–	–
350	–	49.84	–	71.74	0.03187	–	0.01061
375	–	88.40	–	52.46	0.01559	–	0.02301
Steam reforming of methane							
500	0.03538	–	0.01197	–	–	0.2671	0.1948
550	0.2658	–	0.1257	–	–	0.1834	0.5672
600	1.130	–	0.6480	–	–	0.1211	0.8024
650	4.339	–	2.530	–	–	0.09480	1.866
700	10.28	–	7.539	–	–	0.06870	2.874
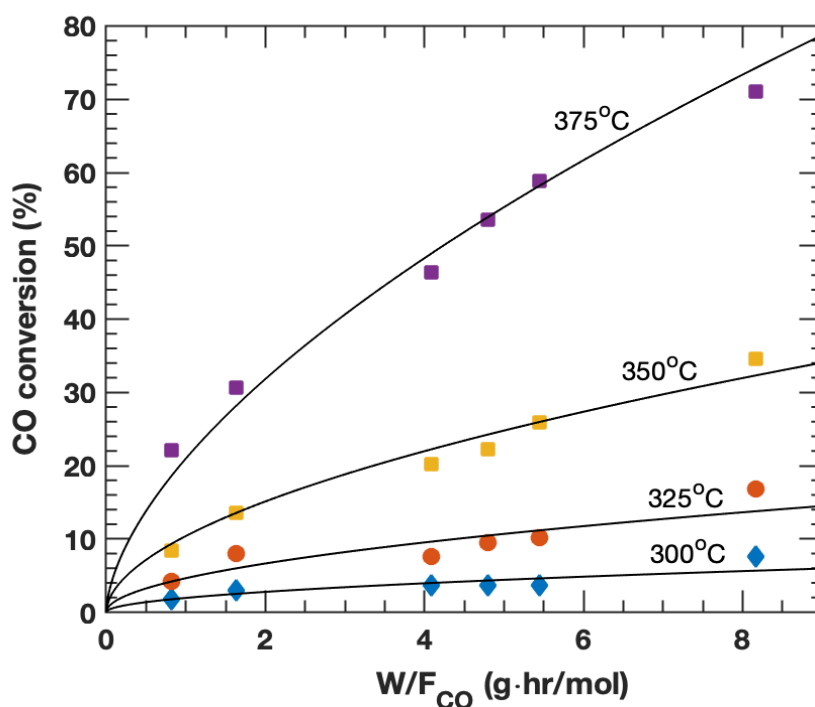
Figure 5.4. *CO conversion versus space time. Markers are the experiment data, while the curves are the simulation result. Feed pressure: 1 atm. S/C = 3.*
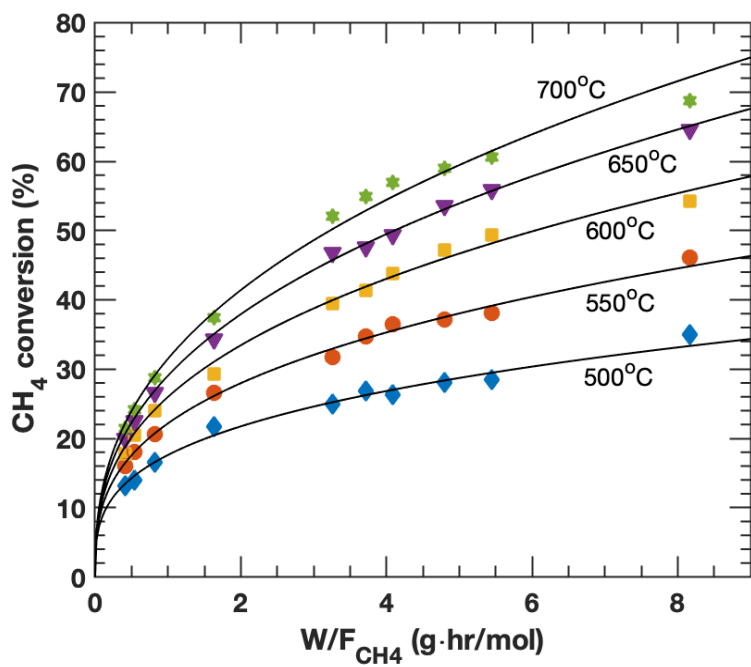
Figure 5.5. *Methane conversion versus space time. Markers are the experiment data, while the curves are the simulation result. Feed pressure: 1 atm. S/C = 3*
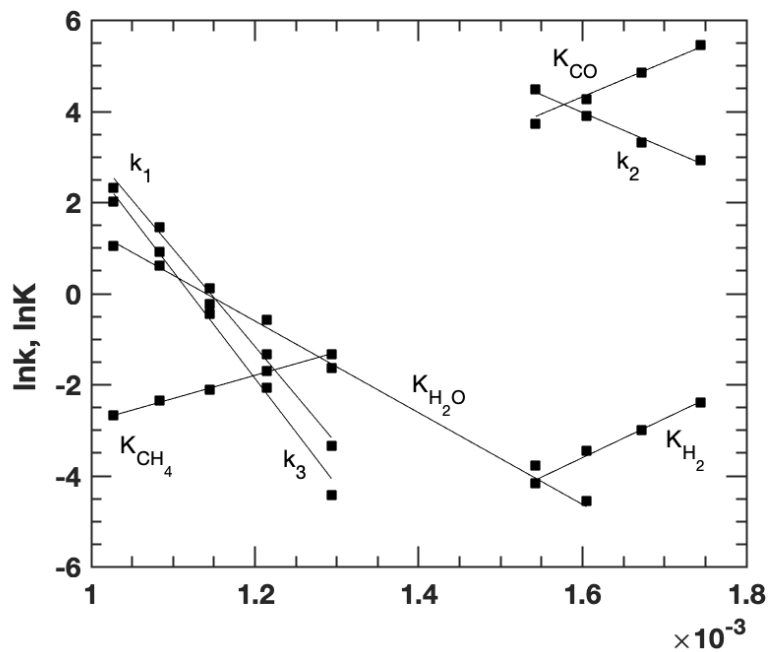
Figure 5.6. *Arrhenius plot of the kinetics constants and adsorption constants in the rate equations.*

122

Table 5.4. Kinetic parameters in the rate equations

Reaction rate constants	$k_j = A_j \exp\left[-E_{aj}/RT\right]$	
k_1 [mol atm$^{0.5}$/(kg-cat h)]	$A_1 = 2.20 \times 10^{14}$	$E_{a1} = 188.9$ kJ/mol
k_2 [mol/(atm kg-cat h)]	$A_2 = 4.29 \times 10^{7}$	$E_{a2} = 66.09$ kJ/mol
k_3 [mol atm$^{0.5}$/(kg-cat h)]	$A_3 = 2.53 \times 10^{14}$	$E_{a3} = 195.9$ kJ/mol

Equilibrium constants

K_1 [atm^2] $= 1.03 \times 10^{10} \exp\left[30.42 - 27106/T\right]$

K_2 [1] $= \exp\left[-4.775 + 4846/T\right]$

Adsorption constants	$K_i = B_i \exp\left[-\Delta H_i/RT\right]$	
K_{CH_4} [atm^{-1}]	$B_{CH_4} = 5.17 \times 10^{-4}$	$\Delta H_{CH_4} = -40.07$ kJ/mol
K_{H_2O} [1]	$B_{H_2O} = 1.75 \times 10^{5}$	$\Delta H_{H_2O} = 87.96$ kJ/mol
K_{CO} [atm^{-1}]	$B_{CO} = 7.78 \times 10^{-5}$	$\Delta H_{CO} = -71.12$ kJ/mol
K_{H_2} [atm^{-1}]	$B_{H_2} = 5.44 \times 10^{-9}$	$\Delta H_{H_2} = -79.99$ kJ/mol

With the experiment data of each component in the SMR and WGS experiments, along with the rate equations presented in Eq. 5.4 to 5.7, the kinetic parameters can be calculated by the nonlinear least squares fitting solver in Matlab. The calculated parameters are given in **Table 5.2** and presented in **Figure 5.3 and 5.4** to show the comparison with experiment data.

By plotting J_{CO_2} as a function of $P_{CO_2}'^n - P_{CO_2}''^n$, n can be calculated by linear fitting and α can be determined from the slope of the fitting line, as shown in **Figure 5.7**. The calculated values of n and α are also given in Table 3. The n values can be approximated by a linear relation as follows:

$$n(T) = 5.769 - 5464/T \qquad (5.22)$$

The correlation of α and temperature can be described by the Arrhenius equation.

The pre-exponential factor and the activation energy can both be obtained by the Arrhenius plot, as shown in **Figure 5.8**. The determined α can substitute into the flux equation (Eq. 5.17) as follows:

$$\alpha = 320.22\exp\left(\frac{-45427}{RT}\right) \qquad (5.23)$$

Table 5.5. *Parameters of the model calculated from fitting experiment data.*

Temperature (°C)	α (S/m)	n
700	1.14	0.5
750	1.57	0.393
800	2.03	0.289
850	2.41	0.201
900	3.03	0.125
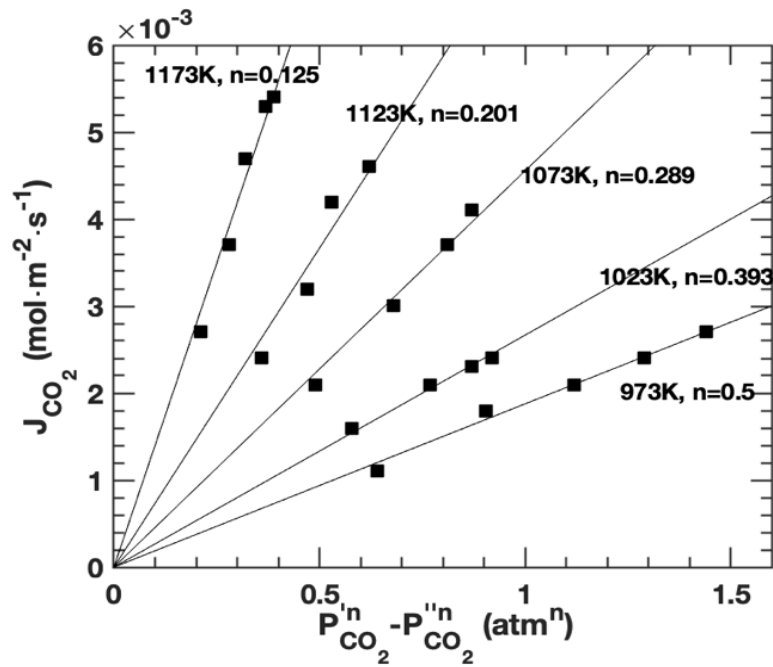
Figure 5.7. *Regression of experiment data for solving corresponding n-values for the flux equation. The x-intercept was set at 0 for all the regression.*
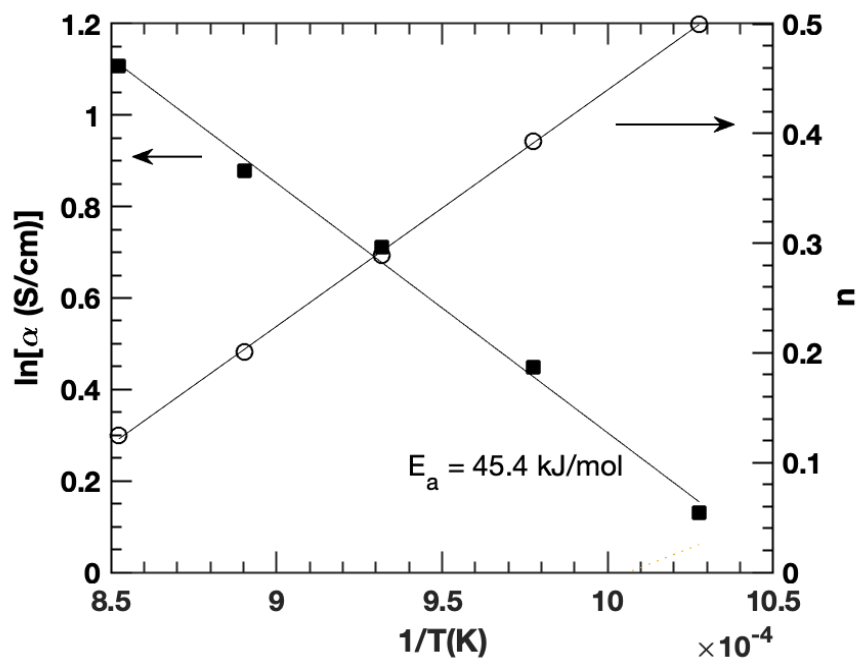
Figure 5.8*. Arrhenius plot of lnα and the temperature dependence of n.*

5.4.2. Reactor Model Validity

The reliability of the model is validated by comparing the output results with experiment data presented in Chapter 4. As presented in **Figure 5.9**, the simulation output suggests the methane conversion should reach equilibrium level for both membrane and fixed-bed reactors. Despite not reaching equilibrium, the conversion measured in the two reactor set-ups is very close. The lower conversion may be resulted from packing or other errors such as flow rate and steam ratio control.

For CO_2 flux and recovery, the model output values are mostly lower than experiment values, as shown in **Figure 5.10**. However, the trend with respect to

temperature generally agrees with experiment data well. The same high agreement is also displayed in H_2 and CO concentration data, as shown in **Figure 5.11 and 5.12**.

As the model shows good reliability, it was also be used to simulate industrial conditions for which the experiment set-up used was not able to work. Hydrogen output concentration with pressurized feed is one of the main interests of this study. As shown in Figure 11, when the feed pressure is 5 atm, the hydrogen concentration can be further increased to about 95%. However, using pressure to 30 atm have almost no effect on a further increase of the output H_2 concentration. The reason can be explained by the rate equation. As Eq. 5.4 and 5.6 show, the negative term will become very large when H_2 concentration is high due to the high power of P_{H2}, and the forward reaction rate will become very slow and reach equilibrium.

Moreover, when CO_2 recovery is high (indicated in **Figure 5.9**), the CO_2 pressure gradient across the membrane will be too low to provide enough CO_2 removal to facilitate the reaction. It will be unrealistic to supply an extremely high sweep gas flow rate to lower the CO_2 concentration at the permeate side. Therefore, a better approach is to apply vacuum at the permeate side to create a larger CO_2 permeation driving force. As presented in **Figure 5.11**, the H_2 concentration in the retentate can reach over 99% when the feed is pressurized to 5 atm and 10^{-3} atm is applied to the sweep side. The result suggests vacuum sweep is more effective than using very high feed pressure (~30 atm) in terms of increasing output H_2 concentration. On the other hand, pressurizing feed is also very effective in reducing CO concentration, which implies facilitated WGS reaction, as shown in **Figure 5.12**. Since the CO concentration in the retentate can be reduced to a very low level when high pressure is used, the effect of sweep side vacuum is not obvious compared with pressurizing feed.
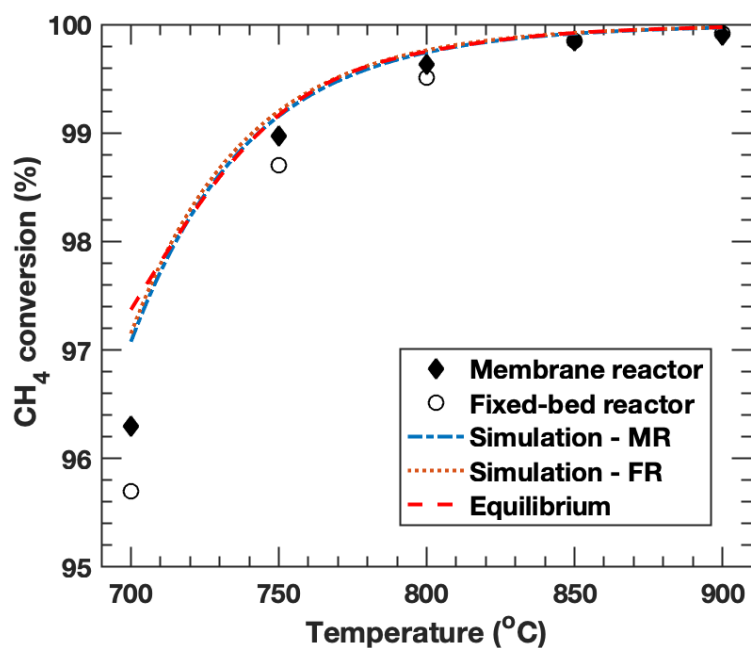
Figure 5.9. *CH₄ conversion comparison between experiment data and simulation results at 700-900 °C. Conditions: sweep: He = 200 ml/min; feed: CH₄ = 5 ml/min; S/C = 3; both sides of the membrane were at 1 atm.*
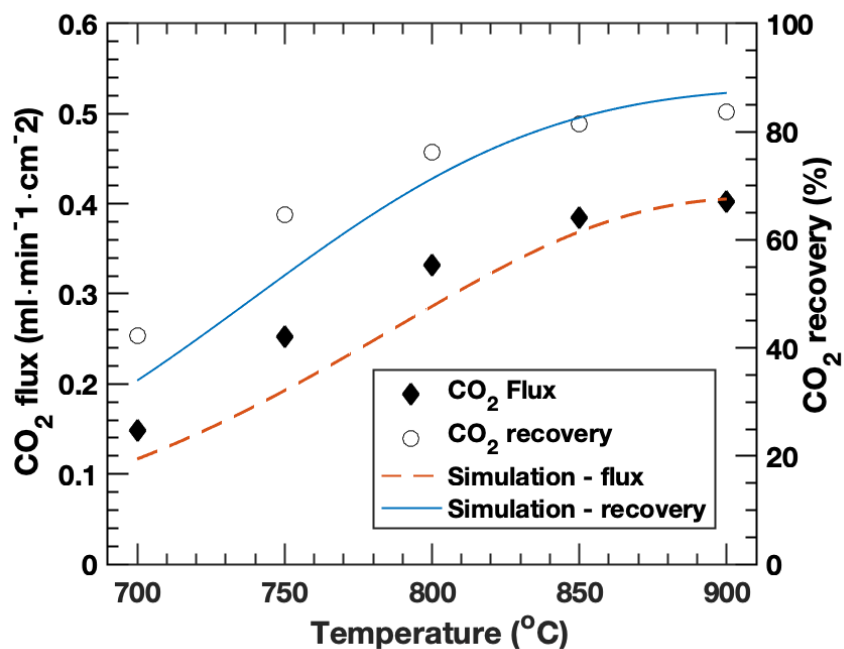
Figure 5.10. *Comparison of CO₂ flux and recovery between experiment results and model output at 700-900 °C. Conditions: sweep: He = 200 ml/min; feed: CH₄ = 5 ml/min; S/C = 3; both sides of the membrane were at 1 atm.*

127
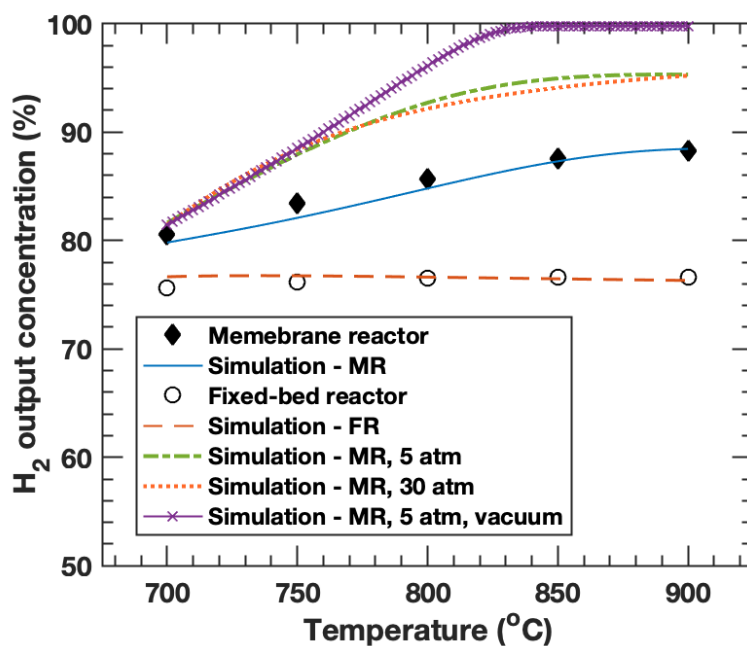
Figure 5.11. *Simulation results of H₂ output concentration with various feed pressure. Conditions: He = 200 ml/min; feed: CH₄ = 5 ml/min; S/C = 3; both sides of the membrane were at 1 atm. Experiment data are also presented for reference.*
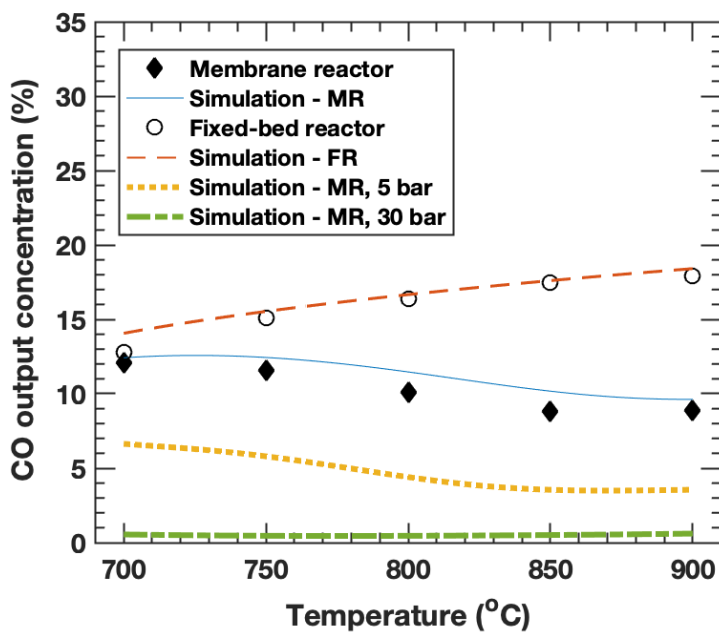
Figure 5.12. *Simulation results of CO output concentration with various feed pressure. Conditions: He = 200 ml/min; feed: CH₄ = 5 ml/min; S/C = 3; both sides of the membrane were at 1 atm. Experiment data are also presented for reference.*

128

5.4.3. Parametric Study

Two dimensionless groups, Damkohler number (Da) and permeation number (θ), were introduced to the equations for the parametric analysis. Since θ is a representation of the permeability of the membrane, the value of θ would change along with temperature. **Figure 5.13** shows the temperature dependence of θ. As the data indicate, the value of θ falls in the range of 0.06 to 7 in the current system when S/C = 3. The effect of S/C ratio is presented in **Figure 5.14**. The data suggest that excess steam has a significant effect on CH_4 conversion, H_2 concentration and H_2 yield. However, the influence of excess steam diminishes when S/C > 3. It is also noteworthy that when S/C > 3, the methane conversion from the membrane reactor start to decrease. This is because the H_2 concentration at such a condition is very high and the forward reaction rate will be slow.
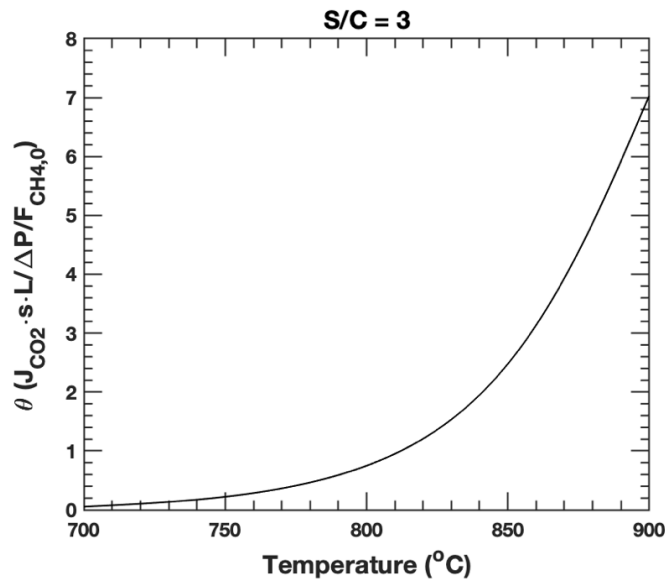
Figure 5.13. *Permeation number (θ) versus temperature (700-900 °C). S/C = 3. Da ~ 2×10^3.*
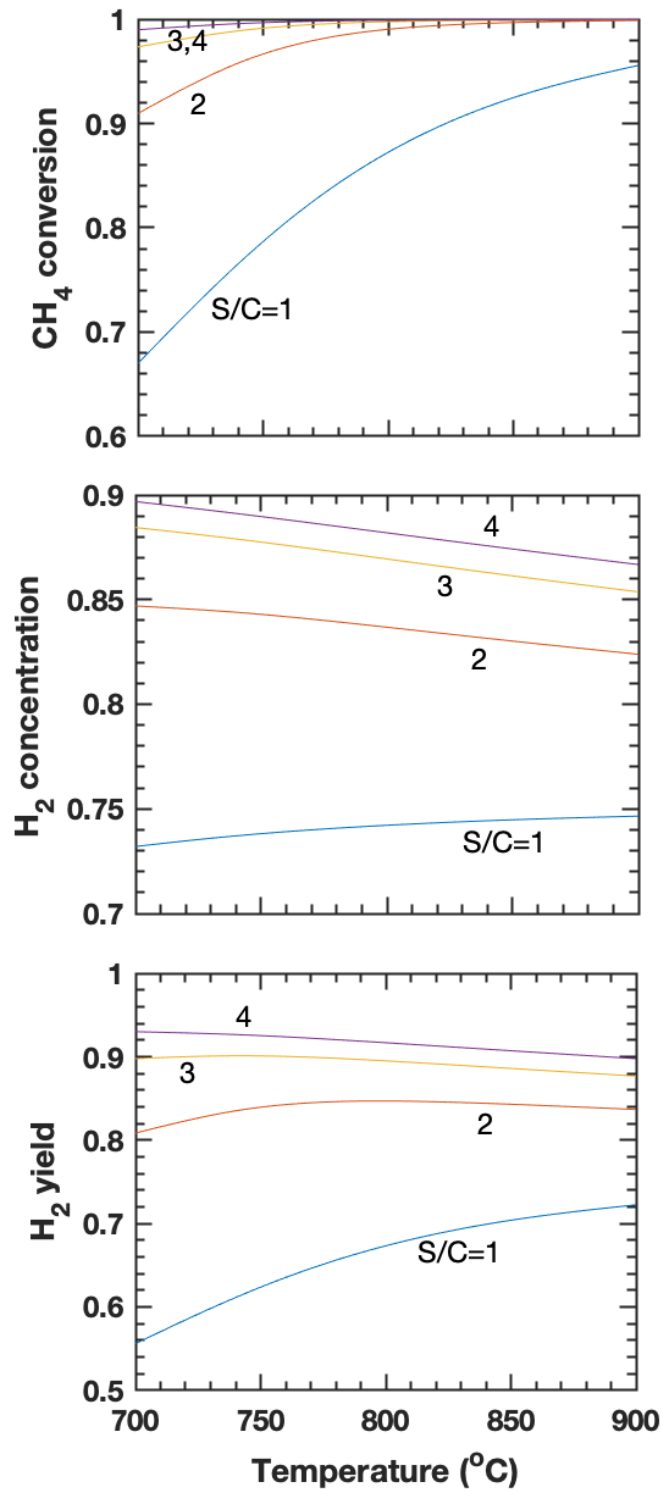
Figure 5.14*. Simulation results of CH₄ conversion, H₂ concentration and H₂ yield with S/C = 1-4. Conditions: feed: 1atm; sweep: 1 atm; feed/sweep = 1/20.*

Figure 5.15 presents the model output results for CH_4 conversion, H_2 output concentration and H_2 yield with various feed pressure. The CH_4 conversion data with P_{feed} = 1 atm suggest that the reaction reaches equilibrium when $Da > 1000$ under atmospheric conditions. Therefore, we can assume instantaneous reaction when $Da = 10000$. As the results indicate, the permeation has almost no effect on all the three items when Da is low (low reaction rate). The permeation will only affect the performance of this type of membrane reactor when the reaction rate is high enough, especially close to equilibrium. When the feed pressure is increased, the output H_2 concentration will also increase. However, in both the cases of 15 atm and 30 atm, the hydrogen concentration reaches a limit of around 95% even when the permeation number is very large (~10). These results indicate that the performance of the membrane reactor is restricted by the working condition instead of the permeability of the membrane. Moreover, the H_2 yield also decreases when increasing feed pressure, which is consistent with the decreasing trend of CH_4 conversion with respect to increasing feed pressure.
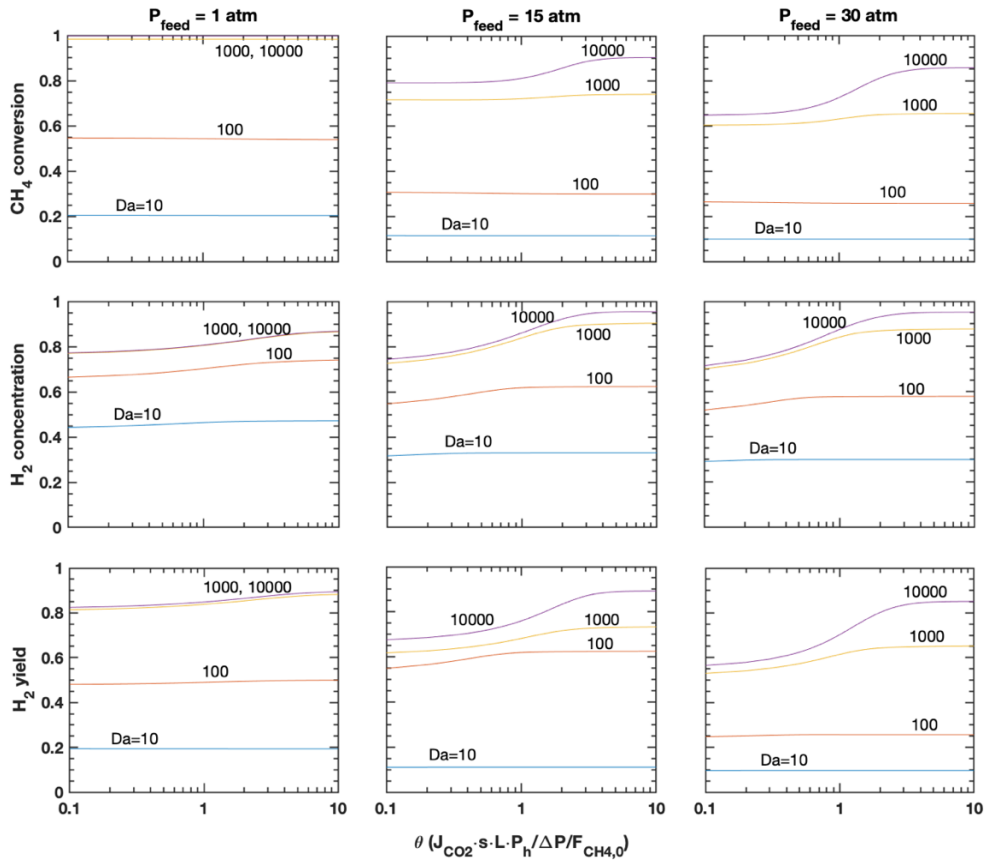
Figure 5.15. *Effect of Damkohler number (Da) and permeation number (θ) on CH_4 conversion, H_2 concentration and H_2 yield with feed pressure = 1, 15, 30 atm. Feed/sweep = 1/20. S/C = 3.*

The concentration profiles of the reactive species also agree well with the explanation above. As presented in **Figure 5.16**, when θ > 5, the concentration of all three species levels off to an equilibrium composition, which indicates that the reaction is close to equilibrium in the first 3/4 of the reactor. It is noteworthy that only in **Figure 5.16** all the concentration is calculated with steam, while all other figures are presenting dry concentration. The equilibrium cannot be broken with only increasing the membrane permeability (θ). On the contrary, as already discussed in the last section, applying vacuum at the permeate side is much more effective in process intensification when high purity H_2

132

is desired. As shown in **Figure 5.17**, with only moderate feed pressure, the CH_4 conversion, H_2 concentration and yield can all reach beyond the equilibrium limitation to over 99% with only moderate feed pressure, the CH_4 conversion, H_2 concentration and yield can all reach beyond the equilibrium limitation to over 99% with $\theta{\sim}3$.
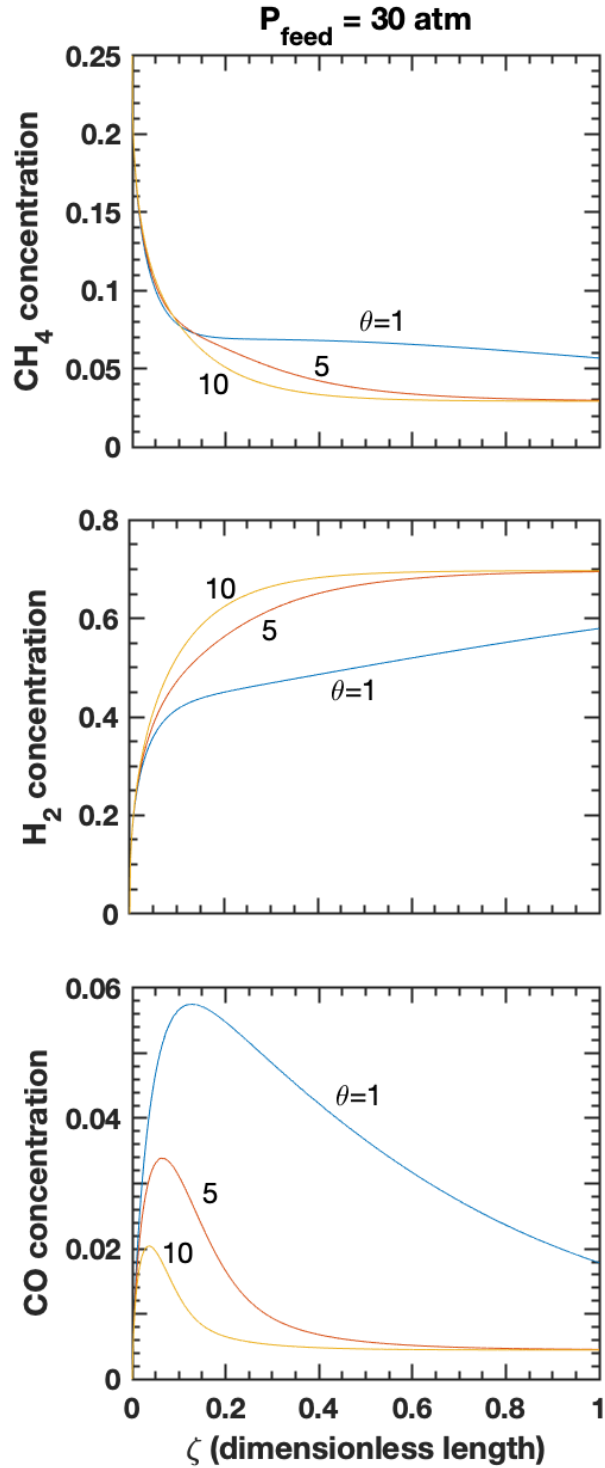
Figure 5.16. *The effect of permeation numer on CH₄, H₂, CO concentration profile in the membrane reactor along axial direction. Feed pressure = 30 atm; S/C = 3; Feed/sweep = 20.*
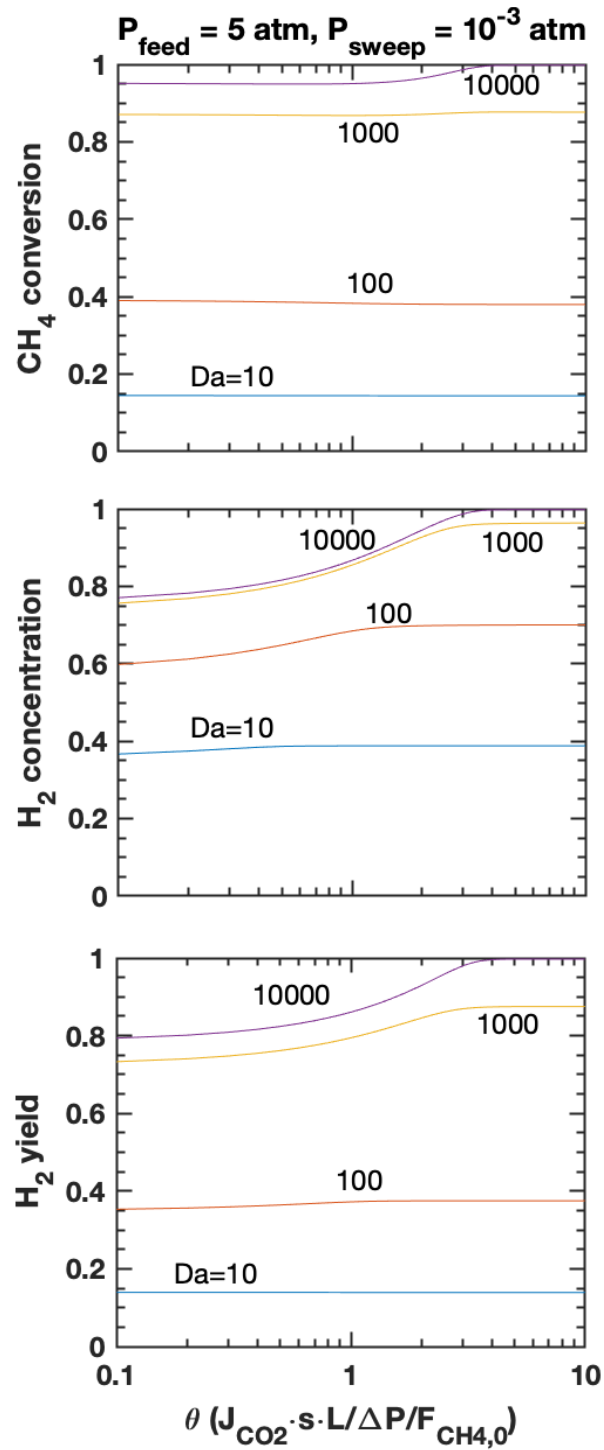
Figure 5.17. *Simulation results of on CH₄ conversion, H₂ concentration and H₂ yield when 5 atm feed and 10⁻³ vacuum sweep are applied. S/C = 3.*

5.5. Conclusions

The model proposed in this work shows high reliability as the simulation output agrees well with the experiment data. Although the simulation results of CO_2 flux and CO_2 recovery are slightly off from experiment data, the general trend with respect to temperature is very similar. This also leads to accurate prediction in H_2 and CO concentration calculations. Applying high feed pressure in the simulation does increase the H_2 output concentration in the retentate stream, however, the concentration would reach a 95% percent limit. Due to the slow reaction rate and low CO_2 driving force, when working at high-pressure conditions, the performance of the membrane reactor will be limited by the working condition instead of the permeability of the membrane. Applying vacuum at the sweep side of the membrane reactor can very effectively promote the retentate H_2 concentration to break through the equilibrium limitation and reach over 99%. The results of the dimensionless parametric analysis suggest that the CO_2 permeability will only be effective when the reaction rate is relatively fast, or the feed flow rate is relatively low.

Notations

F_i = Flow rate of species i in the feed, mol s^{-1}

$F_{i,0}$ = Flow rate of species i in the feed at reactor inlet, mol s^{-1}

f_i = Dimensionless flow rate of species i on the feed side, $f_i = F_i/F_{i,0}$

k_j = Reaction rate constants (j = 1,2,3), defined in Table 4

K_1, K_2 = Equilibrium constants, defined in Table 4

K_i = Adsorption parameters of the catalyst to species I, defined in Table 4

Q_i = Flow rate of species i in the permeate, mol s^{-1}

q_i = Dimensionless flow rate of species i on the sweep side, $q_i = Q_i/F_{i,0}$

R_j = Reaction rate (j = 1,2,3), mol kg-cat^{-1} s^{-1}

R_1^{max} = Maximum forward reaction rate of reaction A, mol kg-cat^{-1} s^{-1}

R_j^* = Dimensionless reaction rate, $R_j^* = R_j/R_1^{max}$

Da = Damkohler number, $Da = \dfrac{R_1^{max} w_{cat} L}{F_{CH_4,0}}$

s = Membrane area per unit length, m^2 m^{-1}

w_{cat} = Catalyst weight per unit length, kg-cat s^{-1}

W_{cat} = Total catalyst weight packed in the reactor, kg-cat

L = Membrane length, m

J_{CO2} = CO$_2$ permeation flux, mol m^{-2} s^{-1}

$P_{CO_2}'^n$ = CO$_2$ partial pressure on the reaction side, atm^n

$P_{CO_2}''^n$ = CO$_2$ partial pressure on the sweep side, atm^n

θ = Permeation number, $\theta = \dfrac{J_{CO_2} S L P_{CO_2}'^n}{F_{CH_4,0}(P_{CO_2}'^n - P_{CO_2}''^n)}$

ϕ = Correlation constant of oxygen partial pressure and CO$_2$ partial pressure, $P_{O_2} = \phi P_{CO_2}^q$, mq = n

$\left(\dfrac{\varepsilon}{\tau}\right)_s$ = Geometric factor of the membrane support, ε is the solid fraction of the support and τ is the solid phase tortuosity, dimensionless

σ_i = Ionic conductivity of the membrane support material, S/m

α = Ionic conduction parameter of the flux equation, $\alpha = \phi^m \left(\dfrac{\varepsilon}{\tau}\right)_s \sigma_i$

z = axial coordinate, m

ζ = dimensionless axial coordinate, $\zeta = z/L$

CHAPTER 6

SUMMARY AND RECOMMENDATIONS

6.1 Research Summary

The research presented in this dissertation started from a fundamental study of oxygen sorption property of MIEC material, then extended to various applications including oxygen sorbent, counter-permeable membrane, and membrane reactor. Specifically, the order-disorder phase transition phenomenon was well documented, although it was not effectively for enhancing oxygen desorption rate. On the other hand, CO_2-O_2 counter-permeation was demonstrated for the first time. The results would broaden the field of application of MIEC membranes. Furthermore, a thin asymmetric membrane was also employed in an SRM membrane reactor for the first time. Finally, a semi-empirical mathematical model was developed based on the experiment results.

In Chapter 2, the oxygen sorption properties of three $La_{1-x}Sr_xCo_{1-y}Fe_yO_{3-\delta}$ (LSCF) perovskite oxides with and without oxygen vacancy disorder-order phase transition were studied. LSCF with lower iron content (LSCF1991) shows the highest sorption capacity in 500-800 °C. The material with disorder-order phase transition during desorption also exhibits an enhanced oxygen desorption rate during the TGA measurement. However, in the fixed-bed desorption process, no obvious enhancement resulted from the disorder-to-order phase transition in oxygen desorption is observed for the LSCF1991 sorbent. The oxygen nonstoichiometry (δ) analysis shows that the oxygen desorption rate of LSCF1991 in the fixed-bed does not significantly increase at the same δ value when the sample is tested in TGA. The LSCF1991 sample in the fixed-bed quenched at 600 °C after 2 h of

desorption shows the occurrence of disorder-to-order phase transition for the perovskite sorbent in the fixed-bed environment. The difference in oxygen desorption rates observed between the fixed-bed process and the TGA experiment is due to much higher oxygen partial pressure in the gas surrounding the sorbents during the fixed-bed oxygen desorption process. In such a condition, the disorder-order phase transition does not occur until the late stage the desorption process.

CO_2 and O_2 permeable ceramic-carbonate dual-phase membranes can be used in membrane reactors for applications such as selective oxidation of hydrocarbons. In Chapter 3, two ceramic-carbonate dual-phase membranes consisting of MIEC perovskite-type ceramics of $Pr_{0.6}Sr_{0.4}Co_{0.2}Fe_{0.8}$ and $SrFe_{0.9}Ta_{0.1}O_{3-\delta}$ were synthesized for studying CO_2 permeation, O_2 permeation and counter-permeation. The geometric factors for the carbonate phase and ceramic phase, obtained from helium permeation and electrical conductivity data, were used to calculate the effective carbonate and oxygen ionic conductivity in the carbonate and ceramic phase. Without counter-permeation, O_2 permeation through the dual-phase membrane is controlled by oxygen ionic conduction in the ceramic phase, whereas CO_2 permeation is determined by the total conductance including effective carbonate and oxygen ionic conductivities in both phases. With CO_2 counter-permeation, the total oxygen permeation flux is higher than that without counter-permeation due to an increase in the driving force for oxygen transport. CO_2 permeation consumes oxygen ions transporting through the membrane, resulting in a lower apparent O_2 flux compared with the O_2-only permeation case. However, O_2 counter-permeation has negligible effect on CO_2 permeation flux for the dual-phase membranes.

Chapter 4 presented a new concept of CO_2-permselective membrane reactor for promoting hydrogen production via SRM with CO_2 capture. The membrane reactor features a ceramic-carbonate dual-phase membrane with a two-layered asymmetric wall structure. Bismuth-yttrium-samarium oxide ($Bi_{1.5}Y_{0.3}Sm_{0.2}O_{3-\delta}$, BYS) is added to the support layer to make it repellant to molten carbonate, leaving only the samarium-doped ceria ($Sm_{0.2}Ce_{0.8}O_{2-\delta}$, SDC) layer to form a thin (~150μm) CO_2-permselective SDC/molten-carbonate dual-phase layer after molten carbonate infiltration. The output product composition from the membrane reactor confirms that in situ CO_2 removal effectively promotes WGS conversion and thus enhances hydrogen yield. At 900 °C with feed pressure at 1 atm, the membrane reactor achieves 90% hydrogen yield with 84% CO_2 recovery, which poses significant improvement when compared with conventional fixed-bed reactor under similar conditions. Analysis of CO_2 permeation activation energy suggests that surface reaction rate might have an effect on CO_2 permeation flux for the thin SDC/molten-carbonate membranes.

In the end, a simulation study of steam reforming of methane (SRM) in a thin dual-phase membrane reactor was conducted in Chapter 5. The proposed model was based on the same membrane reactor presented in Chapter 4 and was in a configuration of a plug-flow, co-current, and isothermal membrane reactor. The simulation results were compared with the experiment data for validation. The comparison shows that the model has high reliability. A dimensionless analysis was also conducted in order to simulate real conditions without the restriction of scales. Two dimensionless groups, permeation number (θ) and Damkohler number (Da) were used as indicators of membrane permeability and reaction rate, respectively. The analysis shows that the membrane permeability only has a

significant effect on CH_4 conversion and retentate composition when the reaction rate is relatively fast (Da > 1000). The effects of pressurized feed and vacuum sweep on CH_4 conversion, H_2 output concentration and H_2 yield are discussed and analyzed. Vacuum sweep is more effective in terms of promoting H_2 concentration than using high feed pressure (30 atm). In the simulation, the H_2 output concentration can reach over 99% when 5 atm feed, 10^{-3} sweep is applied to the system.

6.2 Recommendations

6.2.1 Vacuum desorption for phase transition deployment

The intention of conducting the perovskite sorbents research was to apply this technology to an oxy-fuel combustion process. When the sorption packed-bed is integrated into an oxy-fuel combustion system, the flue gas from the combustion chamber will be recirculated to the sorption bed to perform desorption and create an oxygen-rich stream. With that in mind, a sweep gas was used in the desorption process. This operation is not able to create a low oxygen partial pressure environment around the sorbent unless the very high sweep gas flow rate is used. However, in doing so, the oxygen will be much diluted and the oxy-fuel combustion is not effective. Instead of using a sweep gas to perform desorption, a vacuum sweep is an alternative that worth investigation. The information about oxygen desorption rates in different vacuum condition can be very useful for future PSA process design. Recently, Miura et al. (Miura, Ikeda and Tsuchida, 2016) demonstrated vacuum desorption with $Sr_{1-x}Ca_xFeO_{3-\delta}$ sorbents. Despite having higher oxygen sorption capacity than LSCF1991, the desorption rate is still rather low. It would

141

be very interesting to see how the desorption behavior of LSCF1991 will be with vacuum desorption.

6.2.2 Autothermal Methane Reforming (AMR) membrane reactor and modeling study

The study presented in Chapter 3 covers the first investigation of CO_2/O_2 counter-permeation. Based on the information on hand, the author would recommend the future researchers to move forward to apply this membrane technology to an AMR reactor. With the addition of oxygen, it is expected that AMR will have higher methane conversion than SRM at lower temperatures. It is beneficial to run the reactor at lower temperature as this would reduce energy and maintenance cost. However, at lower temperatures, the ionic mobility is limited and the membrane permeability will be significantly hindered. Therefore, the challenge will be how to synthesize thin membrane with desirable permeability at lower temperature. Moreover, compared with SRM, AMR is not a very mature technology. The information about the reaction selectivity of H_2/CO or H_2/CO_2 will be very valuable from an AMR membrane reactor study.

The same principle of developing an SRM membrane reactor model can be applied to AMR membrane reactors as well. Therefore, the author also recommends future researchers to carry out a modeling study for AMR membrane reactor. Compared with SRM, AMR is more complicated and more difficult to control as more gas components are involved. Therefore, a reliable model can be essential for AMR reactor design and scale-up.

REFERENCES

Abbas, S. Z., Dupont, V. and Mahmud, T. (2017) 'Kinetics study and modelling of steam methane reforming process over a NiO/Al$_2$O$_3$ catalyst in an adiabatic packed bed reactor', International Journal of Hydrogen Energy. Elsevier Ltd, 42(5), pp. 2889–2903. doi: 10.1016/j.ijhydene.2016.11.093.

Akamatsu, K. et al. (2011) 'Stable equilibrium shift of methane steam reforming in membrane reactors with hydrogen-selective silica membranes', AIChE Journal, 57(7), pp. 1882–1888. doi: 10.1002/aic.12404.

Akin, F. T. and Lin, Y. S. (2002) 'Selective oxidation of ethane to ethylene in a dense tubular membrane reactor', Journal of Membrane Science, 209(2), pp. 457–467. doi: 10.1016/S0376-7388(02)00363-0.

Akin, F. T., Lin, Y. S. and Zeng, Y. (2001) 'Comparative study on oxygen permeation and oxidative coupling of methane on disk-shaped and tubular dense ceramic membrane reactors', Industrial and Engineering Chemistry Research, 40, pp. 5908–5916. doi: 10.1021/ie0105425.

Anderson, M. and Lin, Y. S. (2006) 'Synthesis and characterization of a ceramic-carbonate dual-phase membrane for carbon dioxide separation', in 9th Int. Conf. on Inorganic Membranes, pp. 678–681. doi: 10.1016/j.memsci.2013.05.046.

Anderson, M. and Lin, Y. S. (2010) 'Carbonate-ceramic dual-phase membrane for carbon dioxide separation', Journal of Membrane Science, 357(1–2), pp. 122–129. doi: 10.1016/j.memsci.2010.04.009.

Anheden, M., Yan, J. and De Smedt, G. (2005) 'Denitrogenation (or oxyfuel concepts)', Oil and Gas Science and Technology, 60(3), pp. 485–495. doi: 10.2516/ogst:2005030.

Anzelmo, B., Wilcox, J. and Liguori, S. (2017) 'Natural gas steam reforming reaction at low temperature and pressure conditions for hydrogen production via Pd/PSS membrane reactor', Journal of Membrane Science, 522, pp. 343–350. doi: 10.1016/j.memsci.2016.09.029.

Armstrong, P. A. (2015) Development of ITM oxygen technology for integration in IGCC and other advanced power generation. Available at: https://www.osti.gov/biblio/1224800.

Arnold, M., Wang, H. and Feldhoff, A. (2007) 'Influence of CO$_2$ on the oxygen permeation performance and the microstructure of perovskite-type (Ba$_{0.5}$Sr$_{0.5}$)(Co$_{0.8}$Fe$_{0.2}$)O$_{3-\delta}$ membranes', Journal of Membrane Science, 293(1–2), pp. 44–52. doi: 10.1016/j.memsci.2007.01.032.

Auvil, S., Schork, J. and Srinivasan, R. (1993) 'US Patent 5,240,474'.

Baksh, M. S. A., Kikkinides, E. S. and Yang, R. T. (1992) 'Lithium Type X Zeolite as a Superior Sorbent for Air Separation', Separation Science and Technology, 27(3), pp. 277–294. doi: 10.1080/01496399208018880.

Balachandran, U. et al. (1995) 'Dense ceramic membranes for partial oxidation of methane to syngas', Applied Catalysis A, General, 133(1), pp. 19–29. doi: 10.1016/0926-860X(95)00159-X.

Balachandran, U. et al. (1997) 'Ceramic membrane reactor for converting methane to syngas', Catalysis Today, 36(3), pp. 265–272. doi: 10.1016/S0920-5861(96)00229-5.

Barbieri, G. et al. (2001) 'Conversion-temperature diagram for a palladium membrane reactor. Analysis of an endothermic reaction: Methane steam reforming', Industrial and Engineering Chemistry Research, 40(9), pp. 2017–2026. doi: 10.1021/ie0006211.

Battersby, S. et al. (2009) 'Performance of cobalt silica membranes in gas mixture separation', Journal of Membrane Science, 329(1–2), pp. 91–98. doi: 10.1016/j.memsci.2008.12.051.

Baumann, S. et al. (2011) 'Ultrahigh oxygen permeation flux through supported $Ba_{0.5}Sr_{0.5}Co_{0.8}Fe_{0.2}O_{3-\delta}$ membranes', Journal of Membrane Science. Elsevier B.V., 377(1–2), pp. 198–205. doi: 10.1016/j.memsci.2011.04.050.

Beér, J. M. (2007) 'High efficiency electric power generation: The environmental role', Progress in Energy and Combustion Science, 33(2), pp. 107–134. doi: 10.1016/j.pecs.2006.08.002.

Bouwmeester, H. J. M. et al. (1992) 'Oxygen semipermeability of erbia-stabilized bismuth oxide', Solid State Ionics, 53–56, pp. 460–468. doi: 10.1016/0167-2738(92)90416-M.

Bouwmeester, H. J. M., Kruidhof, H. and Burggraaf, A. J. (1994) 'Importance of the surface exchange kinetics as rate limiting step in oxygen permeation through mixed-conducting oxides', Solid State Ionics, 72, pp. 185–194. doi: 10.1016/0167-2738(94)90145-7.

British Petroleum Co. (2019) BP Statistical Review of World Energy Statistical Review of World, BP Statistical Review of World Energy. London: British Petroleum Company. Available at: https://www.bp.com/content/dam/bp/business-sites/en/global/corporate/pdfs/energy-economics/statistical-review/bp-stats-review-2019-full-report.pdf.

Brunetti, A. et al. (2007) 'A porous stainless-steel supported silica membrane for WGS reaction in a catalytic membrane reactor', Chemical Engineering Science, 62(18–20), pp. 5621–5626. doi: 10.1016/j.ces.2007.01.054.

Bryden, K. J. and Ying, J. Y. (1995) 'Nanostructured palladium membrane synthesis by magnetron sputtering', Materials Science and Engineering A, 204(1–2), pp. 140–145. doi: 10.1016/0921-5093(95)09950-6.

Cabrera, A. and Armor, J. (1991) 'US Patent 5,071,450'. doi: 10.1016/0375-6505(85)90011-2.

Cales, B. and Baumard, J. F. (1982) 'Oxygen semipermeability and electronic conductivity in calcia-stabilized zirconia', Journal of Materials Science, 17, pp. 3243–3248. doi: 10.1007/BF01203490.

Caro, J. and Noack, M. (2008) 'Zeolite membranes - Recent developments and progress', Microporous and Mesoporous Materials, 115(3), pp. 215–233. doi: 10.1016/j.micromeso.2008.03.008.

Chao, C. C. (1989) 'US Patent 4,859,217'.

Chen, T. et al. (2019) 'A novel study of sulfur-resistance for CO_2 separation through asymmetric ceramic-carbonate dual-phase membrane at high temperature', Journal of Membrane Science. Elsevier B.V., 581, pp. 72–81. doi: 10.1016/j.memsci.2019.03.021.

Chong, K. C. et al. (2016) 'Recent progress of oxygen/nitrogen separation using membrane technology', Journal of Engineering Science and Technology, 11(7), pp. 1016–1030.

Chung, S. J. et al. (2005) 'Dual-phase metal-carbonate membrane for high-temperature carbon dioxide separation', Industrial and Engineering Chemistry Research, 44(21), pp. 7999–8006. doi: 10.1021/ie0503141.

Damen, K. et al. (2006) 'A comparison of electricity and hydrogen production systems with CO_2 capture and storage. Part A: Review and selection of promising conversion and capture technologies', Progress in Energy and Combustion Science, 32(2), pp. 215–246. doi: 10.1016/j.pecs.2005.11.005.

Deng, S. (2006) 'Sorbent Technology', Encyclopedia of Chemical Processing, pp. 2825–2845. doi: 10.1081/E-ECHP-120007963.

Descamps, C., Bouallou, C. and Kanniche, M. (2008) 'Efficiency of an Integrated

Gasification Combined Cycle (IGCC) power plant including CO_2 removal', Energy, 33(6), pp. 874–881. doi: 10.1016/j.energy.2007.07.013.

Dincer, I. and Acar, C. (2014) 'Review and evaluation of hydrogen production methods for better sustainability', International Journal of Hydrogen Energy. Elsevier Ltd, 40(34), pp. 11094–11111. doi: 10.1016/j.ijhydene.2014.12.035.

Dolan, M. D. et al. (2006) 'Composition and operation of hydrogen-selective amorphous alloy membranes', Journal of Membrane Science, 285(1–2), pp. 30–55. doi: 10.1016/j.memsci.2006.09.014.

Dong, H. et al. (2001) 'Investigation on POM reaction in a new perovskite membrane reactor', Catalysis Today, 67, pp. 3–13. doi: 10.1016/S0920-5861(01)00277-2.

Dong, X. et al. (2009) 'CO_2-tolerant mixed conducting oxide for catalytic membrane reactor', Journal of Membrane Science, 340(1–2), pp. 141–147. doi: 10.1016/j.memsci.2009.05.023.

Dong, X. and Lin, Y. S. (2016) 'Catalyst-free ceramic-carbonate dual phase membrane reactor for hydrogen production from gasifier syngas', Journal of Membrane Science, 520, pp. 907–913. doi: 10.1016/j.memsci.2016.08.036.

Dong, X., Ortiz-Landeros, J. and Lin, Y. S. (2013) 'An asymmetric tubular ceramic-carbonate dual phase membrane for high temperature CO_2 separation', Chemical Communications, 49, pp. 9654–9656. doi: 10.1039/c3cc45949g.

Dong, X., Wu, H.-C. and Lin, Y. S. (2018) 'CO_2 permeation through asymmetric thin tubular ceramic-carbonate dual-phase membranes', Journal of Membrane Science, 564, pp. 73–81. doi: 10.1016/j.memsci.2018.07.012.

El-Maghrabi, H. H. et al. (2018) 'Synthesis of mesoporous core-shell $CdS@TiO_2$ (0D and 1D) photocatalysts for solar-driven hydrogen fuel production', Journal of Photochemistry and Photobiology A: Chemistry. Elsevier B.V., 351, pp. 261–270. doi: 10.1016/j.jphotochem.2017.10.048.

ten Elshof, J. E., Bouwmeester, H. J. M. and Verweij, H. (1995) 'Oxygen transport through $La_{1-x}Sr_xFeO_{3-\delta}$ membranes. I. Permeation in air/He gradients', Solid State Ionics, 81(1–2), pp. 97–109. doi: 10.1016/0167-2738(95)00177-8.

Fabián-Anguiano, J. A. et al. (2019) 'Simultaneous CO_2 and O_2 separation coupled to oxy-dry reforming of CH4 by means of a ceramic-carbonate membrane reactor for in situ syngas production', Chemical Engineering Science, 210. doi: 10.1016/j.ces.2019.115250.

Fang, W. et al. (2015) 'A mixed ionic and electronic conducting dual-phase membrane with high oxygen permeability', Angewandte Chemie - International Edition, 54(16), pp. 4847–4850. doi: 10.1002/anie.201411963.

Fujishima, A. and Honda, K. (1972) 'Electrochemical photolysis of water at a semiconductor electrode', Nature, 238(5358), pp. 37–38. doi: 10.1038/238037a0.

Gallucci, F. et al. (2004) 'Experimental study of the methane steam reforming reaction in a dense Pd/Ag membrane reactor', Industrial & Engineering Chemistry Research, 43(4), pp. 928–933. doi: 10.1021/ie030485a.

Gibbins, J. and Chalmers, H. (2008) 'Carbon capture and storage', Energy Policy, 36(12), pp. 4317–4322. doi: 10.1016/j.enpol.2008.09.058.

Giessler, S. et al. (2003) 'Performance of hydrophobic and hydrophilic silica membrane reactors for the water gas shift reaction', Separation and Purification Technology. doi: 10.1016/S1383-5866(03)00069-8.

Goldschmidt, V. M. (1930) 'Geochemische Verteilungsgesetze und kosmische Häufigkeit der Elemente', Klinische Wochenschrift. doi: 10.1007/BF01733729.

Goodenough, J. B. (2004) 'Electronic and ionic transport properties and other physical aspects of perovskites', Reports on Progress in Physics, 67(11), pp. 1915–1993. doi: 10.1088/0034-4885/67/11/R01.

Grant, R. (1975) 'US Patent 3,884,830', Geothermics. doi: 10.1016/0375-6505(85)90011-2.

Guntuka, S. et al. (2008) 'A- and B-site substituted lanthanum cobaltite perovskite as high temperature oxygen sorbent. 1. thermogravimetric analysis of equilibrium and kinetics', Industrial and Engineering Chemistry Research, 47(1), pp. 154–162. doi: 10.1021/ie070859q.

Guntuka, S., Farooq, S. and Rajendran, A. (2008) 'A- and B-site substituted lanthanum cobaltite perovskite as high temperature oxygen sorbent. 2. column dynamics study', Industrial and Engineering Chemistry Research, 47(1), pp. 163–170. doi: 10.1021/ie070860p.

Hammond, G. P. and Spargo, J. (2014) 'The prospects for coal-fired power plants with carbon capture and storage: A UK perspective', Energy Conversion and Management. Elsevier Ltd, 86, pp. 476–489. doi: 10.1016/j.enconman.2014.05.030.

Han, J. et al. (1997) 'Electrochemical vapor deposition synthesis and oxygen permeation properties of dense zirconia-yttria-ceria membranes', Solid State Ionics, 98(1–2), pp. 63–72. doi: 10.1016/s0167-2738(97)00118-5.

Han, J., Xomeritakis, G. and Lin, Y. S. (1997) 'Oxygen permeation through thin zirconia/yttria membranes prepared by EVD', Solid State Ionics, 93(3–4), pp. 263–272. doi: 10.1016/s0167-2738(96)00528-0.

Harry, K. G. and Johnson, A. (2004) 'A non-destructive technique for measuring ceramic porosity using liquid nitrogen', Journal of Archaeological Science, 31(11), pp. 1567–1575. doi: 10.1016/j.jas.2004.03.020.

He, Y., Zhu, X. and Yang, W. (2011) 'The role of A-site ion nonstoichiometry in the oxygen absorption properties of $Sr_{1+x}Co_{0.8}Fe_{0.2}O_3$ oxides', AIChE Journal, 57(1), pp. 87–95. doi: 10.1002/aic.12246.

Hilpert, K. et al. (2003) 'Defect formation and mechanical stability of perovskites based on $LaCrO_3$ for solid oxide fuel cells (SOFC)', Journal of the European Ceramic Society, 23(16), pp. 3009–3020. doi: 10.1016/S0955-2219(03)00097-9.

Hla, S. S. et al. (2009) 'Kinetics of high-temperature water-gas shift reaction over two iron-based commercial catalysts using simulated coal-derived syngases', Chemical Engineering Journal, 146(1), pp. 148–154. doi: 10.1016/j.cej.2008.09.023.

Huang, J. et al. (2006) 'A high-performance ceramic fuel cell with samarium doped ceria-carbonate composite electrolyte at low temperatures', Electrochemistry Communications. doi: 10.1016/j.elecom.2006.03.016.

Ishigaki, T. et al. (1988) 'Diffusion of oxide ion vacancies in perovskite-type oxides', Journal of Solid State Chemistry, 73(1), pp. 179–187. doi: 10.1016/0022-4596(88)90067-9.

Ishihara, T. et al. (2000) 'Mixed electronic-oxide ionic conductivity and oxygen permeating property of Fe-, Co- or Ni-doped $LaGaO_3$ perovskite oxide', Solid State Ionics, 135(1–4), pp. 631–636. doi: 10.1016/S0167-2738(00)00424-0.

Ishihara, T., Matsuda, H. and Takita, Y. (1994) 'Doped $LaGaO_3$ Perovskite Type Oxide as a New Oxide Ionic Conductor', Journal of the American Chemical Society, 116(9), pp. 3801–3803. doi: 10.1021/ja00088a016.

Jiang, H. et al. (2008) 'Simultaneous production of hydrogen and synthesis gas by combining water splitting with partial oxidation of methane in a hollow-fiber membrane reactor', Angewandte Chemie - International Edition, 47(48), pp. 9341–9344. doi: 10.1002/anie.200803899.

Jiang, X. et al. (2016) 'CO_2-Tolerant $SrFe_{0.8}Nb_{0.2}O_{3-\delta}$-Carbonate Dual-Phase Multichannel Hollow Fiber Membrane for CO2 Capture', Industrial and Engineering Chemistry Research, 55(12), pp. 3300–3307. doi: 10.1021/acs.iecr.5b03036.

Jin, W. et al. (2000) 'Experimental and simulation study on a catalyst packed tubular dense membrane reactor for partial oxidation of methane to syngas', Chemical Engineering Science, 55, pp. 2617–2625. doi: 10.1016/S0009-2509(99)00542-4.

Kanezashi, M. and Lin, Y. S. (2009) 'Gas Permeation and Diffusion Characteristics of MFI-Type Zeolite Membranes at High Temperatures', The Journal of Physical Chemistry C, 113(9), pp. 3767–3774. doi: 10.1021/jp804586q.

Kanniche, M. et al. (2010) 'Pre-combustion, post-combustion and oxy-combustion in thermal power plant for CO_2 capture', Applied Thermal Engineering. Elsevier Ltd, 30(1), pp. 53–62. doi: 10.1016/j.applthermaleng.2009.05.005.

Kennedy, D. (2004) 'The hydrogen solution', Science, 305(5686), p. 917. doi: 10.1126/science.305.5686.917.

Kharton, V. V. et al. (1999) 'Perovskite-type oxides for high-temperature oxygen separation membranes', Journal of Membrane Science, 163(2), pp. 307–317. doi: 10.1016/S0376-7388(99)00172-6.

Kharton, V. V., Marques, F. M. B. and Atkinson, A. (2004) 'Transport properties of solid oxide electrolyte ceramics: A brief review', Solid State Ionics, 174, pp. 135–149. doi: 10.1016/j.ssi.2004.06.015.

Kikuchi, E., Uemiya, S. and Matsuda, T. (1991) 'Hydrogen production from methane steam reforming assisted by use of membrane reactor', Studies in Surface Science and Catalysis, 61, pp. 509–515. doi: 10.1016/S0167-2991(08)60117-2.

Kingery, W. D. et al. (1959) 'Oxygen Ion Mobility in Cubic $Zr_{0.85}Ca_{0.15}O_{1.85}$', Journal of the American Ceramic Society, 42(8), pp. 393–398. doi: 10.1111/j.1151-2916.1959.tb13599.x.

Kiukkola, K. and Wagner, C. (1957) 'Measurements on Galvanic Cells Involving Solid Electrolytes', Journal of the Electrochemical Society, 104(6), pp. 379–387. doi: 10.1149/1.2428586.

Kumpmann, A., Günther, B. and Kunze, H. D. (1993) 'Thermal stability of ultrafine-grained metals and alloys', Materials Science and Engineering A, 168(2), pp. 165–169. doi: 10.1016/0921-5093(93)90722-Q.

Li, J. (2018) OTM Combined Reformer for IGCC Power Systems. Available at: https://www.netl.doe.gov/node/7829.

Li, X., Kerstiens, T. and Markus, T. (2013) 'Oxygen permeability and phase stability of $Ba_{0.5}Sr_{0.5}Co_{0.8}Fe_{0.2}O_{3-\delta}$ perovskite at intermediate temperatures', Journal of Membrane Science, 438, pp. 83–89. doi: 10.1016/j.memsci.2013.03.017.

Li, X., Xiao, G. and Huang, K. (2011) 'Effective ionic conductivity of a novel intermediate-temperature mixed oxide-ion and carbonate-ion conductor', Journal of the Electrochemical Society, 158(2), pp. B225–B232. doi: 10.1149/1.3524477.

Liang, F. et al. (2014) 'A novel CO_2-stable dual phase membrane with high oxygen permeability', Chemical Communications, 50(19), pp. 2451–2454. doi: 10.1039/c3cc47962e.

Lin, H. et al. (2006) 'Plasticization-enhanced hydrogen purification using polymeric membranes', Science, 311(5671), pp. 639–642. doi: 10.1126/science.1118079.

Lin, J. Y. S., Ortiz-Landeros, J. and Dong, X. (2016) 'United States Patent 9,327,231 B2'.

Lin, Y. et al. (2005) 'Direct operation of solid oxide fuel cells with methane fuel', Solid State Ionics, 176(23–24), pp. 1827–1835. doi: 10.1016/j.ssi.2005.05.008.

Lin, Y. M. et al. (2003) 'Effect of incipient removal of hydrogen through palladium membrane on the conversion of methane steam reforming: Experimental and modeling', Catalysis Today, 82(1–4), pp. 127–139. doi: 10.1016/S0920-5861(03)00212-8.

Liu, L. M. et al. (1996) 'A thermogravimetric study of the phase diagram of strontium cobalt iron oxide, $SrCo_{0.8}Fe_{0.2}O_{3-\delta}$', Materials Research Bulletin, 31(1), pp. 29–35. doi: 10.1016/0025-5408(95)00147-6.

Liu, S. et al. (2006) '$Ba_{0.5}Sr_{0.5}Co_{0.8}Fe_{0.2}O_{3-\delta}$ ceramic hollow-fiber membranes for oxygen permeation', AIChE Journal, 52(10), pp. 3452–3461. doi: 10.1002/aic.10966.

Lu, B. and Lin, Y. S. (2013) 'Synthesis and characterization of thin ceramic-carbonate dual-phase membranes for carbon dioxide separation', Journal of Membrane Science, 444, pp. 402–411. doi: 10.1016/j.memsci.2013.05.046.

Lu, B. and Lin, Y. S. (2014) 'Asymmetric thin samarium doped cerium oxide-carbonate dual-phase membrane for carbon dioxide separation', Industrial and Engineering Chemistry Research. doi: 10.1021/ie502094j.

Ma, L. C. et al. (2015) 'Integration of membrane technology into hydrogen production plants with CO_2 capture: An economic performance assessment study', International Journal of Greenhouse Gas Control, 42, pp. 424–438. doi: 10.1016/j.ijggc.2015.08.019.

Ma, L. C. et al. (2017) 'Economic performance evaluation of process system design flexibility options under uncertainty: The case of hydrogen production plants with integrated membrane technology and CO_2 capture', Computers and Chemical Engineering. Elsevier Ltd, 99, pp. 214–229. doi: 10.1016/j.compchemeng.2017.01.020.

Malinauskas, A. P. and Mason, E. A. (1983) Gas transport in porous media: the dusty-gas model. Amsterdam: Elsevier B.V.

Meng, L. and Tsuru, T. (2016) 'Hydrogen production from energy carriers by silica-based catalytic membrane reactors', Catalysis Today, 268, pp. 3–11. doi: 10.1016/j.cattod.2015.11.006.

Merkel, T. C. et al. (2010) 'Power plant post-combustion carbon dioxide capture: An opportunity for membranes', Journal of Membrane Science, 359(1–2), pp. 126–139. doi: 10.1016/j.memsci.2009.10.041.

Miura, N., Ikeda, H. and Tsuchida, A. (2016) '$Sr_{1-x}Ca_xFeO_{3-\delta}$ as a New Oxygen Sorbent for the High-Temperature Pressure-Swing Adsorption Process', Industrial and Engineering Chemistry Research, 55(11), pp. 3091–3096. doi: 10.1021/acs.iecr.5b04579.

Mizusaki, J. et al. (1984) 'Nonstoichiometry of the perovskite-type oxide La1-xSrxCrO3-δ', Solid State Ionics, 12(C), pp. 119–124. doi: 10.1016/0167-2738(84)90138-3.

Mizusaki, J. et al. (1985) 'Nonstoichiometry and defect structure of the perovskite-type oxides $La_{1-x}Sr_xFeO_{3-\delta}$' Journal of Solid State Chemistry, 58(2), pp. 257–266. doi: 10.1016/0022-4596(85)90243-9.

Mizusaki, J. et al. (1989) 'Nonstoichiometry of the perovskite-type oxides $La_{1-x}Sr_xCoO_{3-\delta}$', Journal of Solid State Chemistry, 80(1), pp. 102–111. doi: 10.1016/0022-4596(89)90036-4.

Mizusaki, J. et al. (1991) 'Nonstoichiometry and thermochemical stability of the perovskite-type La1-xSrxMnO3-δ', Solid State Ionics, 49(C), pp. 111–118. doi: 10.1016/0167-2738(91)90076-N.

Mizusaki, J. (1992) 'Nonstoichiometry, diffusion, and electrical properties of perovskite-type oxide electrode materials', Solid State Ionics, 52(1–3), pp. 79–91. doi: 10.1016/0167-2738(92)90093-5.

Mizusaki, J. et al. (1992) 'Nonstoichiometry and Phase Relationship System at High Temperature of the SrFeO ,., -SrFeO ', Journal of Solid State Chemistry, 99, pp. 166–172.

Munzner, H. et al. (1974) 'US Patent 3,801,513'. doi: 10.1145/178951.178972.

Munzner, H. et al. (1976) 'US Patent 3,960,522'.

Nernst, W. (1899) 'About the electrolytic conduction of solid body at very high temperatures', Z. Elektrochem., 6, p. 41.

Norton, T. T., Lu, B. and Lin, Y. S. (2014) 'Carbon dioxide permeation properties and stability of samarium-doped-ceria carbonate dual-phase membranes', Journal of Membrane Science, 467, pp. 244–252. doi: 10.1016/j.memsci.2014.05.026.

Norton, T. T., Ortiz-Landeros, J. and Lin, Y. S. (2014) 'Stability of La-Sr-Co-Fe oxide-carbonate dual-phase membranes for carbon dioxide separation at high temperatures', Industrial and Engineering Chemistry Research, 53(6), pp. 2432–2440. doi: 10.1021/ie4033523.

Ortiz-Landeros, J., Norton, T. and Lin, Y. S. (2013) 'Effects of support pore structure on carbon dioxide permeation of ceramic-carbonate dual-phase membranes', Chemical Engineering Science, 104, pp. 891–898. doi: 10.1016/j.ces.2013.09.027.

Othman, N. H., Wu, Z. and Li, K. (2015) 'An oxygen permeable membrane microreactor with an in-situ deposited $Bi_{1.5}Y_{0.3}Sm_{0.2}O_{3-\delta}$ catalyst for oxidative coupling of methane', Journal of Membrane Science, 488, pp. 182–193. doi: 10.1016/j.memsci.2015.04.027.

Partovi, K. et al. (2015) 'Effect of the B -Site Composition on the Oxygen Permeability and the CO_2 Stability of $Pr_{0.6}Sr_{0.4}Co_xFe_{1-x}O_{3-\delta}$ ($0.0 \leq x \leq 1.0$) Membranes', Chemistry of Materials, 27(8), pp. 2911–2919. doi: 10.1021/acs.chemmater.5b00166.

Patel, K. S. and Sunol, A. K. (2007) 'Modeling and simulation of methane steam reforming in a thermally coupled membrane reactor', International Journal of Hydrogen Energy, 32(4), pp. 2344–2358. doi: 10.1016/j.ijhydene.2007.03.004.

Pehnt, M. and Henkel, J. (2009) 'Life cycle assessment of carbon dioxide capture and storage from lignite power plants', International Journal of Greenhouse Gas Control, 3(1), pp. 49–66. doi: 10.1016/j.ijggc.2008.07.001.

Petric, A., Huang, P. and Tietz, F. (2000) 'Evaluation of La-Sr-Co-Fe-O perovskites for solid oxide fuel cells and gas separation membranes', Solid State Ionics, 135(1–4), pp. 719–725. doi: 10.1016/S0167-2738(00)00394-5.

Qi, X., Lin, Y. S. and Swartz, S. L. (2000) 'Electric transport and oxygen permeation properties of lanthanum cobaltite membranes synthesized by different methods', Industrial and Engineering Chemistry Research, 39(3), pp. 646–653. doi: 10.1021/ie990675e.

Qiu, L. et al. (1995) 'Oxygen permeation studies of $SrCo_{0.8}Fe_{0.2}O_{3-\delta}$', Solid State Ionics, 76(3–4), pp. 321–329. doi: 10.1016/0167-2738(94)00296-5.

Ravkina, O., Klande, T. and Feldhoff, A. (2015) 'Investigation of carbonates in oxygen-transporting membrane ceramics', Journal of Membrane Science, 480, pp. 31–38. doi: 10.1016/j.memsci.2015.01.042.

Rege, S. U. and Yang, R. T. (1997) 'Limits for Air Separation by Adsorption with LiX Zeolite', Industrial and Engineering Chemistry Research, 36(12), pp. 5358–5365. doi: 10.1021/ie9705214.

Roy, R. (1954) 'Multiple Ion Substitution in the Perovskite Lattice', Journal of the American Ceramic Society, 37(12), pp. 581–588. doi: 10.1111/j.1151-2916.1954.tb13992.x.

Rui, Z. et al. (2009) 'Modeling and analysis of carbon dioxide permeation through ceramic-carbonate dual-phase membranes', Journal of Membrane Science, 345(1–2), pp. 110–118. doi: 10.1016/j.memsci.2009.08.034.

Rui, Z. et al. (2012) 'Ionic conducting ceramic and carbonate dual phase membranes for carbon dioxide separation', Journal of Membrane Science, 417–418, pp. 174–182. doi: 10.1016/j.memsci.2012.06.030.

Service, R. F. (2004) 'The hydrogen backlash', Science, 305(5686), pp. 958–961. doi: 10.1126/science.305.5686.958.

Shao, Z. et al. (2000) 'Investigation of the permeation behavior and stability of a $Ba_{0.5}Sr_{0.5}Co_{0.8}Fe_{0.2}O_{3-\delta}$ oxygen membrane', Journal of Membrane Science, 172(1–2), pp. 177–188. doi: 10.1016/s0376-7388(00)00337-9.

Shao, Z. et al. (2001) 'Performance of a mixed-conducting ceramic membrane reactor with high oxygen permeability for methane conversion', Journal of Membrane Science, 183, pp. 181–192. doi: 10.1016/S0376-7388(00)00591-3.

Shao, Z. and Haile, S. M. (2004) 'A high-performance cathode for the next generation of solid-oxide fuel cells', Nature, 431, pp. 170–173. doi: 10.1038/nature02863.

Sherman, S. R. et al. (2012) 'Combustion-assisted CO 2 capture using MECC membranes', Journal of Membrane Science, 401–402, pp. 323–332. doi: 10.1016/j.memsci.2012.02.024.

Sholklapper, T. Z. et al. (2006) 'LSM-infiltrated solid oxide fuel cell cathodes', Electrochemical and Solid-State Letters, 9(8), pp. 376–378. doi: 10.1149/1.2206011.

Singh, D. et al. (2003) 'Techno-economic study of CO_2 capture from an existing coal-fired power plant: MEA scrubbing vs. O_2/CO_2 recycle combustion', Energy Conversion and Management, 44(19), pp. 3073–3091. doi: 10.1016/S0196-8904(03)00040-2.

Sircar, S., Rao, M. B. and Golden, T. C. (1999) 'Fractionation of air by zeolites', Studies in Surface Science and Catalysis, 120A, pp. 395–423. doi: 10.1016/s0167-2991(99)80559-x.

Smith, A. R. and Klosek, J. (2001) 'A review of air separation technologies and their integration with energy conversion processes', Fuel Processing Technology, 70(2), pp. 115–134. doi: 10.1016/S0378-3820(01)00131-X.

Sunarso, J. et al. (2008) 'Mixed ionic-electronic conducting (MIEC) ceramic-based membranes for oxygen separation', Journal of Membrane Science, 320(1–2), pp. 13–41. doi: 10.1016/j.memsci.2008.03.074.

Sunarso, J. et al. (2011) 'High performance BaBiScCo hollow fibre membranes for oxygen transport', Energy and Environmental Science, 4, pp. 2516–2519. doi: 10.1039/c1ee01180d.

Sutt, R. (1986) 'US Patent 4,594,163'.

Takahashi, T., Esaka, T. and Iwahara, H. (1976) 'Electrical conduction in the sintered oxides of the system Bi2O3BaO', Journal of Solid State Chemistry, 16, p. 317. doi: 10.1016/0022-4596(76)90047-5.

Teraoka, Y. et al. (1984) 'Oxygen-Sorptive Properties and Defect Structure of Perovskite-Type Oxides', Chemistry Letters, 13(6), pp. 893–896. doi: 10.1246/cl.1984.893.

Teraoka, Y. et al. (1985) 'OXYGEN-SORPTIVE PROPERTIES AND DEFECT STRUCTURE OF PEROVSKITE-TYPE OXIDES', Chemistry Letters, pp. 1367–1370. doi: 10.1246/cl.1984.893.

Toftegaard, M. B. et al. (2010) 'Oxy-fuel combustion of solid fuels', Progress in Energy and Combustion Science. Elsevier Ltd, 36(5), pp. 581–625. doi: 10.1016/j.pecs.2010.02.001.

Tong, J. et al. (2003) 'Investigation on the structure stability and oxygen permeability of titanium-doped perovskite-type oxides of $BaTi_{0.2}Co_xFe_{0.8-x}O_{3-\delta}$(x=0.2-0.6)', Separation and Purification Technology, 32(1–3), pp. 289–299. doi: 10.1016/S1383-5866(03)00045-5.

Tong, J. et al. (2005) 'Experimental study of steam reforming of methane in a thin (6 μm) Pd-based membrane reactor', Industrial and Engineering Chemistry Research, 44(5), pp. 1454–1465. doi: 10.1021/ie049115s.

Tsai, C.-Y. et al. (1997) 'Dense perovskite membrane reactors for partial oxidation of methane to syngas', AIChE Journal, 43(S11), pp. 2741–2750. doi: 10.1002/aic.690431320.

Tsuru, T. et al. (2004) 'Methane steam reforming by microporous catalytic membrane reactors', AIChE Journal, 50(11), pp. 2794–2805. doi: 10.1002/aic.10215.

United States Environmental Protection Agency (2019) Sources of Greenhouse Gas Emissions. Available at: https://www.epa.gov/ghgemissions/sources-greenhouse-gas-emissions.

Wade, J. L. et al. (2011) 'Composite electrolyte membranes for high temperature CO_2 separation', Journal of Membrane Science, 369(1–2), pp. 20–29. doi: 10.1016/j.memsci.2010.10.053.

Wang, H. et al. (2009) 'Oxygen selective ceramic hollow fiber membranes for partial oxidation of methane', AIChE Journal, 55(10), pp. 2657–2664. doi: 10.1002/aic.11856.

Wang, H., Cong, Y. and Yang, W. (2002) 'Oxygen permeation study in a tubular $Ba_{0.5}Sr_{0.5}Co_{0.8}Fe_{0.2}O_{3-\delta}$ oxygen permeable membrane', Journal of Membrane Science, 210(2), pp. 259–271. doi: 10.1016/S0376-7388(02)00361-7.

Wei, X. and Lin, Y. S. (2008) 'Protonic and electronic conductivities of terbium doped strontium cerates', Solid State Ionics, 178(35–36), pp. 1804–1810. doi: 10.1016/j.ssi.2007.11.022.

Williams, T. C., Shaddix, C. R. and Schefer, R. W. (2008) 'Effect of syngas composition and CO_2-diluted oxygen on performance of a premixed swirl-stabilized combustor', Combustion Science and Technology, 180(1), pp. 64–88. doi: 10.1080/00102200701487061.

Xia, C. et al. (2010) 'Intermediate temperature fuel cell with a doped ceria-carbonate composite electrolyte', Journal of Power Sources. doi: 10.1016/j.jpowsour.2009.11.104.

Xu, J. and Froment, G. F. (1989) 'Methane steam reforming, methanation and water-gas shift: I. Intrinsic kinetics', AIChE Journal, 35(1), pp. 88–96. doi: 10.1002/aic.690350109.

Xu, N. et al. (2012) 'Silver-molten carbonate composite as a new high-flux membrane for electrochemical separation of CO_2 from flue gas', Journal of Membrane Science, 401–402, pp. 190–194. doi: 10.1016/j.memsci.2012.02.001.

Yang, R. T. (1997) Gas Separation by Adsorption Processes. Reprint, Chemical Engineering Science. Reprint. Imperial College Press. doi: 10.1016/0009-2509(88)80096-4.

Yang, Z. H. and Lin, Y. S. (2003) 'High-temperature oxygen sorption in a fixed bed packed with perovskite-type ceramic sorbents', Industrial and Engineering Chemistry Research, 42(19), pp. 4376–4381. doi: 10.1021/ie030313d.

Yang, Z. H. and Lin, Y. S. (2005) 'Synergetic thermal effects for oxygen sorption and order-disorder transition on perovskite-type oxides', Solid State Ionics, 176(1–2), pp. 89–96. doi: 10.1016/j.ssi.2004.06.011.

Yang, Z. and Lin, Y. S. (2002) 'A semi-empirical equation for oxygen nonstoichiometry of perovskite-type ceramics', Solid State Ionics, 150(3–4), pp. 245–254. doi: 10.1016/S0167-2738(02)00524-6.

Yang, Z. and Lin, Y. S. (2003) 'Equilibrium of oxygen sorption on perovskite-type lanthanum cobaltite sorbent', AIChE Journal, 49(3), pp. 793–798. doi: 10.1002/aic.690490323.

Yang, Z., Lin, Y. S. and Zeng, Y. (2002) 'High-temperature sorption process for air separation and oxygen removal', Industrial and Engineering Chemistry Research, 41(11), pp. 2775–2784. doi: 10.1021/ie010736k.

Yi, J., Schroeder, M. and Martin, M. (2013) 'CO_2-tolerant and cobalt-free SrFe0.8Nb 0.2O3-δ perovskite membrane for oxygen separation', Chemistry of Materials, 25(6), pp. 815–817. doi: 10.1021/cm303666v.

Yi, J., Weirich, T. E. and Schroeder, M. (2013) 'CO_2 corrosion and recovery of perovskite-type $BaCo_{1-x-y}Fe_xNb_yO_{3-\delta}$ membranes', Journal of Membrane Science, 437, pp. 49–56. doi: 10.1016/j.memsci.2013.02.049.

Yin, Q., Kniep, J. and Lin, Y. S. (2008) 'High temperature air separation by perovskite-type oxide sorbents-Heat effect minimization', Chemical Engineering Science, 63(24), pp. 5870–5875. doi: 10.1016/j.ces.2008.09.004.

Yin, Q. and Lin, Y. S. (2007) 'Beneficial effect of order-disorder phase transition on oxygen sorption properties of perovskite-type oxides', Solid State Ionics, 178(1–2), pp. 83–89. doi: 10.1016/j.ssi.2006.11.013.

Zeng, P. et al. (2007) 'Significant effects of sintering temperature on the performance of La0.6Sr0.4Co0.2Fe0.8O3-δ oxygen selective membranes', Journal of Membrane Science, 302(1–2), pp. 171–179. doi: 10.1016/j.memsci.2007.06.047.

Zhang, C. et al. (2008) 'The oxidative stream reforming of methane to syngas in a thin tubular mixed-conducting membrane reactor', Journal of Membrane Science, 320(1–2), pp. 401–406. doi: 10.1016/j.memsci.2008.04.022.

Zhang, H. M. et al. (1990) 'Oxygen sorption and catalytic properties of La1-xSrxCo$_{1-y}$Fe$_y$O$_3$ Perovskite-type oxides', Journal of Catalysis, 121(2), pp. 432–440. doi: 10.1016/0021-9517(90)90251-E.

Zhang, L. et al. (2012) 'High CO_2 permeation flux enabled by highly interconnected three-dimensional ionic channels in selective CO_2 separation membranes', Energy and Environmental Science, 5, pp. 8310–8317. doi: 10.1039/c2ee22045h.

Zhu, J. et al. (2015) 'CO_2-tolerant oxygen-permeable perovskite-type membranes with high permeability', Journal of Materials Chemistry A, 3, pp. 22564–22573. doi: 10.1039/c5ta04598c.

Zhuang, S. et al. (2019) 'Perovskite oxide and carbonate composite membrane for carbon dioxide transport', Materials Letters, 236, pp. 329–333. doi: 10.1016/j.matlet.2018.10.135.

Zienius, M. et al. (2017) 'Oxygen ion conductivity in samarium and gadolinium stabilized cerium oxide heterostructures', Solid State Ionics, 302, pp. 138–142. doi: 10.1016/j.ssi.2016.11.025.

Zuo, M. et al. (2014) 'Ionic conducting ceramic-carbonate dual phase hollow fibre membranes for high temperature carbon dioxide separation', Journal of Membrane Science. Elsevier, 458, pp. 58–65. doi: 10.1016/j.memsci.2014.01.047.

APPENDIX A

LIST OF PUBLICATIONS

The preceding chapters are modified versions of papers published or to be submitted for publication:

Chapter 2

Wu, H. C. & Lin, Y. S. (2017). Effects of oxygen vacancy order−disorder phase transition on air separation by perovskite sorbents. *Industrial & Engineering Chemistry Research*, 56(20), 6057–6064.

Chapter 3

Wu, H. C., Nile, G.R. & Lin, Y. S. (2020). Mixed-conducting ceramic-carbonate dual-phase membranes: gas permeation and counter-permeation. *Journal of Membrane Science, revision.*

Chapter 4

Wu, H. C., Rui, Z. & Lin, Y. S. (2020). Hydrogen production with carbon dioxide capture by dual-phase ceramic carbonate membrane reactor via steam reforming of methane. *Journal of Membrane Science, 598*, 117780.

Chapter 5

Wu, H. C. & Lin, Y. S. (2020) A modeling study on CO_2-permselective membrane reactor performing steam reforming of methane. In progress.

APPENDIX B

SYNTHESIS OF PEROVSKITE AND FLUORITE CERAMIC POWDERS VIA

LIQUID CITRIC METHOD

1. In this dissertation, the liquid citric method applied to the synthesis of LSCF-series, $Ce_{0.8}Sm_{0.2}O_{2-\delta}$ (SDC), $B_{1.5}Y_{0.3}Sm_{0.2}O_{3-\delta}$ (BYS) and $Pr_{0.6}Sr_{0.4}Co_{0.2}Fe_{0.8}O_{3-\delta}$ (PSCF) ceramic powders.

2. For LSCF-series materials, the materials used are: $La(NO_3)_3 \cdot 6H_2O$, $Sr(NO_3)_2$, $CO(NO_3)_3 \cdot 6H_2O$, $Fe(NO_3)_3 \cdot 9H_2O$ and citric acid.

3. For SDC, the raw materials used are: $Ce(NO3)3 \cdot 6H2O$, $Sm(NO3)3 \cdot 6H2O$ and citric acid.

4. For BYS, the raw materials used are: $Bi(NO_3)_3 \cdot 5H_2O$, $Y(NO3)3 \cdot 6H2O$, $Sm(NO3)3 \cdot 6H2O$, citric acid and nitric acid.

5. For PSCF, the raw materials used are: $Pr(NO_3)_3 \cdot 6H_2O$, $Sr(NO_3)_2$, $CO(NO_3)_3 \cdot 6H_2O$, $Fe(NO_3)_3 \cdot 9H_2O$ and citric acid.

6. The synthesis starts from weighing the adequate amount of materials. For example, 10 g of $La_{0.1}Sr_{0.9}Co_{0.9}Fe_{0.1}O_{3-\delta}$ (LSCF1991) is equivalent of 0.05 mol of the material. Then the amount of $La(NO_3)_3 \cdot 6H_2O$ needed will be: 0.05×0.1(stoichiometry) $\times$ 433.01(molecular weight) $\div$ 0.999(purity) = 2.167 g. The same principle applies to all the raw materials except citric acid and nitric acid (only for BYS synthesis).

7. For citric acid, 20% of excess is desired to form the metal ion complex in the synthesis process. Use LSCF1991 as an example. When 0.05 mol LSCF1991 is to be made, the amount of citric acid needed will be 0.05(total metal ion mol) $\times$ 1.2(20% excess) $\times$ 192.12(molecular weight) $\div$ 0.995 = 11.585 g

8. Dissolve all the prepared materials in a beaker with deionized water. Generally, a water/solid ratio of 20 is ideal. For example, if the total weight of the solid is 20 g, the amount of water used will be $20 \times 20 = 400$ g.

9. For the synthesis of BYS, 10 wt% of nitric acid (68-70% ACS grade) has to be mixed with water prior to the addition of the solids. For example, if the 90 g of water is used, 10 g of nitric acid has to be added.

10. Heat the solution on a hot plate with continuous agitation (with a magnetic stirbar) at about 100°C (hot plate set point). Keep the solution at this temperature for at least 4 h. Keep the hot plate in a fume hood.

11. Increase the temperature to 200°C to evaporate the excess water. A viscous, gel-like substance should be obtained after all the water being evaporated.

12. Increase the temperature to 400°C to remove the organic content from the citric acid.

13. Grind the resulting powder with a mortar and pestle for 10 min.

14. Calcine the powder in a box furnace. Ramping rate of 2°C/min can be applied to all the materials. The calcination temperature of each material is given in Table A1 as follows:

Table B.1. Calcination temperatures of the ceramics.

Material	Temperature (°C)	Time (h)
LSCF-series	800	8
SDC	550 or 950 (see Chapter 4)	5
BYS	850	5
PSCF	850	8

15. After the calcination, grind the powder for 10 min using a mortar and pestle.

16. Examine the material phase structure by powder X-ray diffraction.

APPENDIX C

SYNTHESIS OF SFT VIA SOLID-STATE REACTION METHOD

1. Weigh stoichiometric amounts of $SrCO_3$, Fe_2O_3 and Ta_2O_5. Refer to Appendix A for the calculation method.

2. Mix the powders by ball-milling in ethanol for 24 h. The power/ball ratio is 50/50 wt%. The level of ethanol should be just enough to cover the powder and the milling balls. The rate of the ball miller is set at 14 (Across International Planetary Ball Mill).

3. Remove the milling balls by a sieve.

4. Place the mixture in the fume hood for drying.

5. After drying, collect the powder mixture in a crucible and calcine the mixture at 1250 °C for 20 h.

6. Grind the powder for 10 min using a mortar and pestle after the calcination.

7. Examine the material phase structure by powder X-ray diffraction.

APPENDIX D

FABRICATION OF DISK MEMBRANES

1. Place the powder in a 2.3 cm diameter die and press the powder using a hydraulic press (Carver 3853-0) to 180 MPa. The weight of PSCF powder can be 2.5 to 3 g. The weight for SFT has be 3 to 3.5 g. If the good quality SFT membrane is very difficult to make if the SFT green body is too thin.

2. Maintain the pressure for 5 min.

3. Release the pressure and carefully detach the membrane green body from the mold.

4. Calcine the powder in a box furnace. Ramping rate of 2°C/min can be applied to both the materials. The calcination temperature of each material is given in Table C.1 as follows:

Table C.1. Sintering temperatures for the disks.

Material	Temperature (°C)	Time (h)
PSCF	1200	10
SCF	1300	20

5. Examine the material phase structure by X-ray diffraction.

APPENDIX E

FIXED-BED SORPTION AND DESORPTION EXPERIMENT

1. Prepare a clean dense alumina tube. In this dissertation, the alumina tube used was 19 in. long and 7/16 in. in I.D.

2. Use the ceramic fiber (from Grainger) to block one side of the tube.

3. Load the fused silica grains (from 3M) into the tube to about the middle point of the length. The packing length can be observed by a strong flashlight. In the packing process, keep taping the alumina tube gently to ensure the packing is tight.

4. Load the weighed sample to the tube assistant tool (small paper or plastic funnel). Generally, 2~3 g of perovskite powder should be sufficient for a 4~5 cm long packed bed.

5. Load the silica grains until the whole tube is filled.

6. Install the fittings and connect the gas lines. The ferrules in the fitting should be graphite or Teflon. Metal fitting is not suitable for a ceramic tube.

7. Start heating to the target temperature in the rate of 2°C/min.

8. Prior to oxygen adsorption, the sorbent should be treated with 10 ml/min helium at the target temperature for at least 4 h. Once finished, the sample is ready for sorption/desorption experiment.

9. The sorption/desorption is carried out by switching the feed between air/helium. The concentration can be measured by the bench-top oxygen analyzer (System Illinois ZR800).

APPENDIX F

STEADY-STATE HELIUM PERMEATION

1. Place the disk membrane in the permeation module. both surfaces of the membrane are pressed against rubber O-ring for gas tightness. The schematic for steady-state set-up is shown in Figure D.1
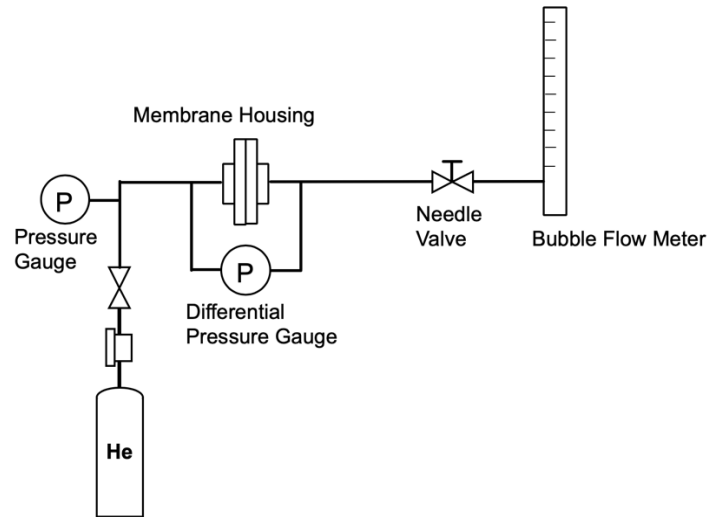
Figure F.1. Schematic of the steady-state helium permeation set-up.

2. Adjust the flow rate from the mass flow controller and the needle valve to set a certain pressure. Once the upstream pressure stops fluctuating, measure the helium flow rate by using the bubble flow meter.

3. Repeat step 2 and collect data for at least 5 different average of cross-membrane pressures.

APPENDIX G

ELECTRICAL CONDUCTIVITY MEASUREMENT OF CERAMIC SAMPLES

1. Grind the disc membrane with 500-grit sandpaper into rectangular shape.

2. Attach silver wires to the bar sample in the configuration shown in Figure G.1. The interval of each wire should be the same.

3. Apply silver ink to the seam between the wires and the bar sample to eliminate the contact effect on conductivity.

4. Let the silver ink to dry in room condition for at least 8 h.

5. Heat the sample in a box furnace at 700 °C for 5 h. Set the ramping/cooling rate as 2 °C/min. The wires should be secured in place after the heat treatment.

6. Connect the wires on the sample to the leads of Probostat.

7. Connect the current leads to a source meter (Keithley 2400) and the voltage leads to a multimeter (Keithley 2700). Make sure the connection is made in the configuration shown in Figure G.1.
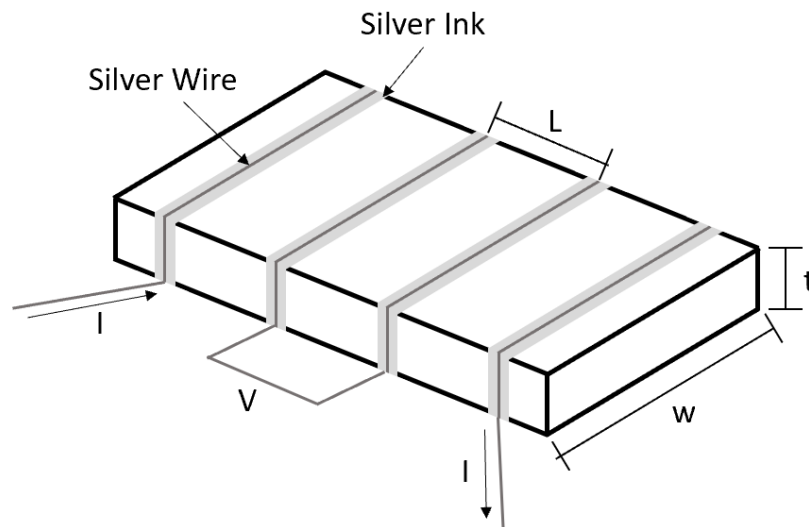
Figure G.1: Four-point electrical conductivity sample preparation
(Source: Gabriel R. Nile. Synthesis and characterization of dual-phase membranes. 2018)

8. When measuring the conductivity in the air, the outer enclosing tube is not necessary. However, when special conditions are desired, the enclosing tube should be installed before heating.

9. Set up the furnace and start heating. Set the ramping/cooling rate as 2 °C/min.

10. Use the source meter to provide current and use the multimeter to measure the voltage. Due to the small resistance, the multimeter alone cannot give accurate result despite it has 4-point mode.

APPENDIX H

FABRICATION OF ASYMMETRIC MEMBRANE VIA CENTRIFUGAL

CASTING

1. The composition of BYS-SDC slurry is BYS/SDC powder in 40/60 wt%. The SDC powder used for BYS-SDC slurry is the batch calcined at 950°C. The solid/water (deionized) ratio is 50/50 wt%.

2. The composition of SDC slurry is SDC/water (deionized) in 20/80 wt%. The SDC used here is the batch calcined at 550°C.

3. The amount of slurry needed is determined by the size of the mold. It can only be determined by trial-and error at first. In this dissertation, the molds used is 7 cm long and has an I.D. of 0.9 cm. About 8 g of slurry will be sufficient to fill the mold.

4. Add 5~10 drops of 3% polyvinyl alcohol (PVA) into the mixture.

5. Ball mill the mixtures for 4 h. Set the rotational speed at 14.

6. When finished, use a metal sieve to remove the milling balls from the slurry.

7. Before using the centrifuge mold, the inner surface must be cleaned and lubricated lightly with Vaseline.

8. Assemble the mold by installing the rubber sleeve and the clamps. Once finished, install a Teflon stopper at one end.

9. Pour the SDC slurry into the mold first. Once filled, seal the mold with another Teflon stopper. The reasons for making the SDC layer outside are (1) increase membrane surface area per unit length and (2) easier to spot defects if there are any.

10. Use the high-speed stirrer to perform the centrifugal casting. Set the speed at 4500 rpm and spin for 20 min.

11. When finished, open one end of the tube and drain the liquid. Pour in the BYS-SDC slurry.

12. Repeat step 11.

13. When finished, open one end of the tube and drain the liquid. Place the mold vertically on a paper towel for about 1min and then put the tube upside down for another minute. Make sure there are no water droplets before drying.

14. The drying is done in the humidity chamber, which should be set at 60% RH and 40°C. Allow the tube to dry in the humidity chamber for at least 12 h.

15. After step 15, the green body should already shrink and detached from the mold. Carefully remove the sleeve and the clamps to open the mold and take the green body out.

16. Let the tube body sit at room condition for about 12 h. This will help the ceramic body to stabilize.

17. Sinter the tube at 1150 °C for 10 h. Set the ramping rate at 1°C/min.

APPENDIX I

MEMBRANE REACTOR OPERATION MANUAL

1. Prepare a powder mixture of SDC/Pyrex powder/NaAl(OH)$_4$ in the ratio of 4/5/1. Grind the powder with a mortar and a pestle for 30 min.

2. Add few drops of deionized water into the mixture and keep grinding.

3. Repeat step 2 until the ceramic paste is homogeneous and easy to apply. A few drops of 3% PVA solution can be added (optional).

4. Place the membrane on the groove of the inner tube of the membrane module.

5. Apply the ceramic paste to the seam between the membrane and the alumina tube with a small piece of plastic. The plastic can be cut from a pipette.

6. Place a dense alumina disc on the top of the membrane. Use the same method as describe in step 5 to apply the paste to the seam.

7. Let the paste dry in room condition for at least 1 day.

8. Assemble the membrane module. Install the outer tube to the bottom fitting. Place the tubular furnace into place, then install the top fitting.

9. Connect gas lines and start heating in the rate of 1 °C/min to 750 °C. Maintain the temperature at 750 °C for 5 h.

10. Connect the permeate or retentate outlets (depending on what is to measure) to the gas chromatography (Agilent 7890A).

11. Introduce 100 ml/min nitrogen to the feed side and 100 ml/min helium to the sweep side to test leakage of the system. If the detected concentration is higher than 0.5%, the furnace should be turned off and the membrane/sealing should be inspected after the set-up cools down. Replace the membrane or re-apply the sealing paste if necessary.

12. Disconnect the outlets from the GC.

13. Install the cold traps and set up the ice water bath for the cold traps.

14. Turn on the heating tapes and the syringe pump. Make sure the steam has been supplied appropriately before feeding in methane. This is to prevent carbon deposition.

15. Start methane supply. The S/C ratio can be adjusted depending on the experiment condition.

16. Reconnect the outlets to the GC and start measurement.

APPENDIX J

MATLAB PROGRAM FOR KINETIC PARAMETER ANALYSIS

```matlab
function SRM_kinetics
clear global; clear all; clc;

% Import Data in Structure & Global Declaration from SMR_hr***.txt file
% *** would be the temp. of the case
global T t p data
data = importdata('SMR_hr500.txt');
t0 = data.data(1,1:8); t0 = t0';
T = data.data(2,1); T = T + 273;
p0 = data.data(3:6,1:8); p0 = p0';

% spline interpolation to smooth the data
t = linspace(min(t0),max(t0),100);
for i = 1:size(p0,2)
    p(:,i) = spline(t0,p0(:,i),t);
end


assignin('base','t',t);
assignin('base','T',T);
assignin('base','p',p);

function P = kinetics(theta,t)
% Input flow rate CH4,H2O,CO,H2,CO2 (in mol/min),total (in Pa)
% Initial value
p0 = [0.25;0.75;1e-4;1e-4;1e-4];

% ODE Solver
[tt, Pp] = ode45(@ DiffEq,t,p0);

    function  dP = DiffEq(t, p)


        % flow rate of each component,mol/min
        PCH4 = p(1);
        PH2O = p(2);
        PCO  = p(3);
        PH2  = p(4);
        PCO2 = p(5);
        JCO2 = 0;                        %mol/m^2/s

        %Keq, equilibrium constant
        Ksr  = exp(30.42-27106/T);
        Kwgs = exp(-4.775+4846/T);

        %DEN
        DEN = 1+abs(7.78e-5*exp(71120/8.314/T))*p(3)+abs(5.44e-
9*exp(79990/8.314/T))*p(4)+theta(3)*p(1)+theta(4)*p(2)/p(4);

        %Reaction kinetic equations
        r_sr     = theta(1)*(p(1)*p(2)-
p(4)^3*p(3)/Ksr)/(p(4)^2.5)/DEN^2; %mol/g-hr
        r_wgs    = 4.29e6*exp(-66090/8.314/T)*(p(3)*p(2)-
p(4)*p(5)/Kwgs)/p(4)/DEN^2;
```

179

```matlab
        r_total = theta(3)*(p(1)*p(2)^2-
p(4)^4*p(5)/Ksr/Kwgs)/(p(4)^3.5)/DEN^2;

        %Molar banlance (WGS temperary 1/3/2019) mol
        pdot = zeros(5,1);
        pdot(1) = -(r_sr+r_total);
        pdot(2) = -(r_sr+r_wgs+2*r_total);
        pdot(3) = (r_sr-r_wgs);
        pdot(4) = (3*r_sr+r_wgs+4*r_total);
        pdot(5) = (r_wgs+r_total);
        dP = pdot;
    end
P = Pp;
end


% Initialization
theta0 = [1,1,1e-2,1e-1];

% Curve Fitting
%    -> Tolerance setting
lb = [1e-2 1e-4 1e-3 1e-3];
ub = [100 10 1 10];
options =  optimoptions('lsqcurvefit','FunctionTolerance',1e-12);


[theta,Rsdnrm,Rsd,ExFlg,OptmInfo,Lmda,Jmat] = ...
    lsqcurvefit(@kinetics,theta0,t,p,lb,ub,options);

tv = linspace(min(t), max(t));
Pfit = kinetics(theta, tv);
save theta theta

% Parameter Show
OptmInfo
fprintf(1,'\tRate Constants:\n');
for k1 = 1:length(theta)
    fprintf(1, '\t\tTheta(%d) = %8.5f\n', k1, theta(k1))
end

% Plot Simulation Result
figure(1)
plot(t, p, 'o:');
hold on;
hlp = plot(tv, Pfit);
hold off; grid
xlabel('Time'); ylabel('Concentration');
xlim([0 20]); ylim([0 1]);
legend(hlp, 'P_1(t)', 'P_2(t)', 'P_3(t)', 'P_4(t)','P_5(t)',
'Location','NE')
set(gca, 'fontname', 'times');
set(gca,'fontsize', 12);
end
```

```matlab
function WGS_kinetics
clear global; clear all; clc;

% Import Data in Structure & Global Declaration from WGS***.txt file
% *** would be the temp. of the case
global T t p data
data = importdata('WGS300.txt');
t0 = data.data(1,1:8); t0 = t0';
T = data.data(2,1); T = T + 273;
p0 = data.data(3:6,1:8); p0 = p0';

% spline interpolation to smooth the data
t = linspace(min(t0),max(t0),100);
for i = 1:size(p0,2)
    p(:,i) = spline(t0,p0(:,i),t);
end

assignin('base','t',t);
assignin('base','p',p);
assignin('base','T',T);

function P = kinetics(theta,t)
% Input flow rate CH4,H2O,CO,H2,CO2 (in mol/min),total (in Pa)
% Initial value
p0 = [0.25;0.75;1e-4;1e-4];

% ODE Solver
[tt, Pp] = ode45(@ DiffEq,t,p0);

    function  dP = DiffEq(t, p)

        %flow rate of each component,mol/min
        PCO = p(1);
        PH2O = p(2);
        PH2  = p(3);
        PCO2  = p(4);
        JCO2 = 0;

        %{
        theta(1)=k2;
        theta(2)=KCO;
        theta(3)=KH2;
        theta(4)=KH2O;
        %}

        %Keq, equilibrium constant
        Kwgs = exp(-4.775+4846/T);

        %DEN
        DEN = 1+theta(2)*p(1)+theta(3)*p(3);

        %Reaction kinetic equations
        r_wgs  = theta(1)*(p(1)*p(2)-p(3)*p(4)/Kwgs)/p(3)/DEN^2;
```

181

```matlab
        %Molar banlance (WGS temperary 1/3/2019) mol
        pdot = zeros(4,1);
        pdot(1) = -r_wgs;
        pdot(2) = -r_wgs;
        pdot(3) = r_wgs;
        pdot(4) = r_wgs;
        dP = pdot;
    end
P = Pp;
end

% Initialization
theta0 = [10,100,0.01];

% Curve Fitting
%    -> Tolerance setting
lb = [1 10 0.01];
ub = [100 1000 1];
options =  optimoptions('lsqcurvefit','FunctionTolerance',1e-6);



[theta,Rsdnrm,Rsd,ExFlg,OptmInfo,Lmda,Jmat] = ...
    lsqcurvefit(@kinetics,theta0,t,p,lb,ub,options);

tv = linspace(min(t), max(t));
Pfit = kinetics(theta, tv);
save theta theta

% Parameter Show
OptmInfo
fprintf(1,'\tRate Constants:\n')
for k1 = 1:length(theta)
    fprintf(1, '\t\tTheta(%d) = %8.5f\n', k1, theta(k1))
end

% Plot Simulation Result
figure(1)
plot(t, p, 'o:');
hold on;
hlp = plot(tv, Pfit);
hold off; grid
xlabel('Time'); ylabel('Concentration');
xlim([0 20]); ylim([0 1]);
legend(hlp, 'P_1(t)', 'P_2(t)', 'P_3(t)', 'P_4(t)', 'Location','NE')
set(gca, 'fontname', 'times');
set(gca,'fontsize', 12);
end
```

APPENDIX K

MATLAB PROGRAM FOR MEMBRANE REACTOR MODELING

```matlab
function MR

%1 Simulation parameters
    global d L dp dt ro Ro void a A A1 m den Ps Pt0 R FCH4 ICH4 IH2O n
Fsw SN2 Tf T u Qz Fz
%1.1 Membrane
    d=1.25e-4;                      %thickness of the membrane, m
    L=3.5e-2;                       %length of the membrane, m
    a=0.85;                         %area reduced by the sealing
    LL=L/100;                       %step size
    ro=0.35e-2;                     %outer radius of the membrane, m
    Ro=0.92e-2;                     %chamber inner radius, m
    dt=0.85e-2;                      %average diameter of catalyst bed, m
    A=pi*(Ro^2-ro^2);               %the cross-sectional of catalyst packing,
m^2
    A1=2*ro*pi;
%1.2 Catalyst
    m=0.2;                          %amount of catalyst, g
    den=m/A/L;                      %catalyst density, g/m3
    dp=500e-6;                      %diameter of the catalyst pellet, m
    void=0.38+0.073*(1-(dt/dp-2)^2/(dt/dp)^2);
                                    %void fraction in catalyst bed.
                                    %Ref.: D.P. Haughey, G.S.G. Beveridge,
Structural properties of packed beds ? A review.
                                    %The Canadian Journal of Chemical
Engineering 47 (1969) 130?140.
%1.3 Operation conditions
    R=8.314;                        %gas constant
    Tf=698;                         %feed temperature, C
    T=Tf+273.15;                    %feed temperature, K
    Pt0=1;                          %feed (tube) side pressure, atm
    Ps=1;                           %permeate (shell) side pressure, atm
    FCH4=5;                         %H4 feed flow rate, ml/min
    ICH4=FCH4/24500;                %CH4 feed flow rate, mol/min
    n=1;                            %feed molar ratio of H2O/CH4
    IH2O=n*ICH4;                    %H2O feed flow rate, mol/min
    Fsw=200;                        %sweep gas flow rate, ml/min
    SN2=Fsw/24500;                  %sweep gas flow rate, mol/min

%Flow rate equations
for j=1:6
    n=n+0.33;
    IH2O=n*ICH4;
    i=1;
while i<=101
    T=T+2;                          %400-600C
    u=(ICH4+IH2O)*T*R/(Pt0*101325)/60/A;   %average flow rate at the
inlet of the membrane, m/s

%TO SOLVE themodynamic equilibrium conversion
%{
F0=[ICH4,IH2O,1e-15,1e-15,2.23e-4,1e-15,1e-15,1e-15,1e-15,1e-
15,Pt0*101325]; %Feeding flow rate of CO, H2O, CO2 and H2
    [te, ye] = ode45(@Equili,[0:0.001:L*5],F0);
```

```matlab
    %[t,y] = ode45(odefun,tspan,y0), where tspan = [t0 tf], integrates
the system of differential equations y'=f(t,y) from t0 to tf with
initial conditions y0.
    %fCO(i)=yy(:,1);        %flow rate, mol/min
    %fH2O(i)=yy(:,2);
    %fCO2(i)= yy(:,3);
    %fH2(i)=yy(:,4);

    ch4(j,i)=100*(ICH4-ye(6,1))/ICH4;    %CO conversion via FBR
    save ch4 ch4
%Traditional fixed-bed reactor
    F0=[ICH4,IH2O,1e-15,1e-15,2.23e-4,1e-15,1e-15,1e-15,1e-15,1e-
15,Pt0*101325]; %Feeding flow rate of CO, H2O, CO2 and H2
    [tt, yy] = ode45(@EquationsTR,[0:0.001:L],F0);
    %[t,y] = ode45(odefun,tspan,y0), where tspan = [t0 tf], integrates
the system of differential equations y'=f(t,y) from t0 to tf with
initial conditions y0.
    %fCO(i)=yy(:,1);        %flow rate, mol/min
    %fH2O(i)=yy(:,2);
    %fCO2(i)= yy(:,3);
    %fH2(i)=yy(:,4);

    xCH4(j,i)=100*(ICH4-yy(6,1))/ICH4;    %CO conversion via FBR
    save xCH4 xCH4
%}
%.....................To solve MR differential equations
group......................
    F0=[ICH4,IH2O,1e-15,1e-15,1e-15,1e-15,1e-15,1e-15,1e-15,1e-
15,Pt0*101325];
    [z, y] = ode23s(@Equations,[0:LL:L],F0);
%membrane upstream flow, mol/min
    %FCO(i)=y(:,1);
    %FH2O(i)=y(:,2);
    %FCO2(i)=y(:,3);
    %FH2(i)=y(:,4);
%membrane downstream flow, mol/min
    %QCO(i)=y(:,5);
    %QH2O(i)=y(:,6);
    %QCO2(i)=y(:,7);
    %QH2(i)=y(:,8);

    t(i)=T-273.15;


%.....................
    XCH4(j,i)=100*(ICH4-y(end,1))/ICH4;       %CO conversion via CMR
    flux(j,i)=Ps*y(end,10)*24500/(A1*L*a*10000);   % ml/cm^2/min,
membrane area 6.6 cm^2
    RCO2(j,i)=y(end,10)/(y(end,5)+y(end,10));        %CO2 recovery via
CMR
    H2_yield(j,i)=y(end,4)/ICH4/4;
    CH2(j,i)=y(end,4)/(y(end,1)+y(end,3)+y(end,4)+y(end,5));
    CCO(j,i)=y(end,3)/(y(end,1)+y(end,3)+y(end,4)+y(end,5));
    save y y
    save CH2 CH2
    save CCO CCO
    save H2_yield
```

```
    save XCH4 XCH4
    save flux flux
    save RCO2 RCO2

    i=i+1;
end
T=T-2*(i-1);
end
jj=1:0.333:2.998;      %in order to plot figures, set up S/C molar ratio



%....................drawing figure....................
% variation of CH4 conversion with reaction temperature
figure(1)
plot(t,XCH4(6,:),'r-s')
xlabel('T(^oC)')
ylabel('%')
%axis ([400,550,0,100])
title('H_2O/CH4=3')
legend('CH4 Con.MR')
grid on


% variation of CO2 recovery with reaction temperature
figure(2)
plot(t,100*RCO2(6,:),'g-s')
xlabel('T(^oC)')
ylabel('%')
title('H_2O/CH_4=3')
legend('CO_2 Rec.MR')
grid on


% variation of CO2 flux with reaction temperature
figure(4)
plot(t,flux(6,:),'b-s')
xlabel('T(^oC)')
ylabel('mol/min/m^{2}')
title('H_2O/CH4=3')
legend('CO2 Flux.MR')
grid on

% variation of H2 concentration with reaction temperature
figure(5)
plot(t,CH2(6,:),'c-s')
xlabel('T(^oC)')
ylabel('%')
title('H_2O/CH_4=3')
legend('H2 Con.MR')
grid on


%..........Catalytic Membrane Reactor..........
```

```matlab
function  ydot = Equations(z, y)
global A den T d R Ps dp void u JCO2 Pt SN2 A1 Ksr Kwgs ksr kwgs ktotal
a
%flow rate of each component,mol/min
FCH4=y(1);
FH2O=y(2);
FCO=y(3);
FH2=y(4);
FCO2=y(5);
QCH4=y(6);
QH2O=y(7);
QCO=y(8);
QH2=y(9);
QCO2=y(10);
Fz=y(1)+y(2)+y(3)+y(4)+y(5);
Qz=y(6)+y(7)+y(8)+y(9)+y(10)+SN2;

%partial pressure of each component, atm (tube side and shell side)
Pt=y(11)/101325;
PCH4=Pt*y(1)/Fz;
PH2O=Pt*y(2)/Fz;
PCO=Pt*y(3)/Fz;
PH2=Pt*y(4)/Fz;
PCO2=Pt*y(5)/Fz;
pCO2=Ps*y(10)/Qz;

n=-1.716+2155/T;
JCO2=320.22*exp(-45427/8.314/T)*T*8.314*(PCO2^n-
pCO2^n)/n/4/96485^2/d; %mol/m^2/s

%Keq, equilibrium constant
Ksr=exp(30.42-27106/T);
Kwgs=exp(-4.775+4846/T);

%Adsorption constants (Xu and Froment AICHE J 1989)
KCO=7.78e-5*exp(71120/8.314/T);
KH2=5.44e-9*exp(79990/8.314/T);
KCH4=5.17e-4*exp(40070/8.314/T);
KH2O=1.75e5*exp(-87960/8.314/T);

%DEN
DEN=1+KCO*PCO+KH2*PH2+KCH4*PCH4+KH2O*PH2O/PH2;

%Rate constants
ksr=2.2e11*exp(-189000/8.314/T);
kwgs=4.29e4*exp(-66090/8.314/T);
ktotal=2.53e11*exp(-195900/8.314/T);

%Reaction kinetic equations
r_sr=ksr*(PCH4*PH2O-PH2^3*PCO/Ksr)/PH2^2.5/DEN^2/60; %mol/g-min
r_wgs=kwgs*(PCO*PH2O-PH2*PCO2/Kwgs)/PH2/DEN^2/60;
r_total=ktotal*(PCH4*PH2O^2-PH2^4*PCO2/Ksr/Kwgs)/PH2^3.5/DEN^2/60;

%viscosity calculation
b12=(18/16)^0.5;b21=1/b12;                   %1:CH4,2;H2O,3:CO,4:H2,5:CO2
```

```matlab
b13=(28/16)^0.5;b31=1/b13;
b14=(2/16)^0.5;b41=1/b14;
b15=(44/16)^0.5;b51=1/b15;
b23=(28/18)^0.5;b32=1/b23;
b24=(2/18)^0.5;b42=1/b24;
b25=(44/18)^0.5;b52=1/b25;
b34=(2/28)^0.5;b43=1/b34;
b35=(44/28)^0.5;b53=1/b35;
b45=(44/2)^0.5;b54=1/b35;
u1=1.253e-6*T^1.5/(T+197.8);
u2=(1.1127e-6*T^0.5338)/(1+94.7/T+0/T^2);        %viscosity of CO N-s/m2
u3=(1.7096e-8*T^1.1146)/(1+0/T+0/T^2);
u4=(2.148e-6*T^0.46)/(1+290/T+0/T^2);
u5=(1.797e-7*T^0.685)/(1-0.59/T+140/T^2);


ug=u1.*y(1)./(y(1)+b12.*y(2)+b13.*y(3)+b14.*y(4)+b15.*y(5))+u2.*y(2)./(
y(2)+b21.*y(1)+b23.*y(3)+b24.*y(4)+b25*y(5))+u3.*y(3)./(y(3)+b31.*y(1)+
b32.*y(2)+b34.*y(4)+b35.*y(5))...

+u4.*y(4)./(y(4)+b41.*y(1)+b42.*y(2)+b43.*y(3)+b45.*y(5))+u5.*y(5)./(y(
5)+b51.*y(1)+b52.*y(2)+b53.*y(3)+b54.*y(4));        %viscosity of
mixture N-s/m2% Plot the results

Mm=(y(1)*16+y(2)*18+y(3)*28+y(4)*2+y(5)*44);        %average molar
weight in the tube,g/mol
rog=Mm*Pt*101325/(R*T)/1e3;        %density of the gas mixture in
the tube,kg/m3


%Molar banlance
ydot(1)=-A*den*(r_sr+r_total);
ydot(2)=-A*den*(r_sr+r_wgs+2*r_total);
ydot(3)=A*den*(r_sr-r_wgs);
ydot(4)=A*den*(3*r_sr+r_wgs+4*r_total);
ydot(5)=A*den*(r_wgs+r_total)-JCO2*A1*a*60;
ydot(6)=1e-15;
ydot(7)=1e-15;
ydot(8)=1e-15;
ydot(9)=1e-15;
ydot(10)=JCO2*A1*a*60;
ydot(11)=-(((150*ug*u*(1-void)^2)/((dp)^2*void^3))+1.75*rog*u^2*(1-
void)/(dp*void^3));
ydot=ydot';
```

APPENDIX L

MATLAB PROGRAM FOR DIMENSIONLESS PARAMETRIC STUDY

```matlab
function MR_dimensionless

%1 Simulation parameters
    global d L dp ri dt ro void Ro A A1 m den Ps Pt0 R FCH4 ICH4 IH2O n
Fsw SN2 Tf T u P0 theta step
%1.1 Membrane
    d=1.2e-4;                   %thickness of the membrane, m
    L=3.5e-2;                   %length of the membrane, m
    ri=0.3e-2;                  %inner radius of the membrane, m
    ro=0.35e-2;                 %outer radius of the membrane, m
    Ro=0.92e-2;                 %chamber inner radius, m
    dt=0.7e-2;
    A=pi*(Ro^2-ro^2);           %the cross-sectional of catalyst packing,
m^2
    A1=2*ro*pi;
%1.2 Catalyst
    m=0.2;                      %amount of catalyst, g
    den=m/A/L;                  %catalyst density (total bed vol.~10ml),
g/m3
    dp=500e-6;                  %diameter of the catalyst pellet, m
    void=0.38+0.073*(1-(dt/dp-2)^2/(dt/dp)^2);
                                %void fraction in catalyst bed.
                                %Ref.: D.P. Haughey, G.S.G. Beveridge,
Structural properties of packed beds ? A review.
                                %The Canadian Journal of Chemical
Engineering 47 (1969) 130?140.
%1.3 Operation conditions
    R=8.314;                    %gas constant
    Tf=680;                     %feed temperature, C
    T=Tf+273.15;                %feed temperature, K
    Pt0=1;                      %feed (tube) side pressure, atm
    Ps=1;                       %permeate (shell) side pressure, atm
    FCH4=1;                     %CH4 feed flow rate, ml/min
    ICH4=FCH4/24500;            %CH4 feed flow rate, mol/min
    n=3;                        %feed molar ratio of H2O/CH4
    IH2O=n*ICH4;                %H2O feed flow rate, mol/min
    Fsw=20;                     %sweep gas flow rate, ml/min
    SN2=Fsw/24500;              %sweep gas flow rate, mol/min
    step=100;                   %number of steps
    zspan=0:(1/step):1;
    u=(ICH4+IH2O)*T*R/(Pt0*101325)/60/A;   %average flow rate at the
inlet of the membrane, m/s




%....................To solve MR differential equations
group....................
for i=1
    while i<=11
    T=T+20;
    j=linspace(700,900,11);
    TT(i)=4.36e-56*j(i)^19.03;
    theta=TT(i)
    save theta theta
    F0=[1,n,1e-6,1e-6,1e-6,1e-15,1e-15,1e-15,1e-15,1e-15,Pt0];
```

```matlab
P0=[ICH4*1/sum(F0(1:5)),IH2O*n/sum(F0(1:5)),F0(3)/sum(F0(1:5)),F0(4)/su
m(F0(1:5)),F0(5)/sum(F0(1:5))];
    [z, y] = ode23(@Equations,zspan,F0);
    flux=Ps*y(end-1,10)/7;

    YH2(i)=y(end,4)/4;
    CO=y(end,3)/(y(end-1,1)+y(end-1,3)+y(end-1,4)+y(end-1,5));
    XCH4(i)=real(y(1,1)-y(end,1))/real(y(1,1));
    CH2(i)=real(y(end,4))/real(y(end,1)+y(end,3)+y(end,4)+y(end,5));

    t(i)=T-273.15;
    save CO CO
    save YH2 YH2
    save CH2 CH2
    save flux flux
    save y y
    save XCH4 XCH4
    i=i+1;
    end
    T=T-20*(i-1);
end
load handel
sound(y,Fs)
%membrane upstream flow, mol/min
    %FCO(i)=y(:,1);
    %FH2O(i)=y(:,2);
    %FCO2(i)=y(:,3);
    %FH2(i)=y(:,4);
%membrane downstream flow, mol/min
    %QCO(i)=y(:,5);
    %QH2O(i)=y(:,6);
    %QCO2(i)=y(:,7);
    %QH2(i)=y(:,8);


%{
function [value, isterminal, direction] = negfilter(z, y)
value      = ispos(y(3));
isterminal = 1;    % Stop the integration
direction  = -1;
%}

%..........Catalytic Membrane Reactor..........
function  ydot = Equations(z, y)
global A den T d L P0 R Ps dp void u JCO2 Pt SN2 A1 Ksr Kwgs ksr kwgs
ktotal theta ICH4 rmax Da step
%flow rate of each component,mol/min
fCH4=y(1);
fH2O=y(2);
fCO=y(3);
fH2=y(4);
fCO2=y(5);
qCH4=y(6);
qH2O=y(7);
qCO=y(8);
```

191

```matlab
qH2=y(9);
qCO2=y(10);
fz=y(1)+y(2)+y(3)+y(4)+y(5);
qz=y(6)+y(7)+y(8)+y(9)+y(10)+SN2/ICH4;


%partial pressure of each component, atm (tube side and shell side)
Pt=y(11);
PCH4=Pt*y(1)/fz;
PH2O=Pt*y(2)/fz;
PCO=Pt*y(3)/fz;
PH2=Pt*y(4)/fz;
PCO2=Pt*y(5)/fz;
pCO2=Ps*y(10)/qz;



%gas permeance, mol m-2 s-1 Pa-1;
n=-1.716+2155/T;
JCO2=320.22*exp(-45427/8.314/T)*T*8.314*(PCO2^n-
pCO2^n)/n/4/96485^2/d; %mol/m^2/s
theta=JCO*A1*60*(PCO2^n)/ICH4/(PCO2^n-pCO2^n);


%Keq, equilibrium constant
Ksr=exp(30.42-27106/T);
Kwgs=exp(-4.775+4846/T);



%Adsorption constants (Xu and Froment AICHE J 1989)
KCO=1.04e-4*exp(70650/8.314/T);
KH2=5.44e-9*exp(82900/8.314/T);
KCH4=5.17e-4*exp(38280/8.314/T);
KH2O=3.50e5*exp(-88680/8.314/T);


%DEN
DEN=1+KCO*PCO+KH2*PH2+KCH4*PCH4+KH2O*PH2O/PH2;
DEN0=1+KCO*P0(3)+KH2*P0(4)+KCH4*P0(1)+KH2O*P0(2)/P0(4);


%Rate constants
ksr=2.2e11*exp(-188900/8.314/T);
kwgs=4.29e4*exp(-66090/8.314/T);
ktotal=2.53e11*exp(-195900/8.314/T);



%Reaction kinetic equations
rmax=ksr*(P0(1)*P0(2))/P0(4)^2.5/DEN0^2;

%Damkohler number
Da=rmax*A*den*L/ICH4/step;
save Da Da
r_sr=ksr*(PCH4*PH2O-PH2^3*PCO/Ksr)/PH2^2.5/DEN^2/rmax; %mol/g-min
r_wgs=kwgs*(PCO*PH2O-PH2*PCO2/Kwgs)/PH2/DEN^2/rmax;
r_total=ktotal*(PCH4*PH2O^2-PH2^4*PCO2/Ksr/Kwgs)/PH2^3.5/DEN^2/rmax;


%viscosity calculation
b12=(18/16)^0.5;b21=1/b12;                %1:CH4,2;H2O,3:CO,4:H2,5:CO2
```

192

```matlab
b13=(28/16)^0.5;b31=1/b13;
b14=(2/16)^0.5;b41=1/b14;
b15=(44/16)^0.5;b51=1/b15;
b23=(28/18)^0.5;b32=1/b23;
b24=(2/18)^0.5;b42=1/b24;
b25=(44/18)^0.5;b52=1/b25;
b34=(2/28)^0.5;b43=1/b34;
b35=(44/28)^0.5;b53=1/b35;
b45=(44/2)^0.5;b54=1/b35;
u1=1.253e-6*T^1.5/(T+197.8);
u2=(1.1127e-6*T^0.5338)/(1+94.7/T+0/T^2);        %viscosity of CO N-s/m2
u3=(1.7096e-8*T^1.1146)/(1+0/T+0/T^2);
u4=(2.148e-6*T^0.46)/(1+290/T+0/T^2);
u5=(1.797e-7*T^0.685)/(1-0.59/T+140/T^2);

ug=u1.*y(1)./(y(1)+b12.*y(2)+b13.*y(3)+b14.*y(4)+b15.*y(5))+u2.*y(2)./(
y(2)+b21.*y(1)+b23.*y(3)+b24.*y(4)+b25*y(5))+u3.*y(3)./(y(3)+b31.*y(1)+
b32.*y(2)+b34.*y(4)+b35.*y(5))...

+u4.*y(4)./(y(4)+b41.*y(1)+b42.*y(2)+b43.*y(3)+b45.*y(5))+u5.*y(5)./(y(
5)+b51.*y(1)+b52.*y(2)+b53.*y(3)+b54.*y(4));        %viscosity of
mixture N-s/m2% Plot the results

Mm=(y(1)*16+y(2)*18+y(3)*28+y(4)*2+y(5)*44);        %average molar
weight in the tube,g/mol
rog=Mm*Pt*101325/(R*T)/1e3;            %density of the gas mixture in
the tube,kg/m3




%Molar banlance
ydot(1)=-Da*(r_sr+r_total);
ydot(2)=-Da*(r_sr+r_wgs+2*r_total);
ydot(3)=Da*(r_sr-r_wgs);
ydot(4)=Da*(3*r_sr+r_wgs+4*r_total);
ydot(5)=Da*(r_wgs+r_total)-theta*(1-(pCO2^n)/(PCO2^n));
ydot(6)=1e-15;
ydot(7)=1e-15;
ydot(8)=1e-15;
ydot(9)=1e-15;
ydot(10)=theta*(1-(pCO2^n)/(PCO2^n));
ydot(11)=-(((150*ug*u*(1-void)^2)/((dp)^2*void^3))+1.75*rog*u^2*(1-
void)/(dp*void^3))/101325;
ydot=ydot';
```